

Contents

| | |
|--|-----------|
| 1. Abstract | 5 |
| 2. List of papers | 6 |
| 3. Introduction | 9 |
| 4. Light propagation in tissue - theory and models | 11 |
| 4.1 Introductory overview | 11 |
| 4.2 Radiative transport theory | 13 |
| 4.2.1 Discretisation methods..... | 17 |
| 4.2.2 Expansion methods | 21 |
| 4.2.3 Probabilistic methods | 23 |
| 4.2.4 Discussion - radiative transport theory | 25 |
| 4.3 Electromagnetic theory | 28 |
| 4.3.1 Tissue as a random continuum | 30 |
| 4.3.2 Tissue as a collection of particles | 31 |
| 4.3.3 Discussion - electromagnetic theory..... | 36 |
| 4.4 Relationship between the radiative transport and electromagnetic theories | 38 |
| 5. Computational methods..... | 41 |
| 5.1 Computations treating the indirect problem | 41 |
| 5.2 Computations treating the direct problem..... | 49 |
| 6. Optical properties - measurement techniques..... | 51 |
| 6.1 One-parameter techniques | 51 |
| 6.2 Two-parameter techniques | 52 |
| 6.2.1 Spatially resolved techniques..... | 53 |
| 6.2.2 Time-resolved techniques..... | 53 |
| 6.2.3 Frequency domain measurements..... | 55 |
| 6.2.4 Other techniques | 55 |
| 6.3 The integrating sphere method - a three parameter technique | 56 |
| 6.3.1 Sources of errors in the sphere measurements | 57 |
| 6.3.2 Sources of errors in the narrow-beam measurements | 59 |
| 6.3.3 Double integrating sphere arrangement combined with a narrow-beam set-up..... | 60 |
| 7. Microscopic features of tissue and their relationship to the optical properties..... | 62 |
| 7.1 Microscopic features and light absorption..... | 62 |
| 7.1.1 Light absorbing molecules in tissue..... | 63 |
| 7.1.2 Configurational factors influencing the absorption coefficient | 67 |
| 7.2 Microscopic features and light scattering | 68 |
| 7.2.1 Light scattering structures in tissue | 69 |
| 7.2.2 Configurational factors influencing the scattering properties..... | 71 |

| | |
|---|------------|
| 8. Laser-based treatment modalities - tissue optical aspects | 76 |
| 8.1 Photodynamic therapy | 76 |
| 8.1.1 <i>The distribution of the photoactive drug</i> | 76 |
| 8.1.2 <i>The light distribution</i> | 77 |
| 8.1.3 <i>The photochemical reaction</i> | 77 |
| 8.1.4 <i>The treatment response</i> | 78 |
| 8.2 Thermotherapy | 79 |
| 8.2.1 <i>The light energy deposition</i> | 79 |
| 8.2.2 <i>The treatment response</i> | 81 |
| 9. Optical diagnostic techniques - tissue optical aspects | 84 |
| 9.1 Laser-induced fluorescence | 85 |
| 9.1.1 <i>Propagation of excitation and emission light</i> | 86 |
| 9.1.2 <i>Fluorescence from exogenous fluorophores</i> | 87 |
| 9.1.3 <i>Evaluation methods</i> | 88 |
| 9.2 Elastic scattering spectroscopy | 89 |
| 9.3 Laser-Doppler flowmetry | 91 |
| 10. Summary of papers | 94 |
| 11. Acknowledgements | 97 |
| 12. References | 98 |
| 13. Papers | 108 |

1. Abstract

In this work a number of theoretical models, describing light propagation in matter, have been applied to and developed for the examination of tissue. The aim was to model the light scattering and absorption in tissue in order to improve the understanding of underlying mechanisms of laser-based diagnostics and treatment modalities utilised for cancer and cardiovascular diseases. The models studied ranged from the simplest Beer-Lambert law, assuming a plain exponential behaviour of the light transport, to solutions of Maxwell's fundamental equations for the scattering of electromagnetic waves. The latter approach was specifically used for computations of light scattering by red blood cell volume-equivalent spheroids by applying the numerical T-matrix formalism. Furthermore, the adding-doubling method, based on the radiative transport equation for multiple scattering, as well as the stochastic Monte Carlo approach, describing the light transport as a random walk process of photons, were employed to model light propagation in dense tissue. The advantages and disadvantages of each model are discussed by exemplifying which applications they are useful for and valid in.

Light scattering and absorption in tissue were also studied in practice. The absorption and scattering characteristics governing the macroscopic light propagation were determined *in vitro* in terms of the absorption and scattering coefficients as well as the g-factor, employing different integrating-sphere techniques. Changes in these fundamental optical properties were monitored for tissue being exposed to laser-based treatment modalities, such as photodynamic therapy (PDT) and continuous or pulsed thermotherapy. The observed influence on the scattering properties and the manifest increase in the absorption coefficient could be related to mainly morphological and biochemical changes in the blood and/or microvascular damage in the tissue. The latter was further confirmed by an imaging technique showing changes in laser-Doppler signals from moving red blood cells in conjunction with PDT, indicating a local increase in tissue perfusion.

Differences in tissue characteristics were monitored *in vivo*, in order to distinguish diseased from healthy tissue alone, or in combination with photosensitive agents, employing laser-induced fluorescence (LIF) or near infrared (NIR) spectroscopy. Malignancies in the skin and in the oesophagus could be identified utilising the tumour selective agents ALA and Photofrin respectively, in conjunction with LIF. It was also shown to be possible to spectroscopically distinguish fibrous and fatty heart tissue from healthy myocardium *in vitro* using either LIF or NIR spectroscopy, if combined with a powerful analysis method such as Principal Component Analysis (PCA).

2. List of papers

This thesis is based on the following papers:

- Paper I** A. M. K. Nilsson, R. Berg, and S. Andersson-Engels, "Measurements of the optical properties of tissue in conjunction with photodynamic therapy," *Appl. Opt.* **34**, 4609-4619 (1995)
- Paper II** A. M. K. Nilsson, C. Sturesson, D. L. Liu, and S. Andersson-Engels, "Changes in spectral shape of tissue optical properties in conjunction with laser-induced thermotherapy," *Appl. Opt.* (1997) (accepted)
- Paper III** W. Verkruijsse, A. M. K. Nilsson, T. E. Milner, J. F. Beek, G. W. Lucassen, and M. J. C. van Gemert, "Absorption of blood depends on temperature during a 0.5 ms laser pulse at 586 nm," submitted to *Photochem. Photobiol.* (1997)
- Paper IV** A. M. K. Nilsson, G. W. Lucassen, W. Verkruijsse, S. Andersson-Engels, and M. J. C. van Gemert, "Changes in optical properties of human whole blood *in vitro* due to slow heating," *Photochem. Photobiol.* **65**, 366-373 (1997)
- Paper V** A. M. K. Nilsson, P. Alsholm, A. Karlsson, and S. Andersson-Engels, "T-matrix computations of light scattering by red blood cells," submitted to *Appl. Opt.* (1997)
- Paper VI** A. Pifferi, A. M. K. Nilsson, and S. Andersson-Engels, "Accelerated Monte Carlo models to simulate fluorescence of layered tissues," manuscript for *JOSA* (1997)
- Paper VII** A. M. K. Nilsson, D. Heinrich, J. Olajos, and S. Andersson-Engels, "Near infrared diffuse reflection and laser-induced fluorescence spectroscopy for myocardial tissue characterisation," *Spectrochim. Acta* **53**, (1997) (in press)
- Paper VIII** C. Staël von Holstein, A. M. K. Nilsson, S. Andersson-Engels, R. Willén, B. Walther, and K. Svanberg, "Detection of adenocarcinoma in Barrett's oesophagus by means of laser induced fluorescence," *GUT* **39**, 711-716 (1996)

-
- Paper IX** C. af Klinteberg, I. Wang, A. M. K. Nilsson, S. Andersson-Engels, S. Svanberg, and K. Svanberg, " δ -aminolevulinic acid-induced protoporphyrin IX fluorescence in basal cell carcinomas of the skin," manuscript for Photochem. Photobiol. (1997)
- Paper X** C. af Klinteberg, A. M. K. Nilsson, I. Wang, S. Andersson-Engels, S. Svanberg, and K. Svanberg, "Kinetic fluorescence studies of δ -aminolevulinic acid-induced protoporphyrin IX accumulation in basal cell carcinomas," manuscript for Cancer Lett. (1997)
- Paper XI** A. M. K. Nilsson, I. Wang, C. af Klinteberg, S. Andersson-Engels, N. Bendsoe, S. Svanberg, and K. Svanberg, "Blood perfusion studies on basal cell carcinomas in conjunction with photodynamic- and cryo therapy employing laser-Doppler imaging," manuscript for Br. J. Dermatology (1997)
-

In addition to the above papers, material is also presented in:

A. M. K. Nilsson, R. Berg, and S. Andersson-Engels, "Integrating sphere measurements of tissue optical properties for accurate PDT dosimetry," in *Laser Interaction with Hard and Soft Tissue II*, H. J. Albrecht, G. P. Delacretaz, T. H. Meier, R. W. Steiner, L. O. Svaasand, and M. J. C. van Gemert, eds., Proc. Soc. Photo-Opt. Instrum. Eng. **2323**, 47-57 (1994)

H. Messmann, P. Mlkvy, S. Montán, I. Wang, A. Nilsson, K. Svanberg, S. Svanberg, A. MacRobert, and S. Bown, "Endoscopic fluorescence of gastrointestinal neoplasia after sensitisation with 5-amino laevulinic acid (ALA) or Photofrin," in *5th International Photodynamic Association Biennial Meeting*, D. A. Cortese, ed., Proc. Soc. Photo-Opt. Instrum. Eng. **2371**, 506-509 (1994)

A. M. K. Nilsson, C. Staël von Holstein, S. Andersson-Engels, R. Willén, B. Walther, and K. Svanberg, "Clinical detection studies of Barrett's metaplasia and oesophageal adenocarcinoma by means of laser-induced fluorescence," in *Optical Biopsies*, R. Cubeddu, S. R. Mordon, and K. Svanberg, eds., Proc. Soc. Photo-Opt. Instrum. Eng. **2627**, 49-56 (1995)

A. M. K. Nilsson, G. W. Lucassen, W. Verkruijsse, S. Andersson-Engels, and M. J. C. van Gemert, "Optical properties of human whole blood - changes due to slow heating," in *Laser-Tissue Interaction and Tissue Optics II*, H. J. Albrecht, G. P. Delacretaz, T. H. Meier, R. W. Steiner, and L. O. Svaasand, eds., Proc. Soc. Photo-Opt. Instrum. Eng. **2923**, 24-34 (1996)

C. af Klinteberg, A. M. K. Nilsson, I. Wang, S. Andersson-Engels, S. Svanberg, and K. Svanberg, "Laser-induced fluorescence diagnostics of basal cell carcinomas of the skin following topical ALA application," in *Optical Biopsies and Microscopic Techniques*, I. J.

Bigio, W. S. Grundfest, H. Schneckenburger, K. Svanberg, and P. M. Viallet, eds., Proc. Soc. Photo-Opt. Instrum. Eng. **2926**, 32-40 (1996)

A. M. K. Nilsson, R. Berg, and S. Andersson-Engels, "Measurements of the optical properties of tissue in conjunction with photodynamic therapy," in *Biomedical Optical Spectroscopy and Diagnostics*, E. Sevick-Muraca, and D. Benaron, eds., Trends in Optics and Photonics **III**, OSA, 234-244 (1996)

C. af Klinteberg, A. M. K. Nilsson, I. Wang, S. Andersson-Engels, S. Svanberg, and K. Svanberg, "Laser-induced fluorescence diagnostics of basal cell carcinomas of the skin following topical ALA application," Biomedical Optics Newsletter **5**, 1-6 (1996)

J. Olsrud, R. Wirestam, S. Brockstedt, A. M. K. Nilsson, K. -G. Tranberg, S. Holtås, F. Ståhlberg, and B. R. Persson, "Use of the proton resonance frequency shift method in phantoms: application to interstitial laser thermotherapy," manuscript for Phys. Med. Biol. (1997)

An invited review paper written in Swedish:

A. Nilsson, "Framtida alternativ för cancerbehandling," Ung Forskning **1**, 48-50 (1995)

3. Introduction

Most of us have personal associations with cancer and cardiovascular diseases. This is not so surprising considering the alarming numbers presented in WHO's World Health Report 1997, stating that 33% and 12% of all deaths world wide are caused by circulatory diseases and cancers, respectively. Beside infectious and parasitic diseases, they represent the two most common causes of death. While other fatal disorders have been gradually eliminated, the risk of developing these two diseases is steadily growing. Thus, there exists an urgent need for new, efficient treatment modalities and diagnostic techniques.

The laser, clinically available since the 1960's,¹ was almost immediately shown to have properties useful for medical applications. It yields monochromatic, non-ionising light, which can target and be absorbed by specific biomolecules, leaving other molecules more or less unaffected. This results in selective, specific and comparatively harmless interactions between the light and medium, of importance from a clinical point of view. Laser light can also easily be focused into spots of different sizes, thus providing variable probing areas, resulting in radiation doses which can be made extremely intense. The latter possibly very high when required. This in combination with the flexibility and the minimally invasive character provided by the use of optical fibres, resulted in lasers soon being recognised as a potential option both for therapy and diagnostics of cardiovascular diseases and tumours.

In the case of *therapy*, clear and preferably selective photobiological effects should be induced by the laser light. This is achieved by the transformation of light energy into either chemical, thermal or mechanical energy via resonant light absorption,² causing direct and delayed selective cell death. Photochemical processes often require long exposure times (in the order of 1000 s) and low power densities (typically 0.1 W/cm²). Thermal effects are efficiently induced at long to intermediate exposure times (>0.001 s) and intermediate power densities (10⁰-10⁶ W/cm²) and photomechanical effects will be induced by short pulses (10⁻⁶-10⁻⁹ s) in combination with high power densities (10⁹-10¹² W/cm²). Photodynamic therapy (PDT), thermotherapy and tissue ablation are treatment modalities, each involving one of these three interaction processes described.

The light-tissue interactions in the *diagnostics* approach must in contrast be non-destructive, meaning a resonant light absorption that is below the threshold required to induce chemical and thermal reactions. The key words for tissue diagnostics are instead light scattering and re-emission. By analysing the features of the scattered and re-emitted light in terms of wavelength, temporal and spatial/angular distributions, indirect information can be gained from multiple scattering tissues, such as: the quantity of essential and characteristic tissue biomolecules, average cell size and on the presence of domains embedded in the tissue with divergent optical properties. There exists a variety of potential methods,³ either based on resonant light absorption followed by re-emission, such as laser-induced fluorescence (LIF), non-resonant inelastic scattering in conjunction with Raman spectroscopy, or on elastic scattering, such as flow cytometry, diffuse reflection spectroscopy, absorption spectroscopy and time resolved transmittance or reflectance spectroscopy.

By choosing appropriate parameters such as those of light intensity, irradiation geometry, wavelength, exposure time and exposure mode (pulsed or continuous), the desired light-tissue interaction can be determined for optimal treatment, or diagnostic conditions. The choice of these physical irradiation parameters of the treatment or probe light, is indirectly a way of designing the resulting light scattering and absorption in the tissue, in order to generate not only suitable interactions between the light and tissue but also appropriate penetration depths. This requires rigorous knowledge of the absorption and scattering properties of tissue, or in other words of fundamental tissue optics - the central issue of this work.

Tissue optics deals primarily with two problems, which we can refer to as the *direct* and *indirect* problems emerging in connection with laser-based treatments (direct) and diagnostics (indirect), respectively. The direct problem concerns the estimation of the energy density [J m^{-3}] of the impinging light reaching a certain position within the tissue, for example a malignant area embedded in healthy tissue, when the optical absorption and scattering properties are known. This can be solved by measuring the optical properties of the tissue, including those of the malignancy, and computing the resulting light flux both in- and outside the tissue, employing one of the many numerical methods available for computations of light propagation in tissue. The determination of the optical properties of tissue is thus a central part of tissue optics.

In the indirect problem the unknowns are instead the optical parameters, to be determined from the measured distribution of reflected and/or transmitted light. This often involves extensive computations based on the same numerical methods as those in the direct problem, though iteratively repeated. From the deduced optical properties important information can be gained concerning morphological and physiological parameters of the tissue, related to its health. Investigating the relationship between the optical properties and the microscopical properties of the tissue is therefore an essential and growing area within tissue optics.

This work comprises studies of the absorption and scattering properties of tissue, with emphasis on one of the main absorbers in tissue - the optically very characteristic blood, which is more or less present in all tissue. These studies were partly performed from a theoretical point of view as summarised in Chapters 4 and 5, as well as from an experimental view point described in Chapter 6, and all the way to clinical applications as discussed in Chapters 8 and 9. The experimental part, described in Chapter 6, included measurements of the optical properties employing integrating sphere set-ups. These results were further analysed by relating them to microscopic properties of the tissue, which is discussed in Chapter 7.

4. Light propagation in tissue - theory and models

4.1 Introductory overview

The duality of light - waves/particles - is also apparent within tissue optics. The aspect of which depends on the phenomenon being studied. If we are investigating the light passing through a dense and thick tissue, as for instance in conjunction with trans-illumination of breast tissue, most of the properties associated with the wave characteristics are lost. A model treating the light propagation as a stream of energy quanta, disregarding the typical wave properties, is then appropriate. This is in contrast to light propagation through a completely amorphous medium, as for instance glass, where the polarisation and interference phenomena, etc. are apparent due to the regular structure. However, when light is passing through a tissue with a certain more regular structure, for instance muscle tissue with its elongated cells, or flowing blood as disc shaped cells, a characteristic asymmetry can often be found in the angular distribution of the scattered light. Due to the collective alignment, the asymmetric characteristics of the scattering from the individual cells are not fully averaged out. This asymmetry can be traced to the asymmetric shape of the individual cells, a phenomenon which can be taken into account using the wave properties of light.

Light propagation in tissue might be envisioned as a stream of particles, photons, each with a localised quantum of energy. The statistical average transport of photons and their energy through turbid medium, such as tissue, can mathematically be expressed by the radiative transport (RT) equation.⁴ It is heuristically derived by considering the energy balance of incoming, outgoing, absorbed and emitted photons of an infinitesimal volume element in the medium, in the very same way as the Boltzmann particle transport equation is derived for heat in a heat conducting medium, and neutrons in a reactor element, etc..⁵ The RT equation is valid in an isotropic and quasi-homogeneous medium, meaning that the optical inhomogeneities are small and uniformly distributed throughout the material. Thus, the tissue is assumed to be a homogeneous matrix containing randomly distributed absorption and scattering centres, simply represented by three parameters: the absorption and scattering coefficients, μ_a and μ_s , as well as the scattering anisotropy factor, g . This is schematically depicted in Figure 4.1a. Each local scattering and absorption centre can be thought of as corresponding to a statistical average of several scattering and absorption events, respectively, due to the cell membranes, organelles, and chromophore molecules. Typical wave

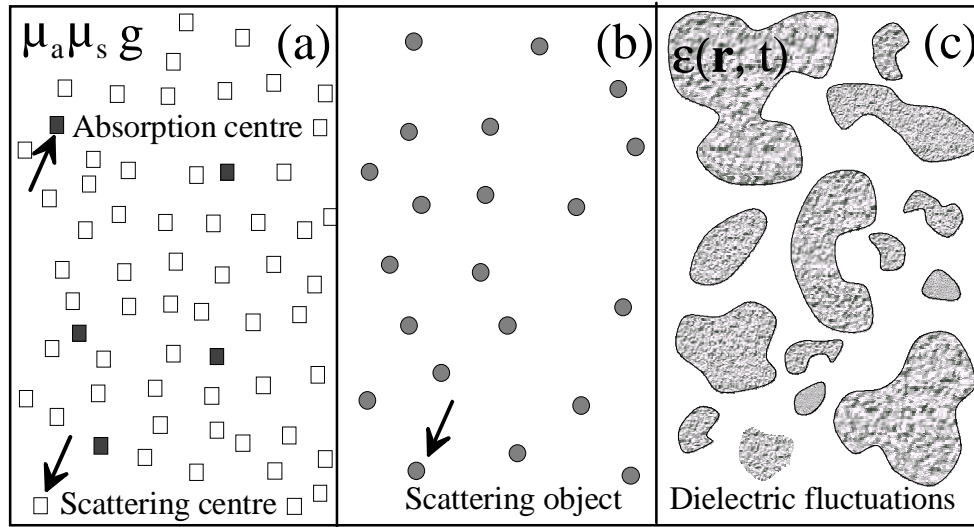


Figure 4.1 Schematic picture of (a) the radiative transport theory and (b), (c) the electromagnetic theory. The former treats the tissue as it would if it contained randomly distributed scattering and absorption centres, while the latter regards tissue as either an ensemble of single scattering particles (b) or as a medium with random dielectric fluctuations (c).

properties, such as polarisation, diffraction and interference, are here neglected. The approach used in transport theory is to add powers rather than fields.

Since there are no analytical solutions available to the transport equation, approximations and/or numerical techniques must be developed and utilised. There exist a wide variety of approximative methods, appropriate for various applications and valid for different optical properties of the modelled tissue. Common for all is that the distribution of the photon energy is expressed by radiometric quantities, *i.e.* passively detectable and measurable parameters. This indicates the practical foundation of radiative transport theory and its close relation to applications and measurements. Computations of light distributions within tissue and tissue phantoms, based on the transport equation, have proven to correspond closely with measured values.⁶⁻⁸ Numerical methods for light propagation, derived from the radiative transport theory, are therefore the most widely employed within tissue optics. However, since the individual scattering and absorption events are collectively represented by scattering and absorption centres, these methods result in a loss of detailed information on fundamental microscopic tissue parameters, concerning tissue physiology and morphology. This indicates that the radiative transport theory is not complete enough to describe light transport in highly structured tissue, such as muscle tissue with its extended muscle fibres, or aligned, flowing disc-shaped blood cells. When morphological parameters such as cell size, shape and alignment are of interest, it is necessary to use more rigorous models.

Alternatively, we can adopt the classical approach and imagine light propagation as a continuous transfer of energy by electromagnetic waves. This is rigorously treated by Maxwell's equations, which are part of the fundamental laws of physics. The light

propagation is mathematically represented by vector waves, being scattered and absorbed in the medium. In tissue optics, two types of media are of particular interest, *i.e.* one consisting of discrete scattering particles and one of a random continuum, as depicted in Figure 4.1b and c. Light propagation in a suspension of well-separated independently scattering particles (Figure 4.1b) is comparatively easy to describe mathematically, since only light from one single particle has to be considered. The approximate light distribution of a collection of particles is then obtained by adding the individual fields. This approach is frequently used to theoretically study light scattering by diluted blood⁹ and tissue phantoms containing silica, or latex spheres and lipid vesicles.¹⁰⁻¹⁶ If the particles are suspended at higher concentrations, multiple scattering must be taken into account. The single particle solution has to be supplemented by adding a "perturbation" factor from the surrounding waves originating from all other particles.⁴ This leads to a complicated formalism without any solutions to the important case of multiple scattering by tissue.

A more realistic model for dense tissue in general, is by representing the physical microstructure, *e.g.* the chromophores, intra- and extra- cellular plasma, cell membranes and organelles, by random dielectric fluctuations given by a dielectric function, $\epsilon(\mathbf{r}, t)$,⁴ as schematically depicted in Figure 4.1c. This function must be for all positions \mathbf{r} and times t , in order to be able to deduce the internal and external electromagnetic fields. Considering the complex and disordered microscopic structure of tissue, the task to determine $\epsilon(\mathbf{r}, t)$ as a true and complete representation of the tissue appears immense. Consequently, there have been no attempts to do so within the tissue optics field, though it has proven to be possible for simpler media within other disciplines, *e.g.* atmospheric and ocean optics.⁴ Thus, this procedure is not yet applicable to multiple scattering tissue. In practice, it presently leaves us with the discrete single-scatterer model, within electromagnetic theory, as the only reasonably appropriate approach.

In this chapter, theoretical models important for applications within tissue optics, either founded on the frequently employed radiative transport theory or the fundamental electromagnetic theory, are summarised. To extensively study the mathematical formulations behind light propagation in tissue might at first seem exaggerated and distant from our aim to be able to better diagnose and treat diseased tissue utilising laser light. However, such an approach often produces important and potentially critical insights into to what applications the different models are useful for and the validity of computational results.

4.2 Radiative transport theory

Three parameters represent and quantify the light-tissue interaction processes in transport theory: the absorption coefficient μ_a [mm^{-1}], the scattering coefficient μ_s [mm^{-1}] and the g -factor. The two first mentioned coefficients reveal their meaning by their names; the absorption coefficient is the probability of absorption per unit path length of a travelling photon and the scattering coefficient is defined correspondingly for the scattering process. The optical properties vary significantly with wavelength and tissue type. Typical values for tissue, with the highly absorbing blood as one of the exceptions, are in the order of 0.2 mm^{-1} for the absorption coefficient and 25 mm^{-1} for the scattering coefficient in the visible spectral range.¹⁷ This means that a photon has a path length of on average 5 mm in the tissue before it is absorbed and a range of approximately 0.04 mm between two scattering

events. Adding these two interaction coefficients yields the so-called total attenuation coefficient, μ_t , which accounts for the probability of all light-tissue interactions per unit path length of a propagating photon. The g-factor, also named the anisotropy or asymmetry factor, is defined as the average cosine of the deflection angle θ at a “single scattering event” (see Figure 4.2), in terms of the transport theory and is then simply a measure of the angular distribution of the scattered light. A g-factor close to zero reflects that the scattering is isotropic, while a value close to unity indicates a sharply scattering peak in the forward direction. Tissue has in general a forward directed scattering¹⁸⁻²⁰ and typical values of the g-factor are thus in the range 0.8-0.95.¹⁷ An expression for the effective scattering should include both the scattering coefficient and the asymmetry factor. It is often quantified by the reduced or effective scattering coefficient:

$$\text{Eq. 4.1} \quad \mu_s' = \mu_s(1-g).$$

More substantial information on the angular distribution of the scattered light is provided by the phase function $p(\mathbf{s}, \mathbf{s}') = p(\cos\theta)$, where \mathbf{s} and \mathbf{s}' are unit vectors in the directions of incident and scattered light respectively, as shown in Figure 4.2. The phase function is a probability density function, which defines the probability of a photon being scattered between the deflection angles θ and $\theta + \Delta\theta$, divided by $\Delta\theta$, for each radiative transport scattering event. We have here assumed that the scattering of a photon is only dependent on the zenith deflection angle θ $[0, \pi]$ between the two vectors \mathbf{s} and \mathbf{s}' . The scattering about the incident direction versus the other spherical angle, *i.e.* the azimuthal angle ϕ shown in Figure 4.2, is considered to be symmetric and uniformly distributed between 0 and 2π . This corresponds to the assumption of the tissue being an isotropic medium, *i.e.* without any major tissue regions with more organised structures. The phase function is usually determined empirically. The most frequently used function for tissue is the

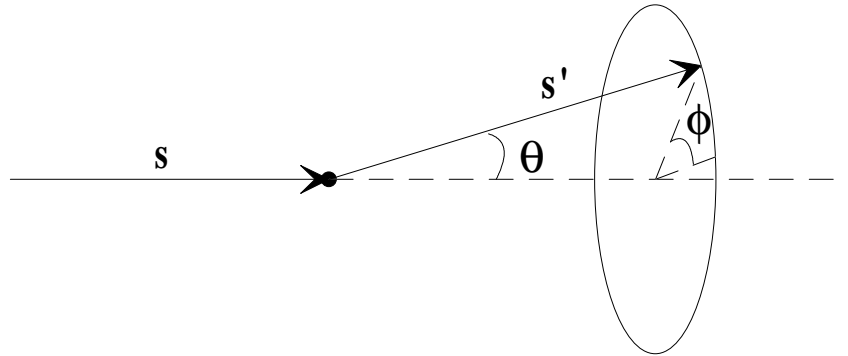


Figure 4.2 Geometrical definitions at an interaction site used in the development of transport theory. The unit vectors, \mathbf{s} and \mathbf{s}' , represent the directions of the incident and scattered light respectively.

Henye-Greenstein function, since it has been shown to agree reasonably well with measured angular distributions obtained from dense tissue, such as skin and aorta:^{18,19}

$$\text{Eq. 4.2} \quad p(\mathbf{s}, \mathbf{s}') = p(\cos\theta) = \frac{(1 - g^2)}{4\pi(1 + g^2 - 2g \cos\theta)^{3/2}}.$$

This function was originally derived to describe scattering of starlight by interstellar matter.²¹ It is normalised to unity on being integrated over a solid angle of 4π . In Eq. 4.2, we can recognise the previously mentioned g -factor, which accounts for the asymmetry in the angular distribution of the scattered light. The formal definition for the mean cosine of the deflection angle is

$$\text{Eq. 4.3} \quad g = \iint_{4\pi} \mathbf{s} \cdot \mathbf{s}' p(\mathbf{s}, \mathbf{s}') d\Omega',$$

where $d\Omega'$ is an infinitesimal element of the solid angle.

A more general expression for the phase function can be formulated as an expansion series in Legendre polynomials $P_n(\mathbf{s}, \mathbf{s}')$:²²

$$\text{Eq. 4.4} \quad p(\mathbf{s}, \mathbf{s}') = \frac{1}{4\pi} \sum_{n=0}^{\infty} (2n+1) b_n P_n(\mathbf{s}, \mathbf{s}')$$

with the expansion coefficients b_n given by:

$$\text{Eq. 4.5} \quad b_n(\mathbf{r}) = \iint_{4\pi} p(\mathbf{s}, \mathbf{s}') P_n(\mathbf{s}, \mathbf{s}') d\Omega'.$$

The first order Legendre polynomials are:

$$\text{Eq. 4.6} \quad P_0(x)=1; \quad P_1(x)=x; \quad P_2(x)=\frac{1}{2}(3x^2-1); \quad P_3(x)=\frac{1}{2}(5x^3-3x).$$

Truncation after the first term in the expansion series in Eq. 4.4, results in a phase function describing isotropic scattering (Eq. 4.4 with $n=0$ and $b_0=1$, which follows from Eq. 4.5 using Eq. 4.6 and the normalisation of the phase function to unity):

$$\text{Eq. 4.7} \quad p(\mathbf{s}, \mathbf{s}') = \frac{1}{4\pi},$$

i.e. equal probability for the photon to be scattered in all directions at each scattering event. When two terms are used in the expansion series, a slightly more forward directed phase function is obtained, which is used to describe diffuse light transport ($b_1=g$, which follows from Eq. 4.5 using Eq. 4.6 and Eq. 4.3):

$$\text{Eq. 4.8} \quad p(\mathbf{s}, \mathbf{s}') = \frac{1}{4\pi} (1+3g \mathbf{s} \cdot \mathbf{s}').$$

Due to the forward-directed nature of the light scattering in tissue, this two-term phase function is sometimes complemented with a Dirac function, $\delta(\mathbf{s}-\mathbf{s}')$,^{23,24} where the fraction f determines the degree of asymmetry:

$$\text{Eq. 4.9} \quad p(\mathbf{s}, \mathbf{s}') = f \delta(\mathbf{s}-\mathbf{s}') + \frac{(1-f)}{4\pi} (1+3g \mathbf{s} \cdot \mathbf{s}').$$

This phase function is called the δ -Eddington phase function. The general formulation provided by the expansion in Legendre polynomials, can also be applied to the Henyey-Greenstein function, resulting in expansion coefficients equal to g^n (which follows from Eq. 4.5, using Eq. 4.6 and Eq. 4.3, and the normalisation of the phase function to unity). The expansion series of the Henyey-Greenstein function is then given by:

$$\text{Eq. 4.10} \quad p(\mathbf{s}, \mathbf{s}') = p(\cos\theta) = \frac{1}{4\pi} \sum_{n=0}^{\infty} (2n+1) g^n P_n(\cos\theta).$$

Other phase functions have also been suggested, including: a Mie phase function,²⁵ a Rayleigh-Gans form function²⁶⁻²⁸ and a two-parametric Reynolds-McCormick phase function.^{29,30} The latter is also named the Gegenbauer kernel function,³¹ since it can be expanded in so-called Gegenbauer polynomials rather than Legendre polynomials.

When the parameters of light-tissue interaction have clearly been defined, it is fairly straight forward to formulate the central equation of transport theory, the radiative transport equation. This was originally carried out in terms of a general

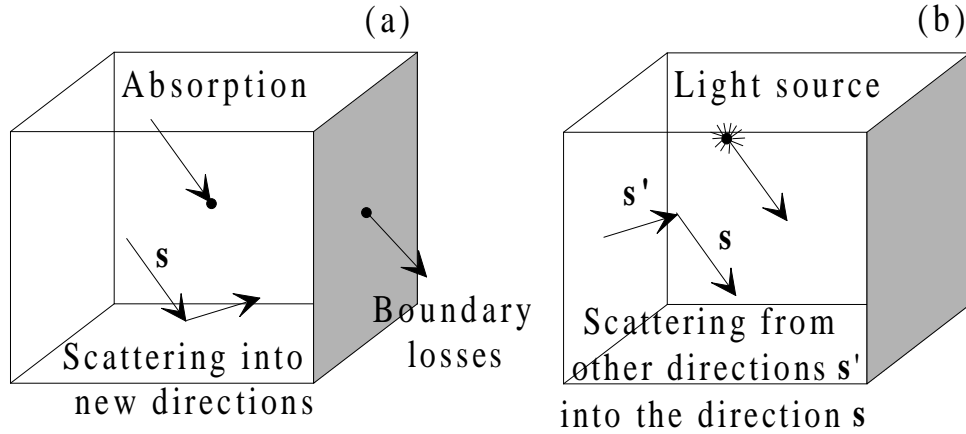


Figure 4.3 The derivation of the radiative transport equation is illustrated as the (a) losses and the (b) gain of the radiance in a infinitesimal volume unit.

particle distribution function $\Psi(\mathbf{r}, \mathbf{s}, t)$, *i.e.* number of particles per unit volume and unit solid angle [$\text{m}^{-3} \text{sr}^{-1}$] travelling in the direction \mathbf{s} at the position \mathbf{r} and time t .⁵ The assumption being for this derivation is that the energy of the particle is, on the average, unchanged at each interaction event. Thus, we restrict the analysis to the transport of monochromatic photons. Within the tissue optics field, it is preferable to express the distribution of photons in a radiometric (detectable) parameter, instead of in the number of photons per unit volume and solid angle. The radiance $L(\mathbf{r}, \mathbf{s}, t)$ [$\text{W m}^{-2} \text{sr}^{-1}$] is often used and simply obtained by multiplying the particle distribution function with the photon energy

and the speed of the photons, v , *i.e.* the speed of light in vacuum divided by the refractive index of the tissue. The radiative transport equation can then be expressed as follows:⁴

$$\text{Eq. 4.11} \quad \frac{1}{v} \frac{\partial L(\mathbf{r}, \mathbf{s}, t)}{\partial t} + \mathbf{s} \cdot \nabla L(\mathbf{r}, \mathbf{s}, t) + (\mu_s + \mu_a) L(\mathbf{r}, \mathbf{s}, t) = \mu_s \iint_{4\pi} L(\mathbf{r}, \mathbf{s}', t) p(\mathbf{s}, \mathbf{s}') d\Omega' + Q(\mathbf{r}, \mathbf{s}, t).$$

If we observe an infinitesimal volume element at \mathbf{r} and time t , we soon realise that the transport equation formulates the energy balance in that element, as schematically illustrated in Figure 4.3. On the left-hand side of Eq. 4.11, the first term represents the temporal change in the number of photons with the direction \mathbf{s} . The second term corresponds to the spatial loss of photons in the direction \mathbf{s} , escaping the observed volume element through its boundary surfaces. The last term on the left-hand side accounts for the photons lost through resonant absorption, as well as scattering of photons of the direction \mathbf{s} to any other

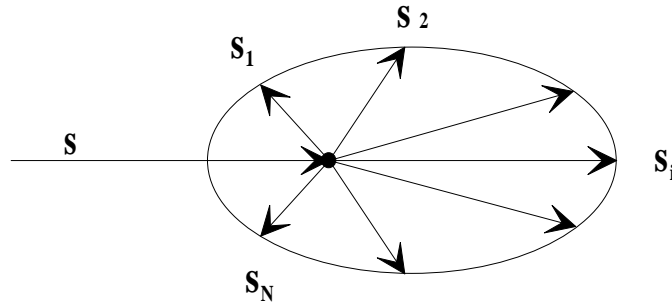


Figure 4.4 The radiance can be discretised in angular components along the directions $\mathbf{s}_1, \mathbf{s}_2, \dots, \mathbf{s}_i, \dots, \mathbf{s}_N$.

direction. On the right hand side of Eq. 4.11, we first have a term representing the photons being scattered from the direction \mathbf{s}' into the direction \mathbf{s} , *i.e.* the gained photons. Finally, there is a source term $Q(\mathbf{r}, \mathbf{s}, t)$ [$\text{Wm}^{-3} \text{sr}^{-1}$] giving the number of photons generated by a light source. Thus, the fundamental meaning of Eq. 4.11 is that the number of lost photons equals the number of gained photons, in other words energy conservation.

The transport equation is formulated and the next step is to find its solution. Since no analytical solutions are available, we have to derive it by employing approximations and numerical solutions. There are a wide range of methods used within tissue optics, which essentially can be grouped under the names discretisation, expansion and probabilistic methods. Those most important will briefly be described here, starting with the discretisation methods.

4.2.1 Discretisation methods

Integro-differential equations without any analytical solutions are often numerically solved by discretisation. The accuracy of the solution obtained is then governed by the number of discretisation terms included. Let us now for simplicity disregard from the time dependency

of the radiance. A discretisation of the transport equation is obtained when the radiance is discretised in N angular components, *i.e.* $L(\mathbf{r}, \mathbf{s})$ with $\mathbf{s}=\mathbf{s}_1, \mathbf{s}_2, \dots, \mathbf{s}_i, \dots, \mathbf{s}_N$, as depicted in Figure 4.4. This method within transport theory is referred to as the *discrete ordinates method*, or the *N-flux method*.^{4,32} From this follows the discretised transport equation:

$$\text{Eq. 4.12} \quad \mathbf{s}_i \cdot \nabla L(\mathbf{r}, \mathbf{s}_i) + (\mu_s + \mu_a) L(\mathbf{r}, \mathbf{s}_i) = \mu_s \sum_{j=1}^N w_j L(\mathbf{r}, \mathbf{s}_j) p(\mathbf{s}_i, \mathbf{s}_j) + Q(\mathbf{r}, \mathbf{s}_i),$$

where $w_1, w_2, \dots, w_j, \dots, w_N$ are the corresponding weighting factors, dependent on the numerical method used to substitute the integral in Eq. 4.11 with the summation in Eq. 4.12. The transport equation can then be converted into a matrix differential equation, which is solved utilising an eigenvalue - eigenvector method. However, this requires extensive computations and is rarely used (a seven/twenty four-flux model, *i.e.* $N=7$ or 24 in Eq. 4.12, was utilised in the earlier days of tissue optics^{19,33,34}).

The complexity is substantially reduced by taking only two angular components of the radiance into account, *i.e.* in the forward and reverse directions, yielding the *one-dimensional transport equation* based on the *two-flux theory* ($N=2$ in Eq. 4.12).³⁵ This is equivalent to a one-dimensional approximation of the tissue, which can be thought of as a line along the z -axis. We therefore cannot talk about solid angles and must instead express the transport equation in terms of irradiance $I(z, \mathbf{s})$ [W m^{-2}], where \mathbf{s} equals either one of the unity vectors \mathbf{z} or $-\mathbf{z}$. The transport equation is then reduced to the following set of differential equations:

$$\begin{aligned} \text{Eq. 4.13} \quad \frac{\partial I(z, \mathbf{z})}{\partial z} + (\mu_{s1D} + \mu_{a1D}) I(z, \mathbf{z}) &= \mu_{s1D} I(z, \mathbf{z}) p(\mathbf{z}, \mathbf{z}) + \mu_{s1D} I(z, -\mathbf{z}) p(\mathbf{z}, -\mathbf{z}) \\ &\quad \mathbf{s}=\mathbf{z} \end{aligned}$$

$$\begin{aligned} \text{Eq. 4.14} \quad -\frac{\partial I(z, -\mathbf{z})}{\partial z} + (\mu_{s1D} + \mu_{a1D}) I(z, -\mathbf{z}) &= \mu_{s1D} I(z, -\mathbf{z}) p(-\mathbf{z}, -\mathbf{z}) + \mu_{s1D} I(z, \mathbf{z}) p(-\mathbf{z}, \mathbf{z}) \\ &\quad \mathbf{s}=-\mathbf{z}, \end{aligned}$$

where μ_{s1D} and μ_{a1D} are the one-dimensional scattering and absorption coefficients. Tissue can often be considered as an isotropic medium, *i.e.* the scattering probability of a photon propagating in one direction being scattered into another does not depend on the initial propagation direction. Hence, $p(\mathbf{z}, -\mathbf{z}) = p(-\mathbf{z}, \mathbf{z})$ and $p(\mathbf{z}, \mathbf{z}) = p(-\mathbf{z}, -\mathbf{z})$. As the one-dimensional analysis allows photon propagation in only two directions, $\mathbf{s}=\mathbf{z}$ and $\mathbf{s}=-\mathbf{z}$, it follows that $p(\mathbf{z}, \mathbf{z}) + p(-\mathbf{z}, \mathbf{z}) = 1$ and $p(-\mathbf{z}, -\mathbf{z}) + p(\mathbf{z}, -\mathbf{z}) = 1$. Using these equalities together with the definition of the back scattering probability S :

$$\text{Eq. 4.15} \quad S = \mu_{s1D} p(-\mathbf{z}, \mathbf{z}) = \mu_{s1D} p(\mathbf{z}, -\mathbf{z}),$$

the final expression for the one-dimensional transport equation is obtained:

$$\text{Eq. 4.16} \quad \frac{\partial I(z, \mathbf{z})}{\partial z} = -(\mu_{a1D} + S)I(z, \mathbf{z}) + SI(z, -\mathbf{z}) \quad \mathbf{s}=\mathbf{z}$$

$$\text{Eq. 4.17} \quad -\frac{\partial I(z, -\mathbf{z})}{\partial z} = -(\mu_{a1D} + S)I(z, -\mathbf{z}) + SI(z, \mathbf{z}) \quad \mathbf{s}=-\mathbf{z}.$$

These equations can be identified with those used in the *Kubelka-Munk* approach^{36,37} ($K_{KM}=\mu_{a1D}$ and $S_{KM}=S$) derived for two diffuse light fluxes propagating in the forward and backward directions assuming diffuse irradiation. Star and van Gemert *et al.*^{22,38} have shown how the one-dimensional interaction coefficients, μ_{a1D} and μ_{s1D} , are related to the volumetric optical properties, if significantly higher effective scattering coefficient than the absorption coefficient is assumed:

$$\text{Eq. 4.18} \quad \mu_a = \frac{1}{2} \mu_{a1D}$$

$$\text{Eq. 4.19} \quad \frac{3}{4} (1-g)\mu_s - \frac{1}{4} \mu_a = \mu_{s1D} \quad p(-\mathbf{z}, \mathbf{z}) = S.$$

The general solutions of Eq. 4.16 and Eq. 4.17 are of the form:²⁶

$$\text{Eq. 4.20} \quad I(z, \mathbf{z}) = A e^{(-\alpha z)} + A' e^{(\alpha z)}$$

$$\text{Eq. 4.21} \quad I(z, -\mathbf{z}) = B e^{(-\alpha z)} + B' e^{(\alpha z)},$$

where α is given by:

$$\text{Eq. 4.22} \quad \alpha = \sqrt{\mu_{a1D}^2 + 2\mu_{a1D}S} = \sqrt{3\mu_a(\mu_a + \mu_s(1-g))} = \sqrt{3\mu_a\mu_{tr}},$$

where μ_{tr} is the so-called transport coefficient. The constants A, A', B and B' are determined from the boundary conditions, *i.e.* from the reflectance and transmittance. The formal definition for the reflectance at a boundary surface with a unit vector \mathbf{n} , pointing into the medium, is:

$$\text{Eq. 4.23} \quad R = - \int_{\mathbf{s} \cdot \mathbf{n} < 0} \mathbf{s} \cdot \mathbf{n} L(\mathbf{r}_{\text{boundary}}, \mathbf{s}) d\Omega,$$

with an analogous definition for the transmittance.

An even simpler case would be to study the irradiance only in one direction, let us say in the propagation direction of a collimated beam along the z-axis, $\mathbf{s}=\mathbf{z}$, disregarding the impact of

the diffusely scattered light. An expression for the collimated transmitted light can then be derived from the transport equation, excluding the terms associated to the diffusely scattered irradiance. The transport equation is then reduced to

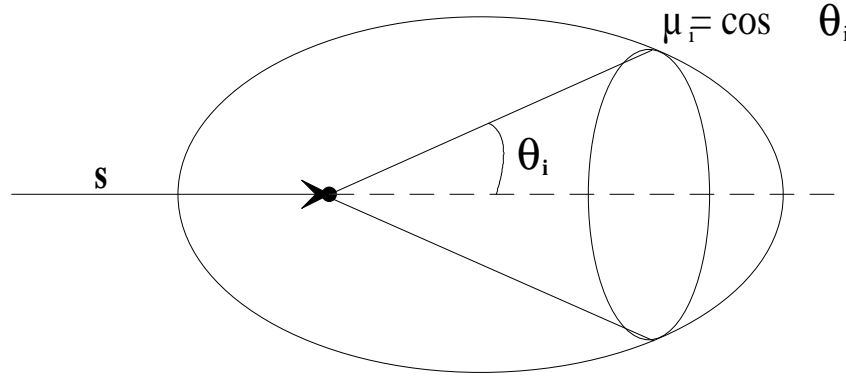


Figure 4.5 The radiance can be discretised by cones characterised by $\mu_i = \cos \theta_i$ and $\phi = [0, 2\pi]$.

$$\text{Eq. 4.24} \quad \frac{\partial I(z, \mathbf{z})}{\partial z} = -(\mu_s + \mu_a) I(z, \mathbf{z}),$$

which can be recognised as the *Beer-Lambert law*. The solution is a simple exponential expression:

$$\text{Eq. 4.25} \quad I(z, \mathbf{z}) = I_{\text{col}}(z) = I(z=0) \exp[-(\mu_s + \mu_a)z].$$

Alternatively, the discretisation of the radiance can be performed in terms of N cones quantified by $\mu_i = \cos \theta_i$ and $\phi = [0, 2\pi]$ as shown in Figure 4.5, *i.e.* in azimuthally averaged radiance components $L(\mathbf{r}, \mu_i)$, in contrast to the previous mentioned angular components in discrete directions. The phase function is then substituted by a redistribution matrix with elements, $h(\mu_i, \mu_j)$, corresponding to the fraction of incident light in a cone μ_i , which is scattered into a cone μ_j . The *adding-doubling method* is based on this discretisation for a slab of tissue, thin along the z -axis and of infinite extent in the xy -plane.^{35,39} The thickness of the slab should be so small that the integration of the radiance along the z -axis can be approximated by an average of the radiances at the top and bottom of the layer. This is necessary to be able to solve the time-independent, discrete, azimuthally averaged transport equation:

$$\begin{aligned} \text{Eq. 4.26} \quad & \mu_i \frac{\partial L(z, \mu_i)}{\partial z} + (\mu_s + \mu_a) L(z, \mu_i) = \\ & = \mu_s \sum_{j=1}^N w_j \left[h(\mu_i, \mu_j) L(z, \mu_j) + h(\mu_i, -\mu_j) L(z, -\mu_j) \right]. \end{aligned}$$

The weighting factors w_j are determined by the numerical integration procedure selected. This equation can be solved via integration over the thickness, $t_1 - t_0 = \Delta t$, of the thin slab:

$$\begin{aligned} \mu_i [L(t_1, \mu_i) - L(t_0, \mu_i)] + (\mu_s + \mu_a) \Delta t L_{1/2}(\mu_i) = \\ \text{Eq. 4.27} \quad = \mu_s \sum_{j=1}^N w_j \Delta t [h(\mu_i, \mu_j) L_{1/2}(\mu_j) + h(\mu_i, -\mu_j) L_{1/2}(-\mu_j)], \end{aligned}$$

where $L_{1/2}$ represents the previously mentioned approximation of the integral:

$$\text{Eq. 4.28} \quad L_{1/2}(\mu_i) = \frac{1}{2} [L(t_0, \mu_i) + L(t_1, \mu_i)].$$

This results in an expression dependent on the radiance at the top, t_0 , and bottom, t_1 , of the slab, which consequently are the only parameters that can be determined. The adding-doubling method is thus mainly used to compute the reflectance and transmittance rather than the radiance inside the tissue. The results from a slab with a thickness twice as thick as the initial thin layer are obtained by summing the contributions from each individual slab. This can be repeated until the true physical thickness is reached.

4.2.2 Expansion methods

A formal method to solve a differential equation is to find the solution to its homogeneous part and expand the general solution in terms of the homogeneous solution obtained. This eigenvector - eigenvalue problem has for the transport equation been treated by Case⁴⁰ and Case and Zweifel,⁵ but has never really been applied to tissue optics.

A simpler approach than using the rather complex eigenfunctions, would be to expand the radiance using a well-known appropriate function series.⁵ Considering the angular distribution of diffusely scattered light, a realistic choice of orthogonal expansion functions for the diffuse radiance would be spherical harmonics. Legendre polynomials $P_n(x)$ (see Eq. 4.6) have proven to be well-suited to axial-symmetric tissue geometry.^{5,22} This implies that the radiance must first be separated into one primary, collimated part, L_c , and one scattered part, L_s :

$$\text{Eq. 4.29} \quad L(\mathbf{r}, \mathbf{s}) = L_c(\mathbf{r}, \mathbf{s}) + L_s(\mathbf{r}, \mathbf{s}),$$

where the collimated part fulfils Beer-Lambert's law:

$$\text{Eq. 4.30} \quad \frac{\partial L_c(\mathbf{r}, \mathbf{s})}{\partial s} = -\mu_t L_c(\mathbf{r}, \mathbf{s}).$$

The expansion of $L_s(\mathbf{r}, \mathbf{s})$ and its expansion coefficients L_n are given by

$$\text{Eq. 4.31} \quad L_s(\mathbf{r}, \mathbf{s}) = \sum_{n=0}^{\infty} (2n+1) L_n(\mathbf{r}) P_n(\mathbf{r}, \mathbf{s})$$

$$\text{Eq. 4.32} \quad L_n(\mathbf{r}) = \iint_{4\pi} L_s(\mathbf{r}, \mathbf{s}') P_n(\mathbf{r}, \mathbf{s}') d\Omega'$$

The regular normalisation factor $(4\pi)^{-1}$ is not included in Eq. 4.31, since by convention³⁵ it is instead taken into account in Eq. 4.36 below. Also the phase function $p(\mathbf{s}, \mathbf{s}')$ is expanded in Legendre polynomials by employing Eq. 4.4 and Eq. 4.5.

By the use of Eqs. 4.4, 4.11, 4.30 and 4.31,²² the stationary radiative transport equation expanded in Legendre polynomials can be derived using:

$$\begin{aligned} \text{Eq. 4.33} \quad & \mathbf{s} \cdot \nabla L_s(\mathbf{r}, \mathbf{s}) + (\mu_s + \mu_a) L_s(\mathbf{r}, \mathbf{s}) = \\ & \frac{\mu_s}{4\pi} \sum_{i=0}^{\infty} \sum_{j=0}^{\infty} \iint_{4\pi} (2i+1) L_i(\mathbf{r}) P_i(\mathbf{r}, \mathbf{s}') (2j+1) b_j P_j(\mathbf{s}, \mathbf{s}') d\Omega' + \\ & + \frac{\mu_s}{4\pi} \sum_{j=0}^{\infty} (2j+1) b_j P_j(\mathbf{s}, \mathbf{s}') L_c(\mathbf{0}, \mathbf{0}) e^{(-\mu_s \cdot \mathbf{s})}. \end{aligned}$$

The last term originates from the collimated radiance, with an initial value of $L_c(\mathbf{0}, \mathbf{0})$, which can be regarded as a source of the scattered radiance.

A set of differential equations is finally obtained by using the stratagem of multiplying the transport equation by $P_n(\mathbf{s}, \mathbf{s}')$. This is followed by an integration over all directions \mathbf{s} and finally employing the addition theorem for Legendre polynomials.^{5,32,35} As with all infinite theoretical expansions, the series of Legendre polynomials must be truncated keeping terms 0, 1, 2, ..., N. This approximation is in general called the *P_N-approximation*.^{5,22,32,35} Truncation after one term corresponds to the assumption of isotropic light scattering, according to Eq. 4.7. If only the first two terms are retained, we are applying the phase function in Eq. 4.8 and the *P₁-approximation*, better known as the *diffusion approximation*. It results in a set of two differential equations, which when combined can be rewritten as the diffusion equation.^{4,41,42} The time-dependent version is often written as³⁵

$$\text{Eq. 4.34} \quad \frac{1}{v} \frac{\partial \Phi(\mathbf{r}, t)}{\partial t} = D \nabla^2 \Phi(\mathbf{r}, t) - \mu_a(\mathbf{r}) \Phi(\mathbf{r}, t) + S_0(\mathbf{r}, t)$$

where $\Phi(\mathbf{r}, t)$ is the fluence rate ($= \iint L(\mathbf{r}, \mathbf{s}, t) d\Omega$) and $S_0(\mathbf{r}, t)$ is a source term. The diffusion coefficient D is defined by

$$\text{Eq. 4.35} \quad D = [3(\mu_a + \mu_s(1-g))]^{-1}$$

The scattered radiance can then be expressed by

$$\text{Eq. 4.36} \quad L_s(\mathbf{r}, \mathbf{s}, t) = L_0 + L_1 = (4\pi)^{-1} \Phi(\mathbf{r}, t) + 3(4\pi)^{-1} \mathbf{j}(\mathbf{r}, t) \cdot \mathbf{s},$$

where $\mathbf{j}(\mathbf{r}, t) = \iint L(\mathbf{r}, \mathbf{s}, t) \mathbf{s} d\Omega$ is the net energy flux vector responsible for the small deviation from isotropy. This approximation is only applicable when the diffusely multiple scattered part of the radiance dominates over that collimated, *i.e.* when $(1-g)\mu_s \gg \mu_a$ and far

from the light source. More pronounced asymmetric light scattering is described on adding a Dirac-function to the two-term phase function, forming the δ -Eddington phase function in Eq. 4.9.

4.2.3 Probabilistic methods

Powerful methods of deducing the light distribution in tissue are those based on the stochastic nature of light. Probability distribution functions of the interaction processes are generally formed utilising the dynamic model of the physical system studied. Within tissue optics they are founded on the radiative transport equation and its probabilistically defined interaction parameters, *i.e.* μ_a , μ_s (the probability of a photon being absorbed/scattered per unit path length) and the g -factor determining the shape of the angular scattering probability function via the phase function.

A traditional and well-known probabilistic model for photon propagation is the *Monte Carlo* approach,⁴³⁻⁴⁷ where individual steps along the photon path is randomised utilising probability density functions for the step sizes, $p(s)$, as well as for the two deflection angles θ $[0, \pi]$ and ϕ $[0, 2\pi]$, *i.e.* $p(\theta)$ and $p(\phi)$ respectively. From the probabilistic definitions of the scattering and absorption coefficients, the probability density function for the step size has been derived, given by^{46,47}

$$\text{Eq. 4.37} \quad p(s) = (\mu_s + \mu_a) \exp[-(\mu_s + \mu_a)s].$$

This exponential distribution can be transformed to yield a randomised sampling of the step size based on a uniformly distributed random number ξ between $[0, 1]$ as follows:

$$\text{Eq. 4.38} \quad s = -\frac{\ln(\xi)}{(\mu_s + \mu_a)}.$$

The probability density function for θ should be selected to resemble the true angular distribution of the scattering. Thus, the density function of the phase function proposed by Henyey-Greenstein²¹ is often adopted, given by

$$\text{Eq. 4.39} \quad p(\cos\theta) = \frac{(1 - g^2)}{2(1 + g^2 - 2g \cos\theta)^{3/2}},$$

where g is the previously mentioned asymmetry factor. Randomised sampling of θ , or rather $\mu = \cos\theta$, utilising a uniformly distributed randomised number ξ between $[0, 1]$ is obtained by employing a transformation of the density function in Eq. 4.39 to^{46,47}

$$\begin{aligned} \text{Eq. 4.40} \quad \mu &= \frac{1}{2g} \left(1 + g^2 - \left(\frac{1 - g^2}{1 - g + 2g\xi} \right)^2 \right) & \text{for } g \neq 0 \\ \mu &= 2\xi - 1 & \text{for } g = 0. \end{aligned}$$

Finally, we assume that the azimuthal angle ϕ is uniformly distributed within $[0, 2\pi]$. This means that $p(\phi)$ is a constant and equals $1/2\pi$. Thus the azimuthal angle is sampled with the randomised number ξ utilising

$$\text{Eq. 4.41} \quad \phi = 2\pi\xi.$$

Furthermore, the absorption is stochastically taken into account at every interaction event during the photon propagation, by decrementing a photon weight, w , initially assigned a value equal to unity.

Each photon path is computationally formed by a number of consecutive repeated events: the step size is randomised according to Eq. 4.38 and the position vector of the photon, \mathbf{r} , is updated. A factor of $w \frac{\mu_a}{(\mu_s + \mu_a)}$ is subtracted from the photon weight and is accounted as absorption. Finally, new deflection angles θ and ϕ are

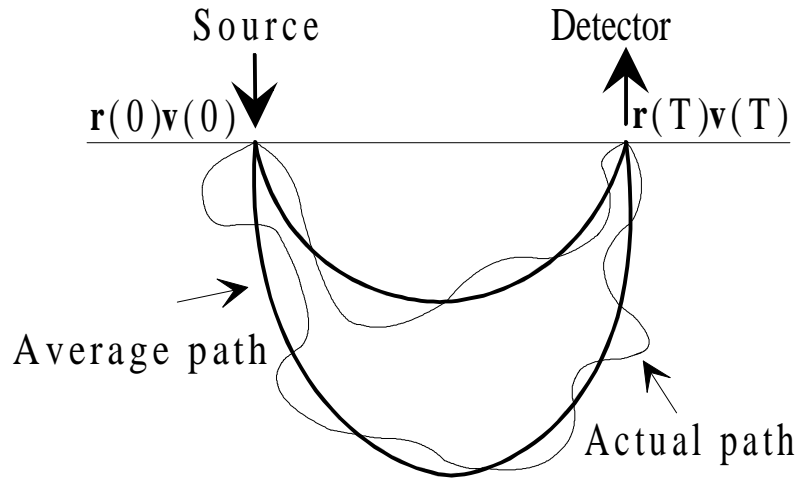


Figure 4.6 The concept of the probabilistic path integral method is shown.

randomised on the basis of Eq. 4.40 and Eq. 4.41, yielding the new propagation direction of the photon. Boundary effects, such as Fresnel reflection, is also taken into account. This is repeated until the position vector has reached one of the tissue boundaries and the photon weight is accounted as either transmission or reflection. The photon propagation can also end when the photon weight falls below a threshold value. Either a complete termination follows or, at one chance out of m ($m > 1$), the weight w is multiplied with the factor m , governed by a roulette technique. New photons are then subsequently launched, all with an initial weight set to unity. In order to obtain good statistics and high accuracy of the resulting absorption, reflection and transmission values, a large number of photons must be tracked.

The Monte Carlo method is easily adopted for extraction of further information. By recording the accumulated photon path length during the photon propagation and rescaling in temporal units using the speed of light, a time-resolved Monte Carlo method can be designed.⁴⁸⁻⁵¹ This means that the temporal behaviour of the reflectance and/or transmittance can be derived. A shift in the wavelength can also be incorporated at a certain fraction of the interaction events. This corresponds to a non-elastic scattering event, which enables Monte Carlo simulations of fluorescence light,^{52,53} as demonstrated in Paper VI, and of Doppler shifts.^{28,54-56}

Instead of randomising each individual step along the pathway of the photon, the entire average path can be stochastically treated. A path probability distribution function $P[\mathbf{r}(t)]$ in a non-absorbing medium is formed for the photon trajectories represented by $\mathbf{r}(t)$, each associated with the speed $\mathbf{v}=\mathbf{v}(t)\mathbf{s}$. This probabilistic approach is referred to as the *path integral* method.^{57,58} It differs from most of the other RT-methods (except for the adding-doubling method) in that it provides information on the radiance at local sites rather than in the entire tissue. The photon probability distribution function $\Psi(\mathbf{r}, \mathbf{v}, t)$ [$\text{m}^{-3} \text{sr}^{-1}$], and consequently expressions for radiometric quantities such as the radiance $L(\mathbf{r}, \mathbf{s}, t)$, is obtained by integrating the path probability distribution function along all the different average paths satisfying initial and final conditions of the location $\mathbf{r}(t)$ and velocity $\mathbf{v}(t)$ of the photon.^{57,58} The initial conditions are given by the location of the source and the initial speed of the photon ($\mathbf{r}(0)$ and $\mathbf{v}(0)$), whereas the final conditions at the time $t=T$ depend on the location of the detector and the final speed of the photon ($\mathbf{r}(T)$ and $\mathbf{v}(T)$), as shown in Figure 4.6. The absorption properties are then separately added by weighting the non-absorption probability distribution function for a photon with a factor dependent on the number of interactions within the tissue.

4.2.4 Discussion - radiative transport theory

Radiative transport theory provides us with a wide variety of computational tools to analyse light transport in tissue, well-founded on physical and biological measurements. However, this does not mean that we can pick any of these models for our application. The decision should be based on what type of information is required (*e.g.* the light distribution in the tissue, the amount of reflected light from or transmitted light through a tissue sample). The geometric and optical properties of the tissue being modelled and accuracy required must be balanced against acceptable computational time. These distinctions are already indicated by the different assumptions being made in the theoretical derivations above, but will be further elucidated with some examples of applications.

We can essentially distinguish between three categories of realistic light distributions, schematically illustrated in Figure 4.7, for which different radiative transport models are appropriate. The light intensity along a collimated light beam propagating in tissue with predominating absorption properties (Figure 4.7a), is well described by the simplest of the light propagation models - the Beer-Lambert law. The influence of scattered light can here be neglected, since most light-tissue interactions are light absorption events. An example of when Beer-Lambert's law is applicable, is given in the present work, Paper III, where the dynamic behaviour of the temperature dependence of the absorption coefficient of the highly light absorbing blood is derived at 586 nm, in conjunction with laser-induced thermotherapy. Blood is one of few tissues exhibiting predominating light absorption properties, appropriate for Beer-Lambert's law, in the visible region. However, tissue is also

highly light absorbing outside the visible window of the electromagnetic waves, *i.e.* Beer-Lambert's law is often applied in the infrared (IR) spectral range. For instance, it was used when performing light transmission measurements in the near infrared region on myocardial tissue in Paper VII, in order to find characteristic absorption dips. Beer-Lambert's law can also be

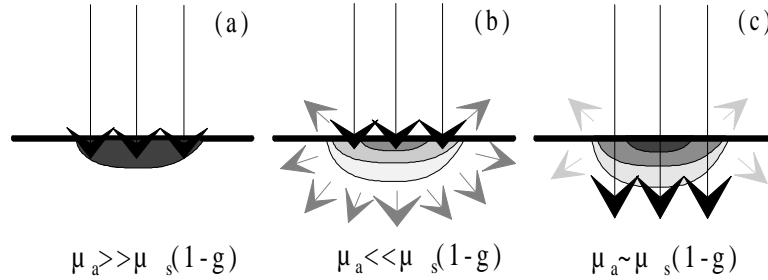


Figure 4.7 Three categories of light distributions, (a) dominating absorption properties, (b) dominating scattering properties, (c) similar absorption and scattering properties, are schematically illustrated. They are each well-described by different types of radiative transport models. The arrows represent the scattering characteristics and the contour plots the absorption characteristics.

employed to derive the total interaction coefficient, μ_t , from measurements of the collimated transmittance (see Eq. 4.24) of tissue with non-negligible scattering properties. This is often one step in the measurement procedure for determination of the three optical properties of a tissue sample, as shown in Papers I, II and IV. The forward directed scattered light must then be efficiently prevented from being registered by the detector, so that only the collimated transmitted part is monitored to ascertain the validity of Beer-Lambert's law.

The other extreme of possible light distributions is in cases where scattering events clearly dominate over absorption, *i.e.* when $\mu_s(1-g) \gg \mu_a$, as depicted in Figure 4.7b. A diffuse light flux is then almost immediately developed. Among the discretisation methods the light propagation can be described by the two diffuse light fluxes (the radiance integrated over the two hemispheres) propagating in the forward- and backward directions in the Kubelka-Munk model. Among the expansion methods the temporal and/or spatial light distribution can be derived employing the P_1 method (the diffusion approximation). Since most tissues exhibit highly forward-directed light scattering,¹⁸⁻²⁰ this category of models will not always provide accurate predictions of the fluence rate. They should thus be used with this limitation in mind. However, the light distribution can often be regarded as diffuse after numerous scattering events. From this it follows that these models will exhibit good accuracy far from the light source and tissue boundaries. Despite the restricted validity of the Kubelka-Munk model, it is frequently used for quick, gross estimations of the optical properties,⁵⁹⁻⁶¹ which yield adequate initial values for more extensive iterative computations.⁶² Since it provides analytical expressions for the absorption and scattering properties of a tissue sample versus easily measurable parameters such as reflectance and transmittance, in contrast to other light-propagation models. The more rigorous diffusion approximation is derived in three dimensions and provides temporal, spatial and angular information on the light distribution in- and outside the tissue. Reasonably good accuracy is obtained, provided no initial events of photon propagation are studied in time, or in space,⁶³ at low computation times. The diffusion approximation is therefore widely used for several

applications within tissue optics, particularly for comparison with time- or spatially-resolved transmission, or reflection measurements conducted in order to determine the optical properties,⁶⁴⁻⁶⁷ or to find inclusions with diverging optical properties, such as tumours embedded in normal dense tissue.⁶⁸⁻⁷¹ High values of the reduced scattering coefficient compared to the absorption coefficient are required for good accuracy. However, the diffusion approximation has been shown to be useful even when this assumption is not completely fulfilled, for example when optically monitoring oxygen saturation in blood. Good agreement between computed and measured results are obtained, as long as the wavelength of the probing light is longer than 660 nm, to reduce the high absorption coefficient.^{41,72} Even better accuracy can be achieved, if anisotropic scattering is incorporated in the two-flux model or diffusion approximation, by the use of correction factors or selecting appropriate expansions of the phase function^{23,24,26,34,73,74} (see *e.g.* the delta-Eddington method). The accuracy for the discretisation methods can be improved by discretisation of the radiance in more than two directions, as for example in seven¹⁹ or twenty-four³⁴ flux models. Comparison between the Beer-Lambert law, the Kubelka-Munk method, the diffusion approximation and the seven/twenty-four -flux model^{19,33,34} illustrates that all methods yield similar values of the fluence rates deep within the tissue. However, too low values for both the Beer-Lambert law (neglecting the diffusely scattered light) and the diffusion approximation, as well as, too high values for the Kubelka-Munk model (assuming completely diffuse light scattering), are computed immediately below the surface, compared to the results from the more accurate multi-flux models.

The final category of light distributions is that generated in tissue which is neither predominantly scattering nor absorbing, but rather a combination of the two (Figure 4.7c). This means that our method should not be restricted by validity when considering the optical properties of the tissue being modelled. The adding-doubling method has in this respect no limitations,^{35,39} and produces steady-state reflectance and transmittance data of good accuracy at low computation times. However, it supports layered tissue geometry of infinite lateral extension only, and the internal light flux is obtained with difficulty. Adding-doubling computations are therefore mainly performed in conjunction with transmission and reflection measurements of thin tissue samples, in order to iteratively fit measured to computed values by varying the optical properties of the modelled tissue sample.⁷⁵⁻⁸¹ In the present thesis (Paper IV) such computations were performed, in order to determine heat-induced changes in the optical properties of blood in a thin flow cell. When the light transport through thicker tissue samples is considered, the path integral method^{57,58} might be more appropriate. It is an efficient probabilistic method to model the light propagation in the frequently employed point-illumination and detection configuration, without restrictions on the validity concerning optical properties. The computations are here founded on the probability function of entire photon paths instead of individual photon steps. This approach seems particularly appropriate for applications where large computations of light distributions are required, *e.g.* for optical imaging. Finally, when the spatial light distribution is of interest, rather than point monitored data, or when complex tissue geometries are considered, a flexible method is required. The probabilistic method based on the Monte Carlo concept is the alternative within radiative transport theory that has the least restrictions concerning optical properties, illumination and detection geometries etc.. The results from such simulations are obtained with good accuracy, except for a normalisation factor, when comparing with experimental measurements performed in spatial,⁸ as well as temporal modes.^{82,83} The influence of geometrical parameters, such as the profile and size of a finite probe beam, on the light distribution has been simulated,^{46,84} as well as of complex

objects embedded in the tissue, such as cylindrical and curved blood vessels in dermis in the skin.⁸⁵⁻⁸⁷ The high accuracy achieved using the Monte Carlo approach means that this is the reference method frequently used to evaluate the validity of other less precise models. Predictions of the radiance using, for instance, the diffusion approximation have been related to those obtained from standard Monte Carlo simulations, these reveal reasonably good correspondence in the spatial light distribution (average deviations < 10%) for g-factors less than 0.8 and reduced scattering coefficients greater than 3 mm⁻¹, as long as the latter is at least ten times larger than the absorption coefficient.^{88,89} Beyond these limits, the diffusion approximation must be regarded as less accurate. Monte Carlo computations also confirm the results obtained from the previously mentioned multi-flux models,^{19,33,34} in these comparisons the diffusion approximation yielded lower fluence rates close to the surface and higher values at greater depths.

The high accuracy provided by Monte Carlo simulations is, in this work, shown to advantage in Paper I and Paper II, when expressing measured changes in transmittance and reflectance of liver and muscle tissue, in terms of changes in their optical properties in conjunction with laser-based treatments. However, there is one major drawback of the Monte Carlo method, the high accuracy can only be obtained after long computation times. Condensed Monte Carlo methods⁹⁰ (see Paper VI), hybrid methods (the Monte Carlo procedure combined with the diffusion approximation),^{91,92} and fitting procedures based on tabulated Monte Carlo simulated data have thus been developed^{82,83,93} (see Paper I and Paper II).

Basic knowledge of the optical properties of the tissue studied is thus an advantage, when selecting computation methods for analysis of the light distribution. However, the choice is also dependent on whether or not extensive results are required. One can say that simple models, such as those founded on one-dimensional transport theory, can successfully be employed for fast, approximate estimations of general trends, as performed in Paper III. A large number of quick computations were conducted here in order to conclude that an increase in the absorption coefficient always (in a large range of scattering and absorption properties) results in an decrease in both reflectance and transmittance, whereas an increase in the scattering coefficient always yields an increase in the reflectance and a decrease in the transmittance. If instead detailed information of for instance the spatial distribution of the light flux in a tissue sample of complex geometry is required with high accuracy, more rigorous and time-consuming computations must be conducted, as for example Monte Carlo simulations.

4.3 Electromagnetic theory

Let us now describe the light as electromagnetic waves. Propagation of electromagnetic waves through a spatially varying dielectric medium, such as tissue, is classically described by Maxwell's equations:^{94,95}

$$\text{Eq. 4.42} \quad \nabla \times \mathbf{H} = \frac{\partial \mathbf{D}}{\partial t} + \mathbf{J}$$

$$\text{Eq. 4.43} \quad \nabla \times \mathbf{E} = - \frac{\partial \mathbf{B}}{\partial t}$$

$$\text{Eq. 4.44} \quad \nabla \cdot \mathbf{D} = \rho$$

$$\text{Eq. 4.45} \quad \nabla \cdot \mathbf{B} = 0,$$

where \mathbf{H} [A m^{-1}] and \mathbf{E} [V m^{-1}] are the magnetic and electric field vectors, \mathbf{D} [C m^{-2}] is the electric displacement vector, \mathbf{B} [Wb m^{-2}] is the magnetic flux density vector, \mathbf{J} [A m^{-2}] is the current density vector, and ρ [C m^{-3}] is the volume charge density. Maxwell's equations are condensed mathematical expressions for fundamental physical laws describing, in integral

form, the total current $(\frac{\partial \mathbf{D}}{\partial t} + \mathbf{J}) \cdot \partial \mathbf{a}$ passing through the area represented by $\partial \mathbf{a}$ induces

a magnetic field, which equals the line integral of \mathbf{H} along the path surrounding the area (Ampère's law). Analogously, a time-varying magnetic flux density \mathbf{B} passing through a closed conducting loop generates a current around that loop, inducing an electric field \mathbf{E} (Faraday's law). Furthermore, the total electric flux $\mathbf{D} \cdot \partial \mathbf{a}$ flowing out of a closed surface $\partial \mathbf{a}$, equals the total charge $\rho \partial V$ (∂V is an infinitesimal volume element) enclosed by the surface (the Gauss electric law). This is in contrast to the magnetic flux $\mathbf{B} \cdot \partial \mathbf{a}$, where there is no magnetic "charge" and thus no *net* flux flowing in or out of a closed surface as indicated by Eq. 4.45 (the Gauss magnetic law). Furthermore, the constitutive relations in a non-dispersive and isotropic medium (corresponds, in the optics region, to an assumption of a refractive index independent of the wavelength and direction, respectively), expressing how the field vectors are interrelated and dependant on the characteristics of the medium, are given by

$$\text{Eq. 4.46} \quad \mathbf{D} = \epsilon \mathbf{E}$$

$$\text{Eq. 4.47} \quad \mathbf{B} = \mu \mathbf{H}$$

$$\text{Eq. 4.48} \quad \mathbf{J} = \sigma \mathbf{E},$$

where ϵ [F m^{-1}] is the permittivity, μ [H m^{-1}] is the permeability (both assumed to be time independent) and σ [S m^{-1}] is the conductivity. Hence, Maxwell's equations Eq. 4.42-Eq. 4.45 can be rewritten as

$$\text{Eq. 4.49} \quad \nabla \times \mathbf{H} = \epsilon \frac{\partial \mathbf{E}}{\partial t} + \sigma \mathbf{E}$$

$$\text{Eq. 4.50} \quad \nabla \times \mathbf{E} = -\mu \frac{\partial \mathbf{H}}{\partial t}$$

$$\text{Eq. 4.51} \quad \nabla \cdot \mathbf{E} = \frac{\rho}{\epsilon}$$

$$\text{Eq. 4.52} \quad \nabla \cdot \mathbf{H} = 0.$$

Eq. 4.51 and Eq. 4.52 are derived under the assumption of a homogeneous medium. An effective complex permittivity is derived from the time-harmonic version of Eq. 4.49 with the convention $e^{-i\omega t}$ ($\omega=2\pi \cdot \text{frequency}$):

$$\text{Eq. 4.53} \quad \nabla \times \mathbf{H} = -i\omega\epsilon\mathbf{E} + \sigma\mathbf{E}$$

as

$$\text{Eq. 4.54} \quad \epsilon_{\text{eff}} = \epsilon + i \frac{\sigma}{\omega}.$$

Its correspondence within optics is the refractive index given by⁹⁵

$$\text{Eq. 4.55} \quad n=n'+in''=(\epsilon/\epsilon_0)^{1/2},$$

where ϵ_0 is the permittivity for free space.

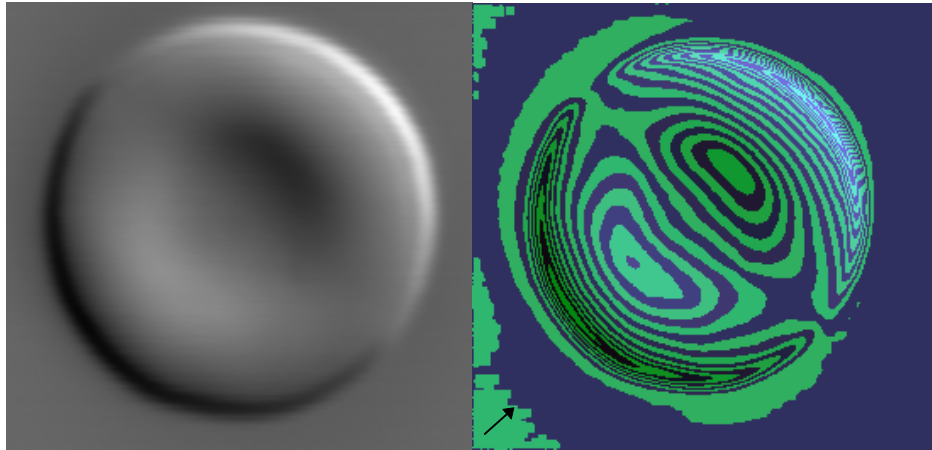


Figure 4.8 An image of a red blood cell (the author's), obtained in a phase microscope, is shown to the left. The processed image to the right schematically illustrates the interference pattern recorded when the two probe beams (with a small inter-distal separation) of the phase microscope were scanned over the cell in the diagonal direction. The direction of the scanning is indicated by the arrow in the left lower corner. A spatial distribution of the phase shift can thus be derived, which in turn corresponds to a map of the refractive index and the thickness of the cell.

The electromagnetic theory is founded on this set of equations, we want to solve them for tissue in the optical region of electromagnetic spectrum.

4.3.1 Tissue as a random continuum

Our aim is to find a solution to Eq. 4.49-Eq. 4.52 for tissue. Tissue with its organelles, cell membranes, inter-cellular structures etc. cannot be regarded as a homogeneous medium, but

instead as a random continuum. Thus, there is a spatial dependency in the permittivity, $\epsilon_{\text{eff}} = \epsilon_{\text{eff}}(\mathbf{r})$, which must be known in order to solve Maxwell's equations. In atmospheric optics this problem has been approached by separating the permittivity into two components; one average value $\langle \epsilon_{\text{eff}}(\mathbf{r}) \rangle$ and one randomly fluctuating component $\epsilon_{\text{eff}}'(\mathbf{r})$.⁴ The latter has different functional forms depending on the nature of the true physical fluctuations in the atmosphere (rain, fog, smog, cloud etc.). For tissue this would according to Eq. 4.55 be equivalent to determining the refractive index as a continuous function of position, dependent on the microscopic morphology of the tissue: on the quantity, size, shape of organelles, cells, structural tissue etc.. Considering these are often of sub-micron size, it is not surprising that this concept has not been realised within tissue optics. However, a first step has been taken in studying spatial variations of the refractive index of cells and mitochondria in a phase microscope.⁹⁶ This is for a red blood cell (the author's) exemplified in Figure 4.8.

4.3.2 Tissue as a collection of particles

Instead of applying the random continuum approach, the electromagnetic theory within tissue optics has been applied to clusters of biomolecules and cells by finding solutions to Maxwell's equations for homogeneous particles. From the assumption of homogeneity it follows that ϵ_{eff} and μ are constants. Thus, Eq. 4.49 and Eq. 4.50 can be manipulated together to form the general vector wave or Helmholtz equations:⁹⁵

$$\text{Eq. 4.56} \quad \nabla \times (\nabla \times \mathbf{E}) - k^2 \mathbf{E} = 0$$

$$\text{Eq. 4.57} \quad \nabla \times (\nabla \times \mathbf{H}) - k^2 \mathbf{H} = 0,$$

where $k^2 = \omega^2 \epsilon_{\text{eff}} \mu = (2\pi/\lambda)^2$. There are several physically realisable electromagnetic fields (\mathbf{E} , \mathbf{H}) that satisfy these equations. In order to find the solution of interest, geometrical and material parameters for the specific problem must be formulated by, for instance, boundary conditions. We are interested here in the electromagnetic fields inside a particle, *i.e.* the internal field \mathbf{E}_{int} , and the scattered E-field \mathbf{E}_s outside the particle. The latter can be regarded as a superposition of wavelets originating from dipoles in the particle, in turn induced by the incident field \mathbf{E}_i . Our fundamental conditions can then be expressed as follows: both the internal (\mathbf{E}_{int}) and external ($\mathbf{E}_{\text{ext}} = \mathbf{E}_i + \mathbf{E}_s$) fields should satisfy Eq. 4.56. Moreover, the internal and external E-fields should be related via boundary conditions at the edge of the particle which depends on the object being studied. The boundary conditions are often based on the general properties of electromagnetic waves, stating for instance the tangential components of the \mathbf{E} - and \mathbf{H} -fields are continuous when passing across a boundary. The incident field is conveniently assumed to be a plane wave $\mathbf{E}_i(\mathbf{r}) = \mathbf{E}_0 \exp(i \mathbf{k}_{\text{sm}} \cdot \mathbf{r} - i\omega t)$, propagating in the surrounding medium with the wave vector \mathbf{k}_{sm} .

The general idea of solving Eq. 4.56 is to expand the incident, internal, as well as scattered fields in terms of vector waves, \mathbf{M} and \mathbf{N} , and determine the expansion coefficients from the boundary conditions for each particle. This can be performed since these vector functions

satisfy the vector wave equation. Spherical vector waves are frequently employed and defined as:⁹⁷

$$\text{Eq. 4.58} \quad \mathbf{M}_{mn}^o(\mathbf{kr}) = \nabla \times \mathbf{r} e^{-im\phi} P_n^m(\cos\theta) (j_n(kr) + in_n(kr))$$

$$\text{Eq. 4.59} \quad \mathbf{N}_{mn}^o(\mathbf{kr}) = k^{-1} \nabla \times \mathbf{M}_{mn}^o(\mathbf{kr}),$$

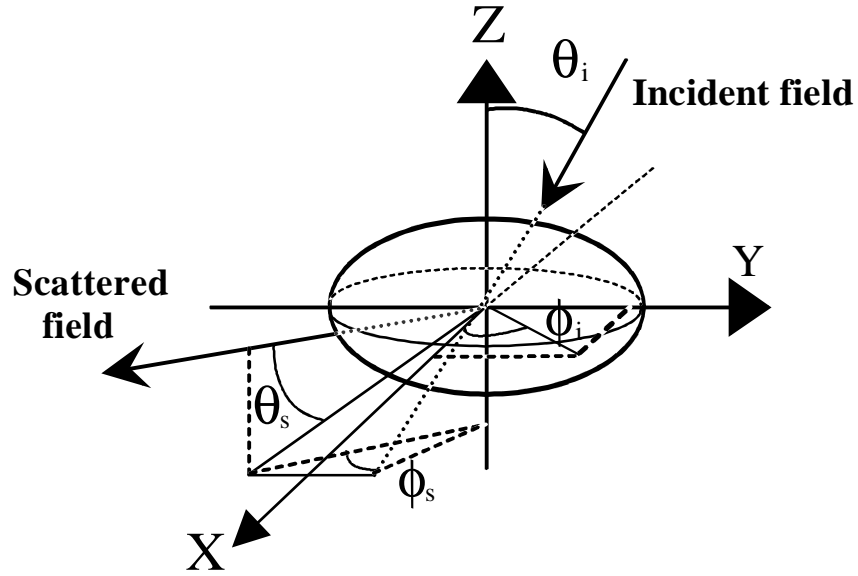


Figure 4.9 Geometrical parameters, used for the derivation of the general solution to the vector wave equation for a single particle are shown.

where geometrical parameters are depicted in Figure 4.9. $P_n^m(\cos\theta)$ are associated Legendre functions specified by their indices $n=0, 1, 2, \dots$ and $m=-n, -n+1, \dots, n-1, n$ (first orders are exemplified in Eq. 4.6). $j_n(kr)$ are spherical Bessel functions, $n_n(kr)$ are Neumann functions and k equals $2\pi/\lambda_{\text{medium}}$.

The \mathbf{M}^o - and \mathbf{N}^o -functions are outward travelling waves with singularities at the origin. The incident field is therefore expressed in terms of \mathbf{M}^i - and \mathbf{N}^i -functions, *i.e.* spherical vector functions as defined in Eq. 4.58 and Eq. 4.59, but with a pure Bessel radial dependency (not Neumann functions due to their behaviour at the origin) in order to obtain a regular solution without singularities at $r=0$ at the centre of the particle:

$$\text{Eq. 4.60} \quad \mathbf{E}_i(\mathbf{k}_{\text{sm}} \mathbf{r}) = E_0 \sum_{m, n} D_{mn} [a_{mn} \mathbf{M}_{mn}^i(\mathbf{k}_{\text{sm}} \mathbf{r}) + b_{mn} \mathbf{N}_{mn}^i(\mathbf{k}_{\text{sm}} \mathbf{r})].$$

D_{mn} are normalisation constants, and the expansion coefficients a_{mn} and b_{mn} are given by the incident field. The internal field is also an equivalent expansion of the \mathbf{M}^i - and \mathbf{N}^i -functions, due to the requirement of a final solution at the origin:

$$\text{Eq. 4.61 } \mathbf{E}_{\text{int}}(\mathbf{k}_{\text{particle}} \mathbf{r}) = E_0 \sum_{m', n'} D_{m'n'} [c_{m'n'} \mathbf{M}_{m'n'}^i(\mathbf{k}_{\text{particle}} \mathbf{r}) + d_{m'n'} \mathbf{N}_{m'n'}^i(\mathbf{k}_{\text{particle}} \mathbf{r})]$$

with the unknown expansion coefficients $c_{m'n'}$ and $d_{m'n'}$. Finally, the scattered field is expressed as a summation of outward travelling, complete \mathbf{M}^o - and \mathbf{N}^o -functions, including the Neumann functions, due to their asymptotic behaviour at large distances from the particle:

$$\text{Eq. 4.62 } \mathbf{E}_s(\mathbf{k}_{\text{sm}} \mathbf{r}) = E_0 \sum_{m, n} D_{mn} [f_{mn} \mathbf{M}_{mn}^o(\mathbf{k}_{\text{sm}} \mathbf{r}) + g_{mn} \mathbf{N}_{mn}^o(\mathbf{k}_{\text{sm}} \mathbf{r})]$$

with f_{mn} and g_{mn} as unknown expansion coefficients. Formally, this concept provides an exact solution to the vector wave equation, but as the expansion series must be numerically truncated, it has an approximate character.

The problem has now been reduced to a determination of the expansion coefficients $c_{m'n'}$, $d_{m'n'}$ (internal field), f_{mn} and g_{mn} (scattered field) from the known a_{mn} and b_{mn} coefficients of the incident field and from the specific boundary conditions. Let us start with the simplest type of particle, a homogeneous sphere.

The special case of the generally formulated solution to the vector wave equation for a homogeneous sphere is well-known under the name *Lorentz-Mie theory* or just *Mie theory*.^{94,95,98} An incident linearly polarised, plane wave with the amplitude E_0 results in expansion series (Eq. 4.60) where all expansion coefficients $m \neq 1$ vanish. The expansion series can then be written as:⁹⁴

$$\text{Eq. 4.63 } \mathbf{E}_i(k_{\text{sm}} \mathbf{r}) = E_0 \sum_n i^n \frac{(2n+1)}{n(n+1)} (\mathbf{M}_n^i - i \mathbf{N}_n^i) \quad (m=1)$$

for the incident E-field, with a corresponding H-field. Thus, compared with Eq. 4.60 the coefficients a_{mn} and b_{mn} are known and we proceed with the boundary conditions using the continuity of the tangential components of the fields across a boundary. Mathematically, this is expressed by

$$\text{Eq. 4.64 } (\mathbf{E}_i + \mathbf{E}_s - \mathbf{E}_{\text{int}}) \times \mathbf{e}_r = 0 \text{ at } \mathbf{r} = a \mathbf{e}_r$$

$$\text{Eq. 4.65 } (\mathbf{H}_i + \mathbf{H}_s - \mathbf{H}_{\text{int}}) \times \mathbf{e}_r = 0 \text{ at } \mathbf{r} = a \mathbf{e}_r$$

at the boundary, $\mathbf{r} = a \mathbf{e}_r$, where a is the radius of the sphere and \mathbf{e}_r is the radial unit vector of the spherical coordinate system with the origin at the centre of the sphere. We have four unknowns c_n , d_n (internal field), f_n and g_n (scattered field) and four independent equations originating from Eq. 4.64 and Eq. 4.65:

Eq. 4.66

$$E_{i\theta} + E_{s\theta} = E_{int\theta}$$

$$E_{i\phi} + E_{s\phi} = E_{int\phi}$$

$$H_{i\theta} + H_{s\theta} = H_{int\theta}$$

$$H_{i\phi} + H_{s\phi} = H_{int\phi} \quad \text{at } \mathbf{r} = a\mathbf{e}_r$$

Hence, the four coefficients are uniquely determined. The expressions consist of the spherical Bessel and Neumann functions, $j_n(x)$ and $n_n(x)$, and their derivatives with x and mx as arguments, where x is the size parameter equal to $2\pi n'_{sm}a/\lambda$ (n'_{sm} is the real part of the refractive index of the surrounding medium and λ is the wavelength of the electromagnetic wave) and m is the relative refractive index equal to $n_{particle}/n_{sm}$.^{94,98} The internal and scattered fields can thus be computed.^{94,99}

As soon as the shape of the particle diverges from the sphere, the complexity of the derivations of the solutions to the vector wave equation increases. The boundary conditions, together with the expansion series, rarely form a linear set of equations, as observed for a sphere, which is necessary to easily compute the expansion coefficients. This however can be solved by mathematically reformulating either the expansion functions or the boundary conditions. The former concept is equivalent to separating the vector wave equation in a more appropriate coordinate system, where one of the coordinate surfaces coincides with the surface of the non-spherical particle. For instance, *cylindrical coordinates* and vector functions are employed to solve the vector wave equation for circular cylinders.^{94,95,98} Moreover, *spheroidal coordinates* have successfully been used for arbitrary spheroids, oblate or prolate.^{100,101}

The second concept implies that new boundary conditions are formulated, whereas the fields are still expanded in spherical vector functions, as in Eq. 4.60 - Eq. 4.62. Waterman,¹⁰² as well as Barber and Yeh,⁹⁷ expressed a boundary condition by means of integrals over the particle surface S of electric and magnetic surface currents. This in combination with the so-called extinction theorem⁹⁵ forms an *extended boundary condition* used to derive the expansion coefficients for the spherical vector functions. The extinction theorem states that the scattered field must cancel the incident field inside the particle and the expression for the total E-field can accordingly be written as

$$\left. \begin{array}{l} \mathbf{r} \text{ outside particle} \\ \mathbf{r} \text{ inside particle} \end{array} \right\} \mathbf{E}(\mathbf{r}) \Big|_0 = \mathbf{E}_i(\mathbf{r}) + \mathbf{E}_s(\mathbf{r}) = \mathbf{E}_i(\mathbf{r}) +$$

Eq. 4.67

$$+ \nabla \times \int_S \mathbf{E} \text{ surface currents } \partial S + \nabla \times \nabla \times \int_S \mathbf{H} \text{ surface currents } \partial S$$

Hence, inside the particle the fields originating from the surface integrals should cancel the incident field. This relates the expansion coefficients of the incident field to the surface currents. The surface currents generate in turn an outward propagating field, *i.e.* the scattered field $\mathbf{E}_s(\mathbf{r})$. This relates the expansion coefficients of the scattered field to the

surface currents. Consequently, the connection between the expansion coefficients of the incident and scattered fields lies in the surface currents. This is mathematically handled by a transition matrix or the T-matrix:

$$\text{Eq. 4.68} \quad \begin{bmatrix} f_{mn} \\ g_{mn} \end{bmatrix} = - \left[\text{T - matrix} \right] \begin{bmatrix} a_{mn} \\ b_{mn} \end{bmatrix}$$

This extended boundary method is therefore frequently called the *T-matrix method*. It implies that the scattering problem is reduced to the determination of the elements of the T-matrix, consisting of surface integrals. These computations can be performed for arbitrarily shaped particles, but have mainly been applied to spheroidal particles.¹⁰³⁻¹⁰⁵ When being derived for spherical particles, the T-matrix is diagonal with elements that coincide with the expressions for the expansion coefficients obtained by Lorentz-Mie theory.

If all terms are included in the expansion series, though this is computationally unrealistic, all the methods based on electromagnetic theory discussed so far can be regarded as exact solutions to the vector wave equation. They are often associated with extensive computations, except for the spherical particle, thus the requirement for approximate, less computationally demanding methods.

For particles small compared to the wavelength, *i.e.* if $|m|x \ll 1$ (x is the size parameter, m is the relative refractive index), it can be shown⁹⁴ that expansion coefficients with terms of the order higher than x^3 can be rejected without any serious concern of the accuracy. For the Mie expansion series of the scattered field this means that only f_{11} must be retained:

$$\begin{aligned} \text{Eq. 4.69} \quad f_{11} &= -i \frac{2x^3}{3} \frac{(m^2 - 1)}{(m^2 + 2)} + O(x^5) \\ g_{11} &= O(x^5) \\ f_{12} &= O(x^5) \\ g_{12} &= O(x^7) \end{aligned}$$

This approximation corresponds to the well-known Rayleigh scattering phenomenon.^{95,98} It can then be shown that the scattered intensity I_s is proportional to the square of the amplitude of the field $|\mathbf{E}_s|$ divided by k (the wave number):⁹⁸

$$\text{Eq. 4.70} \quad I_s \sim (|\mathbf{E}_s|/k)^2 \sim (|f_{11}|/k)^2 \sim x^6/k^2 \sim \lambda^2/\lambda^6 = \lambda^{-4}$$

From this it follows that the intensity is inversely proportional to the fourth power of the wavelength. This well-known proportionality of Rayleigh scattering is in general true regardless of particle shape, as long as, the object is small compared to the wavelength. Furthermore, it can be proven⁹⁴ that the physical interpretation of Rayleigh scattering is that it originates from a particle so small that the surrounding field can be regarded as a uniform

static electric field. This means that also the field inside the particle can be considered as uniform.

To incorporate shape effects, *i.e.* to derive approximate expressions for the light scattering by particles of irregular geometric shape, the Rayleigh-Gans-Debye theory^{95,98} is often used. It can be derived by estimating the scattered E-field per infinitesimal volume unit based on the small particle/Rayleigh limit of Mie theory, as described above. This "E-field density" is then integrated over the true particle volume. The validity of this approximation is satisfactory when $|m-1| \ll 1$ and $kd|m-1| \ll 1$, where d is a linear characteristic dimension of the particle. That is when the refractive indices inside and outside of small or intermediate sized particles (compared to the wavelength) are close.

Numerical techniques can also be applied to compute approximately the scattered E-fields. Local rather than global information on the E-field is often obtained. Instead of solving the eigenvalue problem given by the vector wave equation, by expanding the E-fields in vector functions, simpler expansion functions can be chosen employing the method of moments (MoM).⁹⁵ Maxwell's equations can also be numerically solved by discretising them in space and time, forming so-called finite-difference equations. Employing the finite-difference time-domain method (FDTD),⁹⁵ the E-fields are then obtained using a numerical time-stepping technique. Furthermore, a numerical technique, well-known within other disciplines, is the finite-element method. The E-fields are here determined at certain positions, or nodes and the global expressions for the fields are written as a sum of these node-values multiplied by a basis- or shape function. The shape function is unity at the node and decreases linearly to zero on approaching the neighbouring nodes, *i.e.* a pyramid function. The E-fields are thus determined locally as though raising a tent.

4.3.3 Discussion - electromagnetic theory

Electromagnetic theory, both its fundamental nature and general character are appealing to many physicists, since it is founded on the basic laws of physics and provides mathematical tools, which can be used for a large number of applications. Principally, it forms a framework that can lead to an exact solution to the problem of light distribution in a random continuum such as tissue, if only an expression for the spatial dependency of the refractive index is known in detail. A tissue sample with its cell membranes, cell plasma, organelles and structural components must thus be mapped in terms of the refractive index. The spatial variations in the refractive index of individual cell membranes and mitochondria have been determined,⁹⁶ but the major part of this immense task remains. Instead, the relevance of electromagnetic theory within tissue optics lies mainly in the possibility of studying the influence of characteristic morphological features of the individual tissue components on the light distribution. Which of the tissue constituents can the major part of the light scattering be attributed to, what affect does the cell size, shape and alignment as well as the relative refractive index have on the light distribution, these are some of the questions that should be answered. This is further exemplified in Chapter 7.2. However, some applications of electromagnetic theory will be discussed briefly here.

The most widespread method based on electromagnetic theory within tissue optics is Lorentz-Mie computations for spheres. These are mainly performed in order to compute the scattering properties of calibration suspensions of latex spheres,^{15,106,107} as described in this work (Paper I and Paper II), and also of tissue phantoms, such as Intralipid^{14,16} and spheres dissolved or embedded in suitable media,^{10,12,13} rather than computing the scattering properties of tissue. The reason is that independently-scattering, homogeneous spheres can hardly be considered as a useful theoretical model for cells in tissue, although blood cells in diluted blood is one of the few exceptions. Steinke and Shepard⁹ found good correlation between Mie computed and experimentally determined scattering properties of randomly oriented blood cells. Interesting theoretical information has been extracted on, for instance, the influence of cell size on the light scattering by blood cells from results of Mie computations.^{9,108,109} Even the cell membrane has been incorporated in Mie computations for a layered sphere.^{110,111} Yet, no major influence of the membrane on the distribution of the scattered light was predicted. Mie theory has not so far been extended to the description of complex multiple light scattering by a collection of cells, as in general tissue. Diluted blood, where the cells are well-separated, is from the viewpoint of tissue optics an unusual and simple example. While Mie computations must be recognised as an inadequate model for prediction of authentic light distributions in conventional tissue, it can provide highly interesting information on the size of the average scatterer in tissue,^{14,112,113} by for instance relating the measured to computed wavelength dependence of the scattering properties. A theoretical wavelength dependence is analytically formulated in Paper II by two simple polynomials and used to determine the so called Mie equivalent average radius of liver tissue. This concept is developed in Paper II and was partly based on the work of Mourant *et al.*¹⁴

The solution of the vector wave equation separated in cylindrical coordinates would be an interesting theoretical analogue for muscle fibres, nerve cells and other structural formations in tissue. For instance, the diameter of collagen fibres in neonatal skin has been obtained by comparing experimental data with computations based on such a cylindrical model.⁷⁹ Moreover, the Rayleigh-Gans-Debye approximation has been utilised for light scattering computations of cylinders representing the similar structures of retinal nerve fibres.¹¹⁴

Light scattering from other non-spherical particles, mainly spheroidal objects smaller or equivalent to the wavelength, as in other fields been computed utilising the T-matrix method.^{103-105,115} The application to larger scattering objects such as biological cells, has for computational reasons been beyond reach until fairly recently¹¹⁶. The suggested solution was implemented in the present work and the T-matrix method has been utilised in Paper V for computations of the light scattering by red blood cell volume equivalent spheroids. This non-sphere model enables studies of the influence of cell alignment and shape changes, impossible with Mie theory computations.

The approximate Rayleigh scattering model and its well-known wavelength dependence ($I_s \sim \lambda^{-4}$), can within tissue optics be applied to study the influence of scattering by smaller particles, for example denatured proteins,⁷⁵ or as a "small-scatterer indicator" when estimating the average size of the scatterers in tissue^{14,79} (see Paper II). It can also provide the method of estimating the concentration of important biomolecules based on the information provided by light scattering.¹¹⁷

4.4 Relationship between the radiative transport and electromagnetic theories

Traditionally, computation methods based on radiative transport theory have almost exclusively been used to predict light transport in tissue. It treats the tissue, as a homogeneous medium with averaged light absorption and scattering properties. This is necessary in order to derive methods applicable to authentic clinical conditions and confirmed by experimental results.⁶⁻⁸ However, there are still some open questions regarding for instance the choice of the phase function, the influence of structured cell formations and tissues on the light distribution, and which of the tissue constituents represent the chief scatterers. A growing interest for the relationship between microscopical, morphological and physiological properties of tissue and its optical properties can be seen in recent years,^{14,79,96,112,113,118-121} and is also reflected by the work presented here (Paper I to Paper V). Thus, the detailed information, concerning for example shape, size, alignment and refractive index of a scattering particle provided by electromagnetic theory, has reinforced the position of EM-theory within tissue optics. In addition, the input parameters to the radiative transport computations are often optical properties obtained from inverse or iterative computations based on the very same theory. It is therefore essential, in addition to experimental results, to have theoretical reference techniques in order to confirm the reasonableness of computed results obtained from transport theory. Electromagnetic theory may here serve an important role. In the light of all this, it is important to identify the links between the two theories, which will be discussed here.

To enable the correlation between the radiometric, measurable quantities provided by transport theory and the field characteristics given by electromagnetic theory, Fante¹²² and Ishimaru⁴ have proved that the radiative transport equation can be regarded as an approximate reformulation of Maxwell's equations for a random continuum under certain premises. One of these is that the fluctuations in the permittivity $\epsilon_{\text{eff}}'(\mathbf{r})$ ($\epsilon_{\text{eff}}(\mathbf{r}) = \langle \epsilon_{\text{eff}}(\mathbf{r}) \rangle + \epsilon_{\text{eff}}'(\mathbf{r})$) should be small. The radiance \mathbf{L} in the radiative transport theory is then equivalent to the statistical average of the time-varying Poynting vector \mathbf{S} (see definition in Eq. 4.72) used in electromagnetic theory.

Further links between the two theories can be recognised in the relationship of the three optical properties used in radiative transport (RT) theory to parameters derived from the single-particle analysis of Maxwell's equations. For instance, the phase function, closely related to the g-factor, is in the transport theory generally formulated as an expansion series in terms of Legendre polynomials (see Eq. 4.4). The choice of expansion terms is by no means arbitrary, but can be seen as being influenced by electromagnetic theory. This is so, since the phase function in RT-theory corresponds to the angular distribution function in electromagnetic theory. From Eq. 4.58 - Eq. 4.62 we know that the angular distribution, originating from a single scattering object, is in EM-theory preferably expressed in spherical wave vectors composed of Legendre polynomials.

The absorption and scattering coefficients of radiative transport theory can also be heuristically related to single-particle parameters derived from the analysis of Maxwell's equations. These single-particle parameters are often expressed in terms of differential scattering and total absorption cross sections. The former is defined as⁹⁵

$$\text{Eq. 4.71} \quad \sigma_d(\mathbf{s}, \mathbf{s}') = \lim_{r \rightarrow \infty} \frac{\mathbf{r}^2 S_{s'}}{S_s}$$

where \mathbf{s} and \mathbf{s}' are the unit vectors pointing in the direction of the incident and scattered waves. Moreover, S_s and $S_{s'}$ are the magnitudes of the incident and scattered power flux density vectors, also called the Poynting vectors:⁹⁵

$$\text{Eq. 4.72} \quad \mathbf{S}_s = \frac{1}{2}(\mathbf{E}_i \times \mathbf{H}_i^*) = \frac{\sqrt{\epsilon_0}}{2\sqrt{\mu_0}} |\mathbf{E}_i|^2 \mathbf{s}$$

$$\text{Eq. 4.73} \quad \mathbf{S}_{s'} = \frac{1}{2}(\mathbf{E}_s \times \mathbf{H}_s^*) = \frac{\sqrt{\epsilon_0}}{2\sqrt{\mu_0}} |\mathbf{E}_s|^2 \mathbf{s}',$$

where \mathbf{H}_i^* and \mathbf{H}_s^* means the complex conjugate of the incident and scattered H-fields, respectively. The absorption cross section is defined as⁹⁵

$$\text{Eq. 4.74} \quad \sigma_a = \frac{- \int_{\text{Spherical area}} \text{Re}(\frac{1}{2} \mathbf{E} \times \mathbf{H}^*) \cdot \partial \mathbf{a}}{|\mathbf{S}_s|},$$

where $\mathbf{E} = \mathbf{E}_i + \mathbf{E}_s$ and $\mathbf{H} = \mathbf{H}_i + \mathbf{H}_s$ are the total fields. The integration is here performed over a spherical area surrounding the particle at large distances from the particle ($r \rightarrow \infty$). Assuming single scattering, the absorption and scattering coefficients, μ_a and μ_s , used in transport theory, are for a suspension of discrete scattering particles simply given by multiplying the cross sections with a factor proportional to the concentration of particles. Note that this is only true for low concentrations of scatterers. If the particles are not well separated, multiple or dependent light scattering cannot be neglected. This leads to complicated and at present unformulated relations between the microscopic scattering properties provided by electromagnetic theory (σ_d , σ_a , g_{single}) and the average scattering parameters used in radiative transport theory (μ_s , μ_a , g_{multiple}).

Each model, either founded on radiative transport theory or electromagnetic theory, has its individual strength for different applications, which is well illustrated by the work included in this thesis. For instance, the simple *Beer-Lambert law* was employed to describe the complex phenomena of changing absorption properties of blood during a short laser pulse and to derive a relationship between the absorption coefficient and the temperature of blood (Paper III). Thus, complicated events can be described approximately, by just applying a simple enough model. The price paid by utilising Beer-Lambert's law is that the scattering properties cannot fully be included in the modelling. However, this is not unreasonable for certain tissues, especially for blood, since its absorption coefficient at the 586 nm used in this experiment was shown to be the predominating optical parameter, compared to the

scattering properties. The *adding-doubling method*, based on a discretisation of the transport equation, was used to interrelate the transmitted and reflected light from a thin flow cell with the optical properties of blood, in order to monitor changes induced by slow heating (Paper IV). This was performed at a wavelength of 633 nm, at which the light absorption of blood cannot be considered to dominate over the light scattering. Thus, the scattering properties cannot be neglected, which excludes the use of a simple model such as that of Beer and Lambert. Besides, the forward directed nature of the light scattering by blood cells yields a g-factor close to unity, where several of the other models are invalid. A model without any restrictions in validity related to the optical properties is therefore needed. This is when the adding-double method may well be employed. Furthermore, we have a simple, layered measurement geometry and there are no advantages to know the two dimensional distribution of the transmittance or reflectance, which again favours the adding-doubling method. The *Monte Carlo* approach would be another option and was in this work applied in similar experiments, when determining changes in the optical properties of liver and muscle tissue in conjunction with photodynamic- and thermotherapy (Paper I and Paper II). In addition, this method is completely compatible with different tissue geometries and provides full three-dimensional information concerning the light distribution both within and outside the tissue. The disadvantage with this randomised approach is that the realisation of acceptable statistics is associated with long computation times, which, however, can be overcome by various methods. Yet, not even the Monte Carlo method supplies any detailed information on the physical scattering and absorption events. In order to model the influence of the morphology (size, shape, orientation etc.) of the biological cells on the distribution of light in and outside the tissue, one has to return to theory founded on the basic laws of Maxwell, for instance *Mie theory*, describing the propagation of light by taking the wave properties into consideration. The impact of heat on the sphering of the disc shaped red blood cells (Paper IV), can be theoretically investigated by applying a solution to the scattering problem based on a non-spherical scattering object, for example the *T-matrix* formalism (Paper V). The total light distribution from an assembly of cells, or even a tissue sample, is then often deduced by simply multiplying the light distribution from this single scattering event by a cell concentration related factor. This means that cooperative scattering effects as well as multiple scattering events are neglected. However, general trends of the influence of cell morphology on the scattering distribution can still be studied.

5. Computational methods

The theoretical expressions described in the previous chapter can be re-phrased into various computer routines in order to numerically derive solutions. There are probably almost as many implementations as users, except for a few standard public programs available. The computations performed in this work are mainly based on four such programs for two different types of applications. Inverse adding-doubling and Monte Carlo computations have essentially been performed in order to solve the inverse problem (see Papers I, II and IV), *i.e.* to determine the optical absorption and scattering properties of a tissue sample from measured light distribution values. This enables us to quantify the complex physical phenomena of light transport in tissue in terms of a few, simple parameters. The inverse adding-doubling program of Prahl *et al.*³⁹ and the code for Monte Carlo simulations written by Wang and Jacques⁴⁷ were used here. Furthermore, Mie theory and T-matrix computations have been employed to solve the direct problem in Papers I, II and V, *i.e.* to estimate the light distribution from known configuration and material parameters. The Mie theory was implemented from the work by Zijp and ten Bosch⁹⁹ and the T-matrix programs were based on the code developed by Barber and Hill.¹²³

5.1 Computations treating the indirect problem

The indirect problem is closely related to the determination of optical properties. Solving it is computationally a rather demanding task, since it often involves an iterative fitting procedure. Computed light transmission and reflection data are fitted to corresponding measured values by varying the input parameters of a light distribution model, *i.e.* by varying the three optical properties μ_s , μ_a and g . This was performed by using a conventional numerical minimisation algorithm, the Downhill simplex method.¹²⁴

When selecting an appropriate light propagation model for the iteration procedure, it is clearly of great advantage to have a good insight into the assumptions being made of the theoretical derivations of the models and also basic knowledge of tissue optics in practice. In this work (Paper I to Paper IV) the transmittance and reflectance were measured of a thin tissue sample placed between two glass slides utilising an integrating sphere set up (see Chapter 6.3). The rather simple sample geometry and the requirement of a model yielding results of high accuracy, without any restrictions in the optical parameters, leave us with two computation alternatives based on either the adding-doubling or the Monte Carlo method. An iterative program based on adding-doubling computations, the so-called inverse

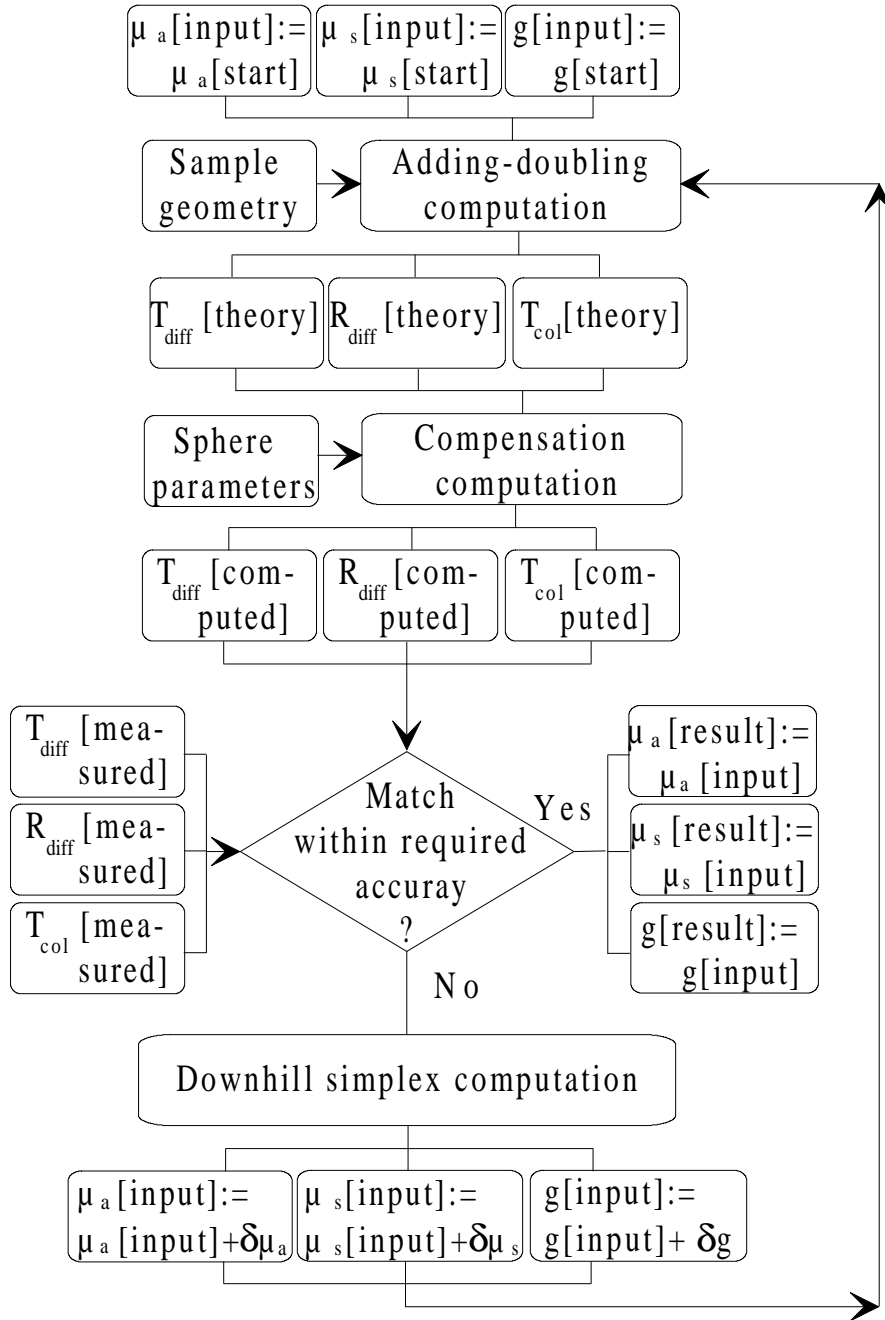


Figure 5.1 The simple flow chart schematically describes the iteration procedure used in the IAD-program to solve the indirect problem.

adding-doubling program (IAD), has been realised by Prahl *et al.*³⁹ and a simple flow chart of the procedure is shown in Figure 5.1. When utilising this program, the radiance was discretised into four cones yielding a so-called four flux model. Adding-doubling computations are significantly faster than conventional Monte Carlo simulations, which due to the many iterations needed in the fitting procedure, more or less, excludes the latter alternative. However, the Monte Carlo approach was in this work (Paper I and Paper II) made more attractive, by developing a data base with transmittance and reflectance values originating from thousands of Monte Carlo simulations, employing the program by Wang and Jacques.⁴⁷ Each simulation was performed with 100 000 photons for optical properties in the range of 2.5-25.0 mm⁻¹ for μ_s , 0.02-4.0 mm⁻¹ for μ_a and 0.675-0.999 for the g-factor. Examples of the values for g=0.9 are shown in Figure 5.2. The simulations were made for a one millimetre thick tissue sample surrounded by the two glass slides.

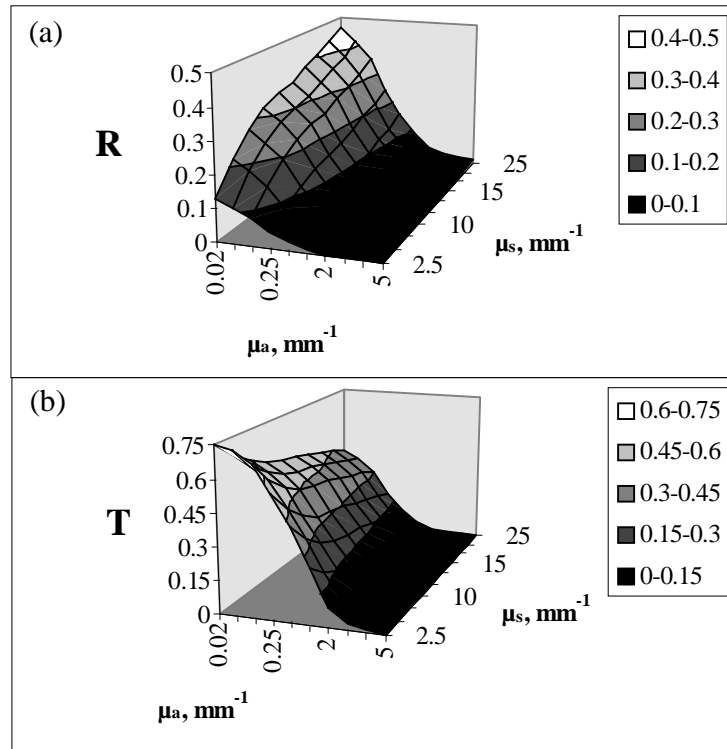


Figure 5.2 Monte Carlo simulated a) reflectance and b) transmittance values are shown versus the scattering and absorption coefficients for g=0.9. This data is a subset of the data base used in the inverse Monte Carlo program employing spline interpolation.

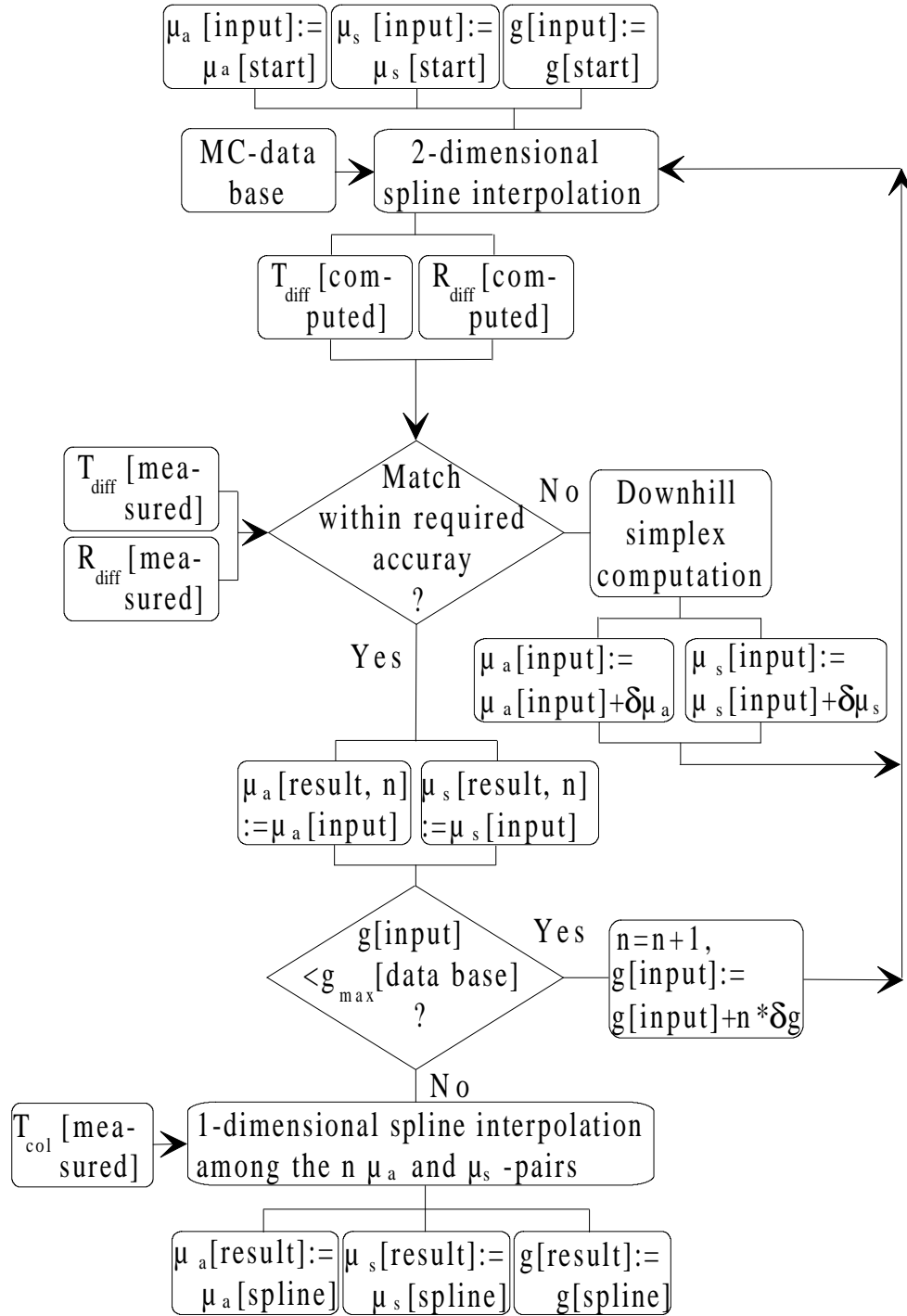


Figure 5.3 The brief outline schematically describes the iteration procedure used in the ISMC-program to solve the indirect problem.

A two-dimensional spline interpolation routine was then employed for each g-factor in the data base, to extract the Monte Carlo simulated transmission and reflection values, corresponding to a pair of absorption and scattering coefficients (μ_s , μ_a). This results in an array of possible μ_s and μ_a pairs versus the g-factor. A final one-dimensional spline interpolation over all g-factors is thus needed, with the total interaction coefficient ($\mu_t = \mu_s + \mu_a$) as input parameter, derived from measurements of the collimated transmittance employing Beer-Lambert's law in Eq. 4.25. Hence, from three measured parameters (R, T, μ_t), we are able to deduce a complete set of optical properties (μ_s , μ_a , g) with computation times equivalent to those of the IAD-program (in the order of a few seconds). A brief outline of the inverse spline Monte Carlo (ISMC) program, written by the author, is shown in Figure 5.3.

Simulating the light transport through a one millimetre thick sample does not imply any restrictions in the sample thickness used for the measurements, since the total transmittance and reflectance are linearly dependent on this parameter. For instance, when transmission and reflection data are measured for a sample half as thick, the computed scattering and absorption coefficients would simply be doubled and the g-factor remains the same. This follows from the concept of Monte Carlo simulations and has been checked by the author for a number of optical properties.

The deviation of 10^{-6} between computed and measured transmission and reflection data, was allowed in the fitting procedure in the ISMC-program. Yet, the accuracy in terms of the derived optical properties might be a more meaningful parameter which must be examined and formally compared to the accuracy given by the alternative method, *i.e.* the IAD-program. The accuracy was tested by simulating approximately 1000 transmittance and reflectance reference pairs, with input parameters in the range $6 < \mu_s < 24 \text{ mm}^{-1}$, $0.05 < \mu_a < 1.85 \text{ mm}^{-1}$, $0.80 < g < 0.98$, using the direct Monte Carlo method. These reference pairs were used together with the total interaction coefficient ($\mu_t = \mu_s + \mu_a$) as input data, both for the inverse spline Monte Carlo program and the inverse adding-doubling program. The calculated optical properties were finally compared with the input data used for the reference Monte Carlo simulations. The relative errors obtained from the ISMC-program were all lower than one percent for the two scattering parameters and lower than 1.5% for the absorption coefficient, except for a few computations. Slightly larger relative errors are thus obtained for the absorption coefficient, which can probably be explained by the small absolute values of this parameter, as compared to the scattering coefficient.

The exceptions (approximately ten out of thousand computations) mentioned were found for combinations between largest absorption and scattering coefficients. The spline interpolation routine then fails to find a minimum, yielding optical

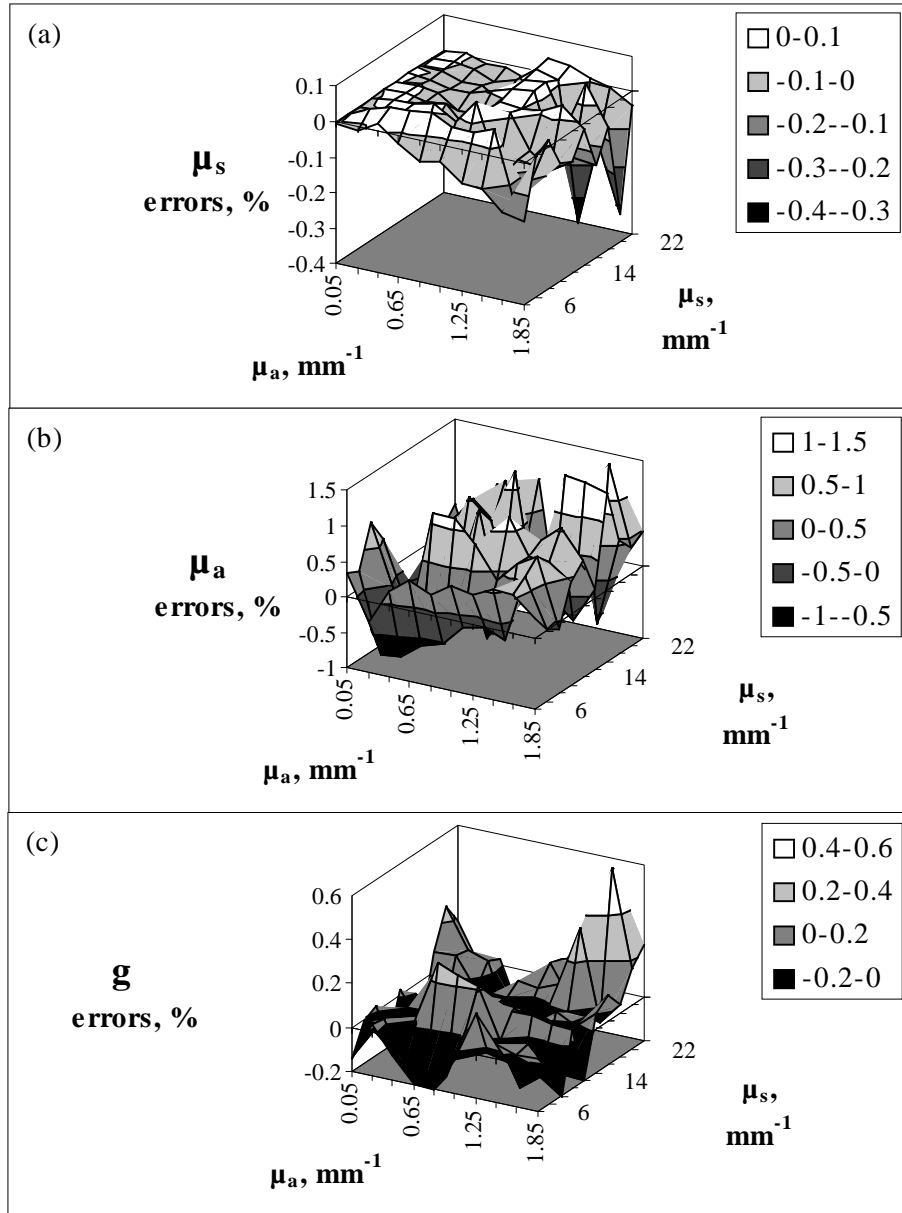


Figure 5.4 The surface plots show examples of relative errors of the a) scattering coefficient, b) absorption coefficient and c) g-factor obtained for the ISMC-program. The relative errors are shown in percentage versus the absorption and scattering coefficients used as input data. The results presented here are all for $g_{\text{indata}} = 0.9$, but are representative for all g-factors in the range 0.8-0.98.

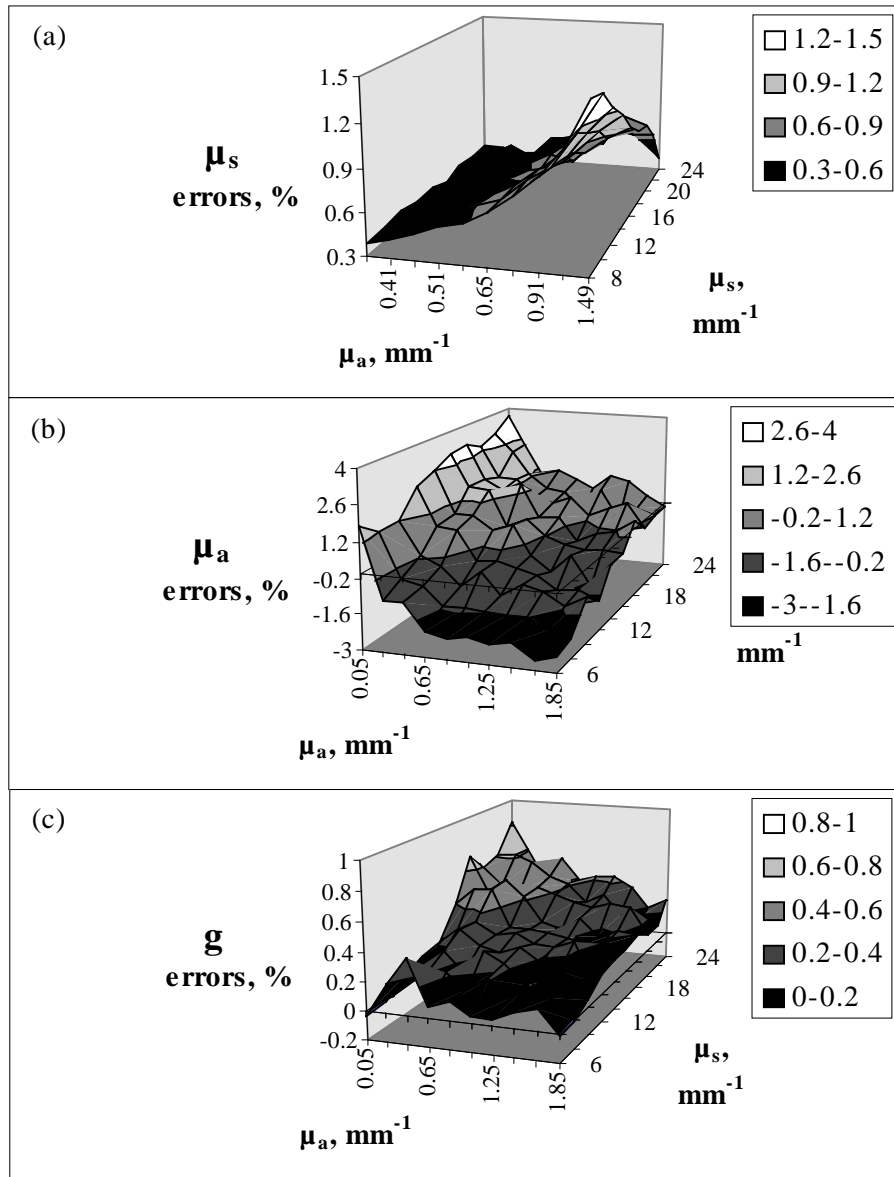


Figure 5.5 The surface plots show examples of relative errors of the a) scattering coefficient, b) absorption coefficient and c) g-factor obtained for IAD-program. The results are here presented in the same way as in Figure 5.4, again with $g_{\text{indata}}=0.9$, though representative for all g-factors in the range 0.8-0.98.

properties far from those supporting the data base. However, this is not a problem in practice, since the computed reflectance and transmittance values were both in the order of 0.01-0.03, which experimentally is an unrealistic combination. Examples of the deviations given by the error analysis of the inverse Monte Carlo approach for $g=0.9$ are shown in

Figure 5.4. This shows that largest errors (though still lower than 1 and 1.5%, respectively) are obtained in the rear, right corner of the surface plots corresponding to a combination of large absorption and scattering coefficients. The relative errors obtained in the IAD-program are larger than those of the ISMC-program, but still less than 2 and 5% for the scattering and absorption coefficients, respectively, and less than 1% for the g-factor. Examples of the relative errors obtained for $g=0.9$ are shown in Figure 5.5. The largest errors were for the scattering coefficient obtained for combinations of low scattering and large absorption coefficients, while the absorption coefficient and g-factor exhibit large deviations for a combination of high scattering and low absorption coefficients. Furthermore, a comparison of the surface plots shown in Figure 5.4 and Figure 5.5, indicates different types of errors. It seems as if the relative errors obtained by the ISMC-program have a stochastic character, in accordance with the stochastic nature of the Monte Carlo approach, whereas the errors obtained by the IAD-program seem to be more systematic, since they tend to be dependent on the optical properties.

In order to evaluate the influence of the finite lateral extension of the tissue sample on both computational methods, the original Monte Carlo code⁴⁷ was modified to include lateral boundaries. These were modelled as glass slides, corresponding to the experimental circumstances. Computations were performed utilising both the original Monte Carlo program and the boundary program for $\mu_s = 25 \text{ mm}^{-1}$, $\mu_a = 0.20 \text{ mm}^{-1}$ and $g = 0.90$. The lateral extension was first set at $5 \times 3 \text{ cm}$, equivalent to the authentic sample size used in the experiments described in Paper I and Paper II, and then followed by $2 \times 2 \text{ cm}$ and $1 \times 1 \text{ cm}$. The vertical geometry of the sample was equal to that used when forming the ISMC-program, *i.e.* a one millimetre thick sample, with a refractive index of 1.4, mounted in-between two glass slides (each 1 mm thick with refractive index of 1.52). In order to estimate the errors in terms of the optical properties, IAD-computations were performed assuming $g=0.90$ and with the reflectance and transmittance data from the Monte Carlo simulations, as input data. The results are presented in Table 5.1, these reveal no significant influence of the lateral boundaries for the $5 \times 3 \text{ cm}$ sized sample, since the deviations in the reflectance, absorbance and transmittance are less than 1% and the accompanying errors of the IAD-computed optical properties (μ_s : -0.3% and μ_a : 3.3%) are within the uncertainty of the IAD- method itself (μ_s : -0.5% and μ_a : 2.3%). For the $2 \times 2 \text{ cm}$ sized sample a slight influence can be observed, with deviations greater than 1% in the reflectance and transmittance data obtained from the boundary computations, which caused larger errors than those normally obtained by the IAD-method. Finally, a significant influence of the boundaries can be seen for the $1 \times 1 \text{ cm}$ sized sample these are in the order of 10% for the reflectance, absorbance and transmittance. In consequence the IAD-method was only able predict absorption coefficients to within $\pm 20\%$. Hence, when samples are used with smaller dimensions than experimentally employed by us, the boundary

Table 5.1 Results obtained when incorporating lateral sample size in the Monte Carlo (MC) simulations (Boundary MC) are shown both in absolute and relative values. Input data were $\mu_s = 25 \text{ mm}^{-1}$, $\mu_a = 0.20 \text{ mm}^{-1}$, $g = 0.90$, sample thickness = 1 mm and refractive index=1.4.

| | Original MC | Boundary MC | Boundary MC | Boundary MC |
|--------------------------|-------------|-------------------------|-------------------------|-------------------------|
| Lat. sample size | infinite | $5 \times 3 \text{ cm}$ | $2 \times 2 \text{ cm}$ | $1 \times 1 \text{ cm}$ |
| Diff. reflectance | 0.271 | 0.270(-0.4%) | 0.266(-1.9%) | 0.249(-8.2%) |

| | | | | |
|-----------------------|---------------|---------------|---------------|---------------|
| Absorbance | 0.467 | 0.468(0.1%) | 0.461(-1.3%) | 0.427(-8.6) |
| Transmittance | 0.218 | 0.216(-0.8%) | 0.214(-1.8%) | 0.198(-9.4%) |
| | IAD | IAD | IAD | IAD |
| μ_s | 24.869(-0.5%) | 24.923(-0.3%) | 24.778(-0.9%) | 24.730(-1.1%) |
| μ_a | 0.2045(2.3%) | 0.2066(3.3%) | 0.2116(5.8%) | 0.2406(20.3%) |
| g (input data) | 0.9 | 0.9 | 0.9 | 0.9 |

effect should and can be taken into account by the ISMC-program, but not by the IAD-program. A new data base could simply be formed for the ISMC-program from boundary Monte Carlo computations. Thus, in contrast to the IAD-method, the geometry of the tissue as modelled by the ISMC-method is not restricted to infinite layers. In conclusion, the immense computations related to defining the data base for the ISMC-program, are avoided when employing the IAD-program. However, once the data base is defined for the ISMC-program, both methods are equally time efficient. Advantages gained by employing the ISMC-method are better accuracy and flexibility concerning the geometry of the modelled tissue sample.

5.2 Computations treating the direct problem

Naturally, single adding-doubling computations or Monte Carlo simulations are primarily used to solve the direct problem, *i.e.* to derive the light distribution from known optical properties. This is for instance accomplished in Paper II, using optical properties, determined from untreated and thermotherapy treated liver tissue, as input parameters in two separate Monte Carlo computations. This was performed in order to illustrate the significant influence of the changes in the optical properties, as induced by the treatment, on the distribution of treatment light in the tissue and thereby most likely on the outcome of the treatment.

Other programs applied to the direct problem in this work are Mie theory⁹⁹ and T-matrix programs¹²³ founded on the electromagnetic theory. They can be used to analyse light scattering from a suspension of well-separated particles rather than from a continuous medium. The Mie theory program has in Paper I and Paper II been employed to quantify the light distribution from a single spherical particle in terms of the total scattering cross section, using Eq. 4.71 integrated over the entire solid angle, and the g-factor. The scattering coefficient of a suspension containing numerous, but well-separated, spheres is then simply obtained by multiplying the total scattering cross section by the particle density, *i.e.* the number of spheres per unit volume. The error in the computed parameters have been shown to be less than 0.0003%.⁹⁹ Input parameters to the Mie theory program are the size parameter, x , equal to $2\pi n'_{sm}a/\lambda$ (n'_{sm} is the real part of the refractive index of the surrounding medium, a is the radius of the sphere and λ is the wavelength of the incident light) and the relative refractive index, m , equal to n_{sphere}/n_{sm} (both real and imaginary parts). Assuming constant refractive indices of both the scattering particle and the surrounding medium, Mie theory computations can be used to derive the theoretical dependence of the scattering properties on the wavelength and sphere size.^{14,125} This was carried out in Paper II, in order to estimate an average size of the main scatterer in liver tissue from spectra of scattering coefficients and g-factors.

Corresponding computations for oblate and prolate spheroids can be performed utilising the T-matrix programs.¹²³ These consist of three separate programs with input parameters such as the familiar size parameter x and relative refractive index m , but owing to the non-spherical shape, also the axial ratio of the spheroid (radial component along the symmetry axis divided by that perpendicular) and the angle of the incident wave versus the symmetry axis. The first program decides after how many terms the expansion series of the scattered field (see Eq. 4.62) can be truncated, by comparing the differential scattering cross sections (Eq. 4.71) computed for N and $N+1$ expansion terms. The original program allows a deviation of 1%, but this convergence criteria was changed to 0.1% for our computations presented in Paper V. This modification together with the incorporation of extended precision variables, replacing the single precision, and also allowing larger dimensions of the T-matrix, were included in order to attain a convergent solution for large and highly aspherical particles, such as an oblate spheroid with a volume ($94 \mu\text{m}^3$) equal to that of a normal red blood cell (RBC).¹²⁶ For an axial ratio of 0.33, close to that of the RBC oblate spheroid (0.375), convergent solutions were only obtained for size parameters lower than 3.5 using the original program.¹²³ The upgraded program, used in Paper V, allowed size parameters up to 22. This is a significant improvement, and more importantly, enough to be able to compute the light scattering by a RBC volume equivalent oblate spheroid with a size parameter at the wavelength 633 nm of 19.6. As a convergence check, the T-matrix program also sets the number of integration points required for accurate evaluation of the elements of the T-matrix, *i.e.* the surface integrals. When all convergence parameters are settled, the T-matrix is finally calculated and stored to be used by any of the other T-matrix programs. Either the angular distribution of the far field (*i.e.* far from the spheroid when the E-field decays with a radial dependence of $e^{-1 \text{ kr}/r}$, $k=2\pi/\lambda$) can be derived for all directions of the scattered light in space using the second program, or the near field (stronger r -dependence and attenuates more rapidly) immediately surrounding the spheroid can be computed by the third program. Both computations were performed for RBC volume equivalent spheroids in the work presented in Paper V.

6. Optical properties - measurement techniques

In order to establish our theoretical computations, still predominantly based on the radiative transport theory in the reality, the optical properties must be experimentally determined. The simplest and most straight forward method to characterise of the light distribution in tissue in practice, is to determine the decay of the light intensity as a function of the penetration distance in the tissue. By insertion of light collecting detection fibres and by varying their distance from the light source, the penetration depth in the tissue can be determined.^{6,7} If instead the detection fibres are kept at a fixed distance from the light source, changes in the light penetration depth can be monitored, for instance in conjunction with laser-based treatments,¹²⁷ as found during photodynamic therapy, see Paper I. However, there is frequently great interest in extracting more detailed information on the light-tissue interactions, *i.e.* to separately quantify the scattering, absorption and scattering anisotropy properties of the tissue. There exist a wide variety of measurement techniques,¹⁷ enabling the derivation of one, two or all of these parameters. Apart from the number of parameters extracted, the methods differ in applicability to tissue *in vivo* or *in vitro*. A brief survey over the main techniques will be given here, although it focuses on the integrating sphere method employed in this work (Paper I to Paper IV).

6.1 One-parameter techniques

There is a group of measurement procedures where one of the optical tissue parameters can be directly derived without any extensive computations or simulations, provided that the measurements are performed on thin, single-scattering samples *in vitro*. The *narrow-beam method* (see Figure 6.1a) is such a technique, where the collimated transmittance is measured, *i.e.* the fraction of light passing straight through the sample without interacting with the tissue. The total interaction coefficient, $\mu_t = \mu_s + \mu_a$, can then be calculated using the law of on-axis exponential attenuation (Beer-Lambert's law Eq. 4.25), and knowing the thickness of the sample.^{128,129} This type of measurement can also be performed for optically relatively thick samples, provided the multiple scattered light is prevented from reaching the detector (large distance between sample and detector and small apertures in front of the detector). The scattering and absorption coefficients can also be separately determined, by placing thin samples in the *centre of an integrating sphere* (see Figure 6.1b).^{129,130} An integrating sphere is simply a hollow

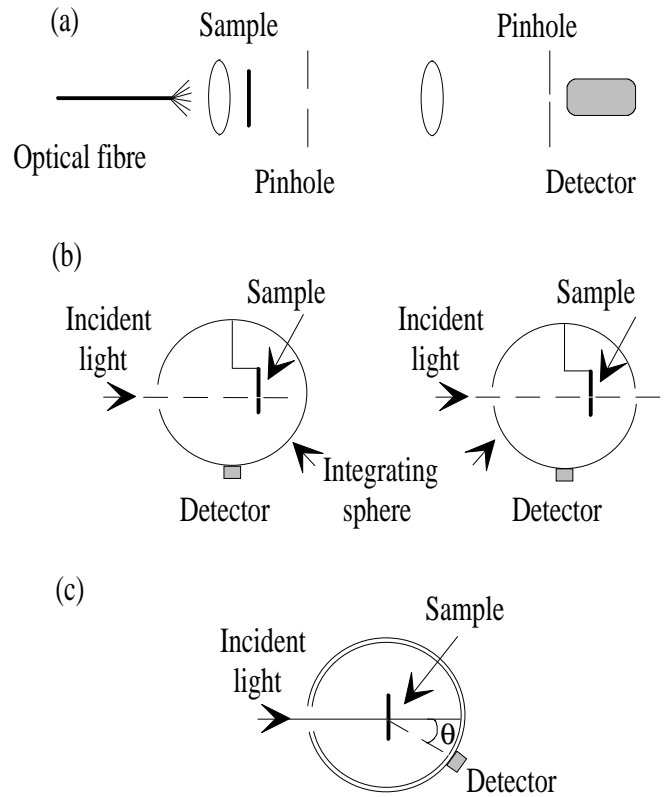


Figure 6.1 The principles of three one-parameter techniques, employed to determine the optical properties, are schematically illustrated: (a) the narrow-beam set up, (b) absorption (left) and scattering (right) measurements utilising an integrating sphere with the sample mounted in the centre and (c) a goniometric apparatus.

sphere with the inner surface covered with a both highly and diffusely reflecting material, such as barium sulphate, apart that is from the small area occupied by a detector. Thus, the detector measures a certain fraction of the light flux filling the sphere. When a sample is mounted inside the sphere, the loss of light compared to the sample free control, is mainly due to absorption by the sample, related to the absorption coefficient. When the on-axis, transmitted light is allowed to escape out of an exit port in the rear end of the sphere, the scattered light from the sample mounted inside the sphere is measured, and the scattering coefficient can be determined. Finally, the goniometric technique can be used to estimate the angular distribution of single-scattering events, which can be correlated to the phase function, or the g-factor (see Figure 6.1c).^{18,20,31,128,129} The scattered light from an optically thin tissue sample is here determined as a function of the scattering angle relative to the incident beam.

6.2 Two-parameter techniques

There are a growing number of sophisticated measurement techniques allowing two parameters, $\mu_s' = \mu_s(1-g)$ and μ_a , to be determined. These can often be applied to dense

tissue, *i.e.* *in vivo* measurements are possible. This is a great advantage, since the optical properties are most likely affected as the tissue is resected and prepared, utilising various techniques. In general, they all involve some measurements of the amount of transmitted light through, or reflected light by the tissue, followed by inverse computation or fitting procedures, described in the previous chapter, to deduce the optical parameters from the measured quantities.

6.2.1 Spatially resolved techniques

The concept of spatially resolved methods is to monitor the quantity of diffusely reflected continuous light, as a function of the distance from the centre of the incident beam, as depicted in Figure 6.2a. Discrete detection with optical fibres^{66,107,131} or imaging techniques^{132,133} can be used with normal, as well as oblique incidence light. Since the shape of the radial dependence of the reflection is determined by the optical properties of the tissue, the absorption and the effective scattering coefficients can be derived from this information. A low absorption coefficient allows photons of longer propagation history to be detected, yielding higher reflectance in the peripheral regions of the reflectance pattern, whereas tissue with stronger effective scattering, corresponding to a high μ_s' -coefficient, produces greater reflectance over the entire radial range. A more isotropically scattering tissue, also with high μ_s' -coefficient, results in higher reflectance close to the centre. The absolute values of the reduced scattering and absorption coefficients can be obtained, either by fitting an analytical expression for the radial dependence, generated by the diffusion approximation,^{66,107,132} or by means of a neural network trained on spatially resolved reflection data utilising the diffusion approximation¹³⁴ or Monte Carlo simulations.¹³³ This enables the determination of two optical properties by means of relatively simple and inexpensive equipment with estimated errors ranging between about 3-15%.^{66,133} However, as several measurements are required along a radial extension from the incident beam, in order to determine one set of optical properties, the accuracy is sensitive to local property variations.

6.2.2 Time-resolved techniques

Time-resolved reflectance or transmittance measurements, are schematically illustrated in Figure 6.2b, of tissue is possible using a picosecond pulsed light source combined with a fast detector, such as a streak camera.

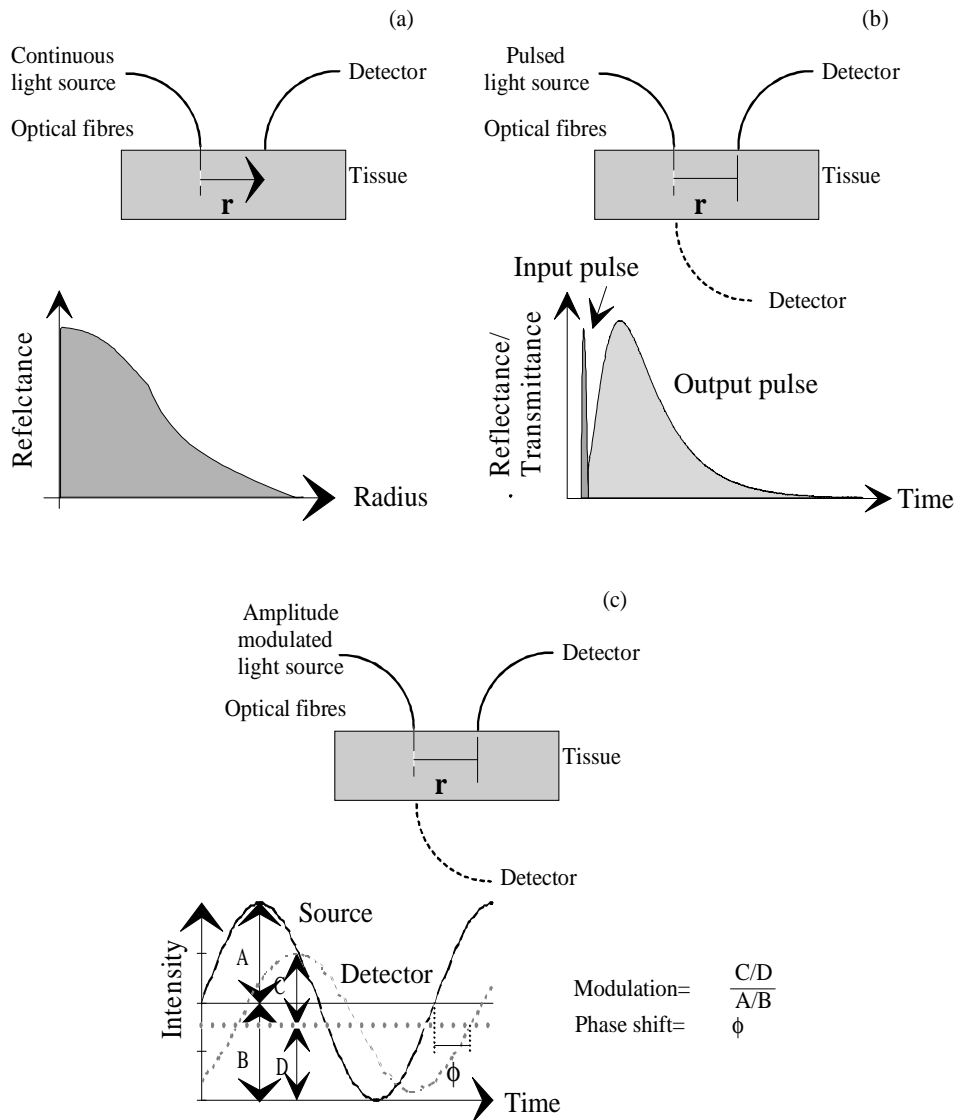


Figure 6.2 The principles of three two-parameter techniques, employed to determine the optical properties, are schematically illustrated: (a) spatially resolved measurements, (b) time resolved measurements and (c) frequency domain measurements.

It can be shown that the temporal behaviour of the scattered pulse following the short, incident pulse is characteristically influenced by the optical properties.^{64,65,67,68,71,135} The absorption coefficient mainly influences the final slope of the reflectance/transmittance-versus-time attenuation curve. A low absorption coefficient allows more “long-lived” photons to be registered and yields consequently a less negative final slope than tissue with higher μ_a . The reduced scattering coefficient primarily affects the temporal behaviour of the peak reflectance/transmittance value measured following each pulse. Scattering increases the effective path length in the tissue and the time. This means that less rapid photons are

recorded with higher effective scattering and the peak value of the time-resolved reflectance/transmittance curve is shifted to longer recording times. By analysing the shape of the temporal curves, using an analytical expression for the temporal dependence derived from the diffusion approximation,⁶⁴ the two optical properties can be determined. Comparison with measurements on tissue phantoms of known optical properties have shown that the errors are essentially in the order of or less than 10%.^{65,67,71} Alternatively, fitting procedures based on data obtained from time-resolved Monte Carlo simulations can be employed.^{83,93} When evaluating the concept by performing experimental measurements of phantoms, significantly better results were obtained, with errors less than 10% over a wider range of optical properties, compared to when fitting the data using the diffusion approximation.⁸³ Thus, this technique allows the determination of the optical properties with reasonable accuracy.

6.2.3 Frequency domain measurements

When a sinusoidally amplitude-modulated beam is propagating through tissue, it can be thought of as a photon density wave, associated with a certain phase velocity and wavelength. Depending on the absorption and scattering properties in the tissue, the phase of this wave is shifted and its amplitude relative to the average level, also called the amplitude modulation, is to various degrees decreased. This is illustrated in Figure 6.2c. A Fourier transformation of the time-resolved diffusion theory formula, yields analytical expressions for the relationships between both the phase shift and modulation on one hand and the absorption and reduced scattering coefficient on the other. It can be shown that a decreasing absorption coefficient, or increasing effective scattering coefficient results in a larger phase shift and a weaker modulation,¹³⁶⁻¹³⁸ at constant source-detector distance and modulation frequency. After measuring the phase shift and modulation versus the modulation frequency, expressions derived from the diffusion theory can be used to determine absolute values,^{136,138-140} or relative changes,¹² of the two optical properties μ_s' and μ_a . Measurements on intralipid phantoms by Madsen *et al.*¹⁴⁰ showed reasonable agreement between measured values and reference data, as long as not too high modulation frequencies were required in order to obtain good dynamics in the frequency dependent phase shift and modulation curves. This sets an upper limit for the absorption coefficients determined. The absorption coefficient of the phantom was relatively low, in the order of 0.01 mm^{-1} , resulting in an average deviation from the reference value of approximately 15% and for the reduced scattering coefficient an average deviation close to 5%. The measurement procedure requires a large number of sequential measurements, while varying the modulation frequency. Alternatively, the measurements can be conducted in the time-domain by recording the time-dispersion curve of one short light pulse, which has propagated through the tissue. Fourier transformation of the pulse yields a broad spectrum of sinusoidal components of various frequency. Thus, information on the light propagation of frequency modulated signals can be obtained in a broad frequency range by analysing the propagation of just one short pulse.¹⁴¹ This favours time-resolved measurements, and also indicates on the close relation between time- and frequency-domain measurements.

6.2.4 Other techniques

Several other techniques of determining the optical properties have been described, some of which are rather specialised. *Pulsed photothermal radiometry* is an optothermal technique based on measurements of one of the secondary phenomena associated with light

absorption, *i.e.* of the resultant increase in temperature. The time dependence of the infrared emission following an incident light pulse is monitored and a fitting algorithm based on an analytical expression derived from the diffusion approximation can be used to deduce the absorption and reduced scattering coefficients with an accuracy ranging between 10-15%.¹⁴² The *coherent backscattering* technique based on the constructive interference of the incident and backscattered waves, can be used to determine the two optical parameters. This results in a coherent peak, with an angular width inversely proportional to the mean free path in the tissue, *i.e.* the reciprocal of the total interaction coefficient $1/\mu_t$. Curve-fitting to an existing theoretical expression, or Monte Carlo simulated data for the angular distribution of the coherent peak, provides a reduced scattering coefficient with a reasonably good accuracy for highly scattering tissue.^{143,144} However, too high absorption coefficients are invariably estimated. *Low-coherence reflectometry* can be thought of as a technique which determines the intensity of the backscattered light at a certain depth in the tissue, without performing any direct measurements by inserting optical fibres. This light is instead probed by scanning a reference mirror in a Michelson interferometer, with the sample located in the end of the other arm. Interference occurs between the reference light and that originating from a specific depth within the tissue. By moving the reference mirror, different tissue depths are probed. The total interaction and backscattering coefficients can be measured with a discrepancy, estimated from phantom measurements, of less than 10%.¹⁴⁵ *Laser-Doppler flowmetry* is a technique where the power spectra of Doppler shifts (number of registered photons versus their frequency shift) are obtained from suspensions of moving particles. These spectra contain information on the total interaction coefficient and the g-factor. For instance, a large g-factor results in a decrease in the number of photons with large frequency shifts. This is because the Doppler shifts obtained are proportional to sine of half the scattering angle, which is small for large g-factors. The two optical scattering parameters can be quantified by fitting Monte Carlo simulated laser Doppler spectra to that obtained experimentally.³⁰ Finally, the *diffuse backscattering of linearly polarised light* technique yields patterns with characteristic radial and azimuthal variations, which depend on the scattering coefficient and the g-factor of the suspension studied.¹⁵

6.3 The integrating sphere method - a three parameter technique

A complete set of optical properties (μ_s , μ_a , g) can be determined by utilising an integrating sphere arrangement. This technique enables local measurements on thin and small tissue samples, which is not possible with the other techniques previously referred to, *i.e.* the optical properties of not only individual tissue structures but also small organs (such as rat livers in connection with animal studies) can be evaluated. Integrating sphere measurements can only be performed on *in vitro* samples. This is one of the major drawbacks of the method, since the physiological conditions (blood flow, metabolism, oxygenation saturation, degradation products etc.) differ from those of tissue *in vivo*. Moreover, the sample preparation induces changes in the tissue, these include dehydration.⁷³ In order to probe realistic optical properties, care must be taken when preparing the samples and measurements must be exclusively performed on fresh samples.

The integrating sphere approach is essentially a two-parameter method, where total/diffuse transmittance through and diffuse reflectance from a thin tissue sample (usually with a thickness of 0.1-1 mm) are measured by collecting the corresponding light flux within an integrating sphere. The transmittance is probed by mounting the sample at the entrance port of the sphere, facing the light source, and the reflectance is measured by placing the sample

at the rear exit port of the sphere, as shown in Figure 6.3a and b, respectively. The significance of an integrating sphere is that it enables measurements of light, globally propagating from a sample and integrated over all solid angles using one detector situated on the inner sphere wall. This is possible since the inner sphere surface is covered with highly reflecting barium sulphate, yielding a Lambertian distribution of the reflected light, *i.e.* with equal radiance L [$\text{W m}^{-2} \text{sr}^{-1}$] in all directions. Due to the spherical geometry, this means that the reflected power [W] is homogeneously distributed over the entire inner surface of the sphere. Thus, the power registered by the detector is proportional to the total reflected/transmitted power with a proportionality factor equal to the detector area divided by the total sphere area. By combining the sample measurements with reference results using a barium sulphate plug of known reflectance in the exit port of the sphere, the ratio of the two measured powers is essentially equal to the reflectance or transmittance. A more rigorous analysis can be carried out, employing fundamental integrating sphere theory based on the multiple reflectance in a cavity.^{146,147}

The sphere results are regularly combined with a third measurement utilising a one-component technique, in order to extract all three optical properties. A goniometric set up has been used¹⁴⁸ to separately measure the g-factor. However,

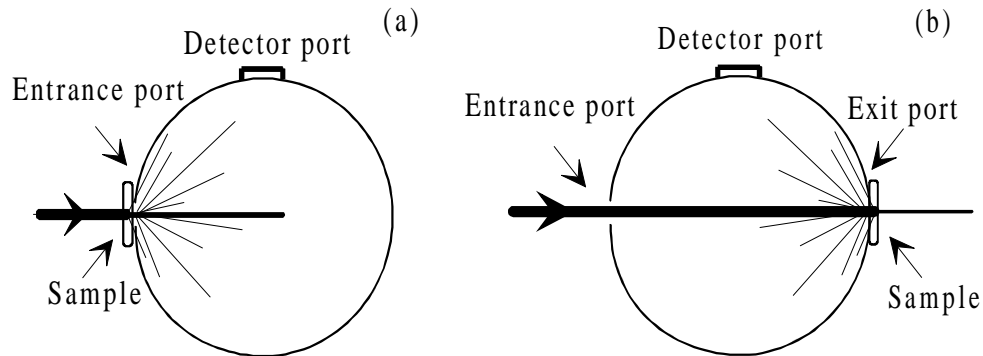


Figure 6.3 The configuration used when measuring a) the total transmittance and b) the diffuse reflectance with an integrating sphere. Alternatively, the diffuse transmittance can be measured by letting the collimated light passing straight through the sample, mounted as in a), escape out of the exit port at the rear of the sphere. The specular reflection, *i.e.* the Fresnel reflection originating from the surface and thus the difference in refractive index of the sample and the surrounding medium, is not probed in the reflectance measurement but escapes the sphere through the entrance port.

the most common procedure is to perform a narrow-beam measurement on a thin tissue sample and apply the Beer-Lambert's law, in order to derive the total interaction coefficient, $\mu_t = \mu_s + \mu_a$, (see Eq. 4.25). Thus, the two scattering parameters, the g-factor and the scattering coefficient, incorporated in the reduced scattering coefficient can be isolated. The measured parameters (reflectance, transmittance and μ_t) are used as input variables for any of the models and methods described in Chapters 4 and 5, in order to derive the corresponding optical properties.

6.3.1 Sources of errors in the sphere measurements

Due to losses at for instance the sphere ports, on the barium sulphate and detector surfaces, we are not detecting the total reflected/transmitted power. This would be of no concern, if the losses for the sample measurements were equal to those of the reference, since we are concerned with the ratio. Unfortunately, this is not quite the situation, owing to the differences in the angular distribution and quantity of reflected light in the first reflection event from the Lambertian reflectance of the barium sulphate plug compared to the more forward scattering tissue sample. Correction factors to compensate for these differences have thus been derived.¹⁴⁹⁻¹⁵¹ It has been shown¹⁵¹ that the compensation factor for a single sphere, with a sample area of approximately 0.35% of the total sphere area, as in our case (Paper I and Paper II), is close to unity (in the order of 1.05) and can therefore be neglected irrespective of sample reflectance and angular distribution of the reflected light flux. This was confirmed by Monte Carlo simulations of the 1 mm thick samples used (Paper I and Paper II), which found they approximated to Lambertian reflected light fluxes. Moreover, calibration measurements on standard plugs of known reflectance have been performed, showing small deviations in the order of $\pm 1\%$. Thus, this seems to be a reasonable estimation of the measurement errors obtained from the single integrating sphere measurements. A deviation of one percent in the input data (reflectance and transmittance) to the inverse spline Monte Carlo program corresponds to a deviation in the order of 0.5-3% in the optical absorption and scattering properties. A larger relative sample area, such as that of the spheres used in Paper III and Paper IV (in the order of 1%), yields significantly higher compensation factors (>1.1) dependent on the reflectance of the sample.¹⁵¹ The compensation factor has been taken into account partly due to this, but because two spheres were employed in a so-called double integrating sphere set up, also in order to compensate for the exchange of light between the two adjacent spheres. Thus, double-sphere measurements always require careful compensation computations for reasonable accuracy, more or less irrespective of the size of the relative sample area. However, the use of compensation factors does not necessarily guarantee accurate results. One must also consider the assumptions being made in order to derive the compensation factors. For instance, accurate compensation can be obtained utilising the compensation factors derived by Pickering *et al.*,^{149,150} provided the angular distributions of the transmitted and reflected light from the sample are similar to a Lambertian light flux. This requires optically thick samples of low forward scattering. A compensation is thus needed for non-Lambertian behaviour in conjunction with optically thin samples, when the relative sample and exit/entrance port area of the sphere/spheres is large, and also always for a double-sphere arrangement (larger effect due to the interaction of the light flux in the two spheres). Since such a compensation would have been necessary for the measurements on the forward-scattering blood in Paper IV, in order to attain reasonable accuracy, no absolute values of the complete set of optical properties were presented. The reported lack of compensation of the non-Lambertian behaviour can probably partly explain the reported dependence of the derived optical properties on the sample thickness when using an integrating sphere set-up.³⁵

The Monte Carlo computations incorporating lateral boundary conditions reveals that too small samples can also violate the accuracy of the sphere measurements. They should be in the order of 2×2 cm and cover the entire sample port of the sphere. Furthermore, Torres *et al.*¹⁵² have pointed out the importance of having a large port-to-beam diameter ratio, in order to not to overestimate the absorption coefficient due to lateral losses. Large beams, with dimensions in the order of 0.5-1 cm, generated by several common lamps and spectrometers should therefore not be used directly for integrating sphere measurements.

This was avoided in Paper I and Paper II by guiding the light along an optical fibre from the light source (a Xe-lamp) to the sample mounted on the integrating sphere and in Paper III and Paper IV by the use of a laser as a light source. This resulted in a precise, circular beam with dimensions of a couple of millimetres, compared to the 2.5 cm large diameter of the entrance and exit ports.

The optical properties are derived not only by employing the Monte Carlo approach, but by any of the previously discussed theoretical models. Some models are less appropriate than others, due to the thin geometry of the tissue; for instance those assuming completely diffuse light scattering, as the Kubelka-Munk method, or the diffusion approximation. An alternative procedure in order to satisfy the assumptions used in these models, is to employ a diffuse light source.^{59,60} Instead of guiding the collimated probe beam directly onto the sample, it can be focused onto the sphere surface, yielding Lambertian reflected light which forms a diffuse light flux inside the sphere, incident on the sample.

6.3.2 Sources of errors in the narrow-beam measurements

The narrow-beam set-up, complementing the integrating sphere method in order to derive all three optical properties, is usually arranged separately from the single^{74,78,153,154} or double^{31,59,60} sphere set-up. This is done partly for practical reasons, but also because measurements employing an integrating sphere using larger relative sample and entrance/exit port area, requires optically thicker samples to obtain reasonable accuracy, in contrast to the thin samples preferred for the narrow-beam measurements. As discussed earlier, optically thick samples yield Lambertian reflected and transmitted light distributions in the sphere/spheres are necessary to minimise the discrepancies in actual light losses compared to those accounted for.

The narrow-beam measurement can be performed on optically thicker tissue samples as well, but this requires careful separation of all the scattered light from the small fraction that passes straight through the sample without interacting with the tissue. The error increases linearly with sample thickness and scattering coefficient, quadratically with the collection angle of the detector, and is inversely quadratically proportional to $(1-g)$ and to the refractive index of the sample.¹⁵⁵ For optically thick samples, one is also limited by the dynamic range of the detection system. The measurements include recording the unattenuated beam (reference measurement), as well as that passing through the tissue. The limitations posed by the dynamic range in the detection can partly be overcome by using calibrated neutral density filters in the light path for the reference measurement, as performed in this work (Papers I, II, and IV). Moreover, the noise level originating from the scattered light can be suppressed by placing two polarising filters with parallel polarisation axes before and after the sample respectively.^{78,154} Thus, the range of optical thickness of the tissue sample, for which narrow-beam measurements are undertaken with reasonable accuracy, can be increased.

The narrow-beam error is not only influenced by the parameters discussed earlier (sample thickness, light collection angle of the detection, refractive index and the scattering properties of the sample), but also on something so trivial as the ability to measure the thickness of the sample, an important parameter in Beer-Lambert's law (see Eq. 4.24). This measurement must be performed with an error in the order of, or less than five percent, so as not to be the dominating error source. For a 0.1 mm thick sample this means that an error of

$\pm 5 \mu\text{m}$ can be tolerated, compared to 0.05 mm for a 1 mm thick sample. The latter measurement accuracy can be obtained using an ordinary pair of callipers, thus favouring the use of thicker samples.

6.3.3 Double integrating sphere arrangement combined with a narrow-beam set-up

The possibility of performing narrow-beam measurements on optically thick samples under previously mentioned premises, has motivated the incorporation of a narrow-beam arrangement within the integrating sphere set-up. This is realised by allowing the collimated part of the transmitted light to escape through the rear exit port of the sphere when measuring the transmittance, now the diffuse transmittance rather than the total.^{62,76,77,81,156} A double integrating sphere set up, incorporated with a narrow-beam assembly, provides an elegant technique of simultaneously monitoring *changes* of all three optical properties. This technique was consequently chosen when heat-induced changes in the optical properties of blood were studied as a function of slowly increased temperature, as presented in Paper IV. Unfortunately, the narrow-beam measurement had to be excluded when the changes in the optical properties during pulsed heating were studied in Paper III, since it was not possible to collimate the beam enough from the pulsed laser used.

However, it cannot be ignored that the unique information provided by the simultaneous monitoring of the three optical properties, enabling analysis of dynamic phenomena, must be paid with less accuracy, compared to with that for the measurements performed without the narrow-beam measurement. It therefore follows that relative rather than absolute measurements are the primary scope of a double-sphere set-up when combined with a narrow-beam arrangement. One reason is that the derivation of absolute values with high accuracy requires elaborate compensation procedures, associated with larger uncertainty in the results.¹⁵⁰ Another reason is that the correction model used does not fully account for the light losses in the exit port of the sphere, when the transmitted light is collected. This occurs when Lambertian light distribution is assumed,^{149,150} due to the forwardly directed nature of light propagation in tissue, especially for blood, as previously discussed. Even more serious is the interference of the escaping light, not only originating from the sample but also from the sphere, with the narrow-beam measurements. This can be shown by comparing results from narrow-beam

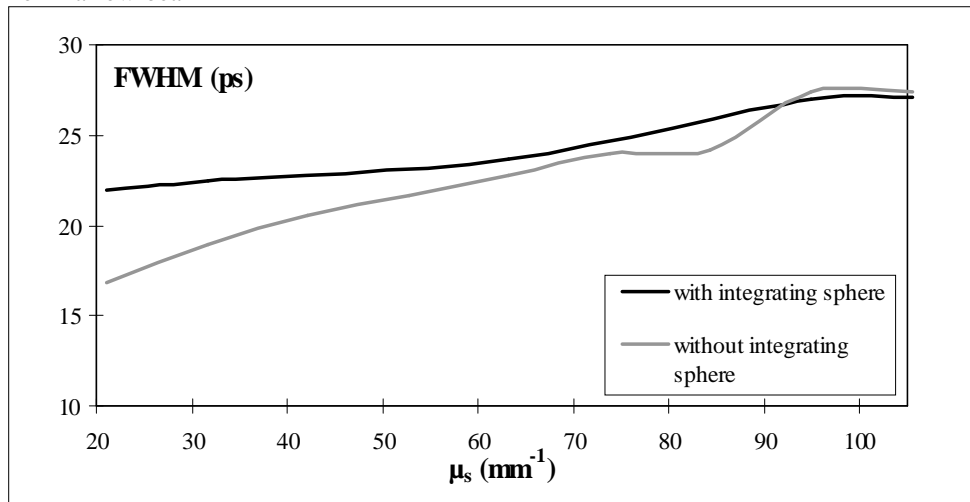


Figure 6.4 The FWHM of an initially 14 ps long pulse, propagating through a 1 mm thick suspension of polystyrene spheres versus the scattering coefficient of the sample.

measurements performed with unmounted and mounted samples on an integrating sphere. In order to better estimate the influence of unwanted scattered light on the measurements of collimated transmitted light, time-resolved measurements were performed. Pulsed light from an argon-ion-laser pumped Ti:sapphire laser was used, set at a repetition rate of 76 MHz and with a wavelength of 792 nm. The light passing through a 1 mm thick sample (total thickness: 3 mm including two surrounding glass plates) was detected by a streak camera with a slit width of 20 μm at a distance of approximately 40 cm, together with a reference pulse with a Full Width Half Maximum (FWHM) of 14 ps. The samples were polystyrene sphere (diameter=1 μm) suspensions of various concentrations in water. These were used in order to vary the scattering coefficient. Ideally, the broadening of the pulse with increasing scattering coefficient should be the same for measurements carried out, both without the integrating sphere and when the sample is mounted on the sphere. However, this was not the case, as shown in Figure 6.4. The expected broadening of the pulse is observed for both measurement series with larger scattering coefficients due to the increased optical thickness. However, a substantial broadening is already observed at lower scattering coefficients, when the sample is mounted on the sphere in contrast to when the narrow-beam set-up is used without the integrating sphere. This indicates that there is a significant influence of the scattering from the sphere on the narrow-beam measurement, despite the small detection angle used. When performing three parameter measurements with a narrow-beam set-up incorporated in the double integrating sphere, one should be aware of this and study changes in the optical properties, as performed in Paper IV, rather than absolute values. Hence, when static phenomena are studied, it is advisable to do the narrow-beam measurement separately from the integrating sphere set up in order to gain better accuracy. Since the sphere measurements result in transmittance and reflectance data of good accuracy, as long as a compensation algorithm and/or calibration routine is used, the accuracy of the three derived optical properties is to a large extent determined by the narrow-beam measurement. Pickering *et al.*¹⁵⁰ have estimated that an error of the derived optical properties in the order of 5% can be achieved, when using a double integrating sphere set-up combined with a narrow-beam measurement and IAD-computations.

7. Microscopic features of tissue and their relationship to the optical properties

The optical parameters, used to describe light transport in tissue, translate averaged physiological and morphological microscopic properties of tissue into the language of optics. Consequently, we can interpret the information given by the measured optical properties in terms of the underlying morphological and physiological state of a tissue in an averaged sense. This is an interesting aspect, since the insight gained can in turn be used to assess the state of health and condition related to both functional and structural modifications of tissues. Disorders are often accompanied by an altered cell metabolism, changes in normal composition of solutes and biomolecules, modified DNA and mitochondrial content of the cells, alterations in the shape of cells and organelles, as well as by changes in entire tissue structures due to fibrosis and incorporation of extraneous biomolecules, etc.. These alterations have a characteristic and varied impact on the tissue absorption and scattering properties. Thus, basic knowledge of the microscopic features underlying the macroscopic optical properties is of great advantage in tissue optics.

7.1 Microscopic features and light absorption

Light absorption at molecular level is perhaps a process where light exhibits its particle characteristics most directly. When a photon impinges on a molecule in the ground state, with an excited state of precisely corresponding energy to that of the photon, then its energy can be resonantly transferred to the absorbing molecule. The excited state could be an electronic level, whose characteristic energy is determined by the atomic and electron configurations in the molecule. It could also be vibrational or rotational levels, where the energy is mainly determined by the three-dimensional positions of the atomic assembly, and its quantised vibrational/rotational characteristics. Molecules are not long lived in their excited states and the absorbed light energy can be transferred to: fluorescence photons, heat, phosphorescence, or neighbouring molecules possibly inducing chemical reactions. The different de-activation paths are schematically depicted by energy level diagrams in Figure 7.1. In a wider perspective, the light absorption essentially depends on the type of absorbing molecules (also referred to as chromophores), on their internal configuration, as well as on their concentration and geometrical distribution within the tissue. These parameters will be discussed and exemplified in this section, starting with a survey of important absorbing molecules in tissue.

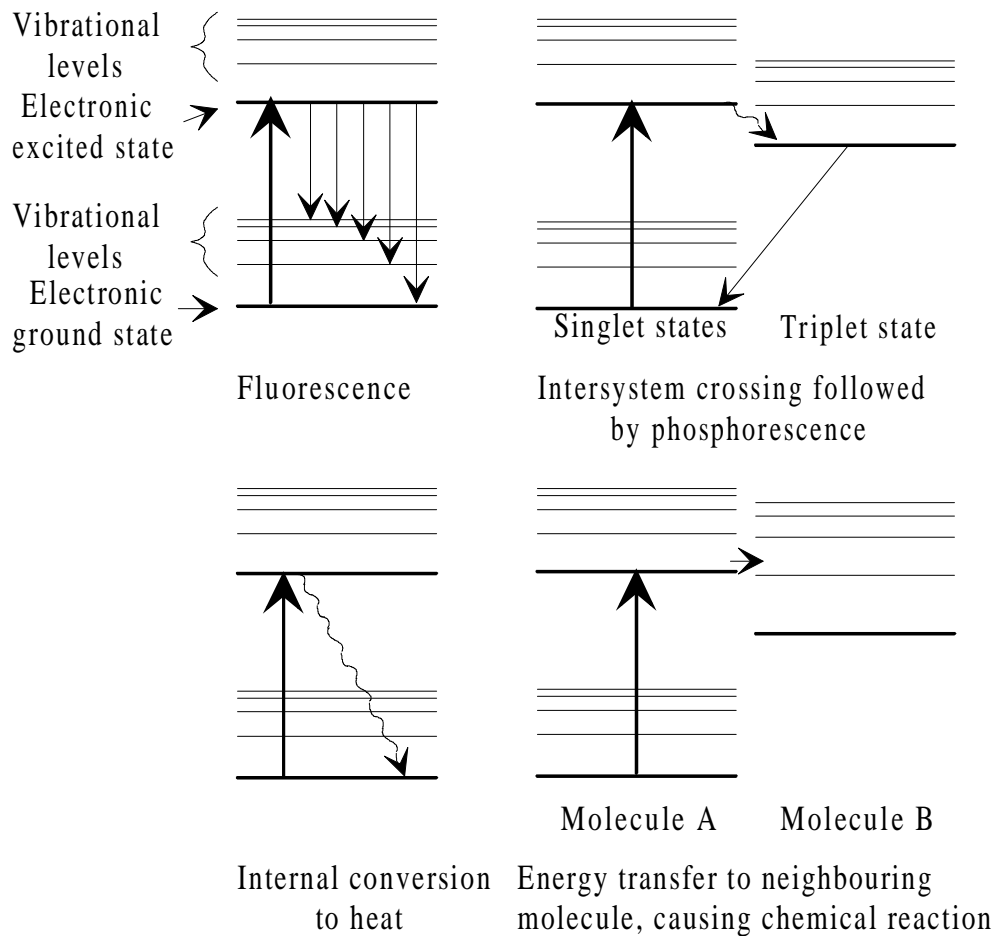


Figure 7.1 Possible pathways following light absorption are schematically represented by energy level diagrams.

7.1.1 Light absorbing molecules in tissue

Typical absorbing molecules in tissue, which require high photon energies for excitation, are DNA, proteins, and water. Due to the high concentration of these molecules in tissue, light in the *ultra violet* (UV) spectral region with wavelengths lower than 400 nm are strongly absorbed. The penetration depth, defined as $[\mu_a + (1-g)\mu_s]^{-1}$ based on the diffusion approximation, is estimated to be in the order of 10-100 μm ,³⁵ which is comparable to the lateral extension of a red blood cell (7.82 μm)¹²⁶ and to the thickness of epidermis (100 μm).¹⁵⁷

Far greater light penetration, in the order of 0.2-1 mm,³⁵ is obtained when increasing the wavelength to the *visible* range (400-700 nm). The main absorbers

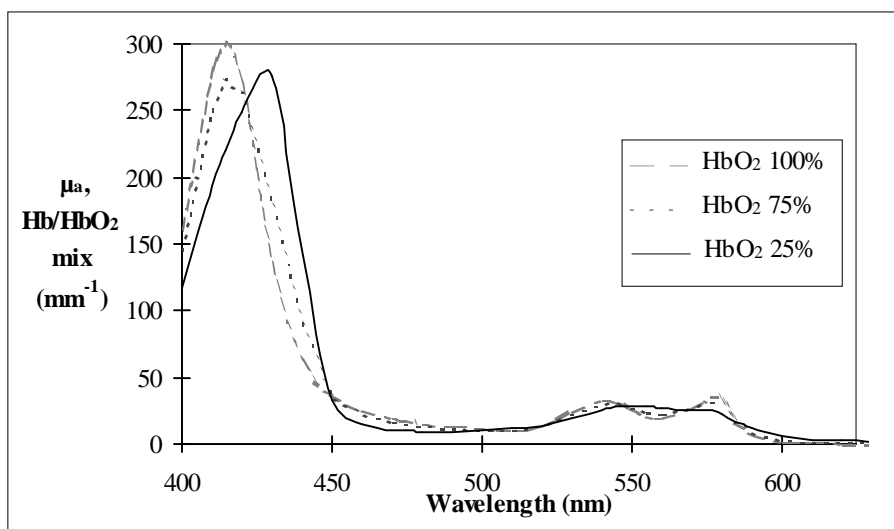


Figure 7.2 The absorption coefficient of different mixtures of oxy- and deoxy-haemoglobin, at a concentration typical for blood, versus the wavelength (data obtained from Verkrusse¹⁵⁸ and Wray et al.¹⁵⁹).

here are organometallic molecules, *i.e.* proteins with a prosthetic group containing a metallic atom. Examples of organometallic molecules are cytochromes in for instance the mitochondria, haemoglobins in the red blood cells, and myoglobin in muscle tissue. Other characteristic chromophores important in the visible spectral range are melanin in the epidermis, the two degradation products of haemoglobin: bilirubin and haemosiderin, and carotenes in fatty tissue. A high correlation at visible wavelengths has been found for the haemoglobin/myoglobin, as well as mitochondrial content in tissue with its absorption coefficient.^{113,120} For instance, the absorption coefficient of white adipose tissue (fat) and mammary adenocarcinoma (tumour tissue) can be attributed entirely to the haemoglobin content.¹²⁰ Moreover, 50% of the absorption in blood-free liver tissue, of cells with high mitochondrial content (22% of the total cell volume), can be attributed to the mitochondrial cytochrome oxidase, and the remaining 50% to haemoglobin.¹¹³ These measurements were performed at 780 nm, where the absorption coefficient of haemoglobin is comparatively weak (approximately 0.6 mm^{-1} for a haemoglobin concentration of 8.4 mM, typical in blood). The total predominance of haemoglobin absorption on the absorption coefficients of tissue for shorter wavelengths is indicated by the absorption spectra shown in Figure 7.2. However, since tissue includes only a small volume fraction of blood, the general light absorption in the visible spectral region is still clearly weaker than that in the UV region.

The average tissue absorption continues to decrease in the *near infrared* (NIR) region (the spectral range of approximately 700-2500 nm) and the light penetration

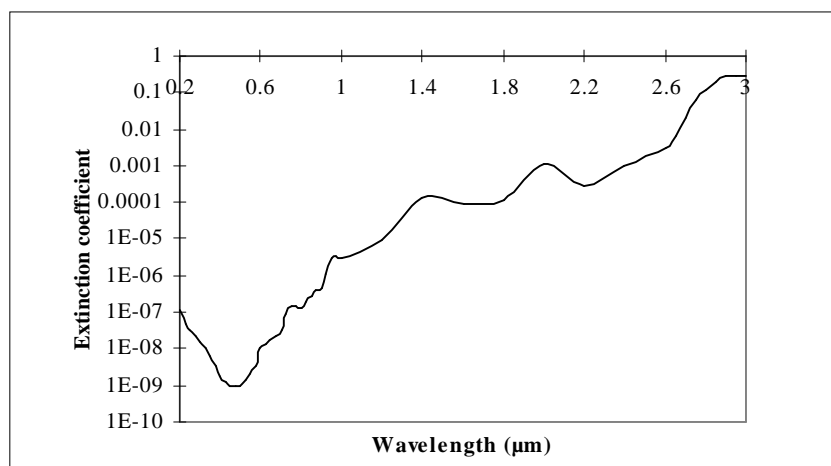


Figure 7.3 A water absorption spectrum is shown on a logarithmic scale in terms of the extinction coefficient (proportional to the absorption coefficient). Data is obtained from Hale and Querry¹⁶⁵.

consequently increases, with a maximum of one to a few millimetres³⁵ in a wavelength range of 700-1300 nm, called the tissue optical window. At longer wavelengths, the absorption rapidly increases again, mainly due to combinational vibrational overtone transitions of the water molecules. The most prominent water absorption bands can be found at 0.76, 0.97, 1.19, 1.45 and 1.94 μm .¹⁶⁰ The section 1.0-2.5 μm of the NIR region also contains characteristic but weak combinational and overtone vibrational bands for O-H, C-H and N-H bonds generally present in most biomolecules. Typical transmission and reflection spectra of cholesterol, collagen and elastin, showing interesting spectral features, are presented in Paper VII. Furthermore, with a rigorous calibration routine, the weak spectral information in this wavelength region can be extracted to determine cholesterol,¹⁶¹ albumin, globulin and urea¹⁶² concentrations in human serum. The wavelength segment 2.0-2.3 μm has been shown to contain particularly useful information,¹⁶² for instance for the characterisation of cardiovascular tissue as described in Paper VII. Fortunately, the light penetration depth in tissue is quite large (approximately 300-400 μm)³⁵ due to a dip in the absorption coefficient of water in this wavelength segment, compared to that at slightly shorter and longer wavelengths in the NIR region (150 μm at $\lambda=2.0$ μm).³⁵

At even longer wavelengths, the *mid-IR* range (2.5-10 μm), the absorption characteristics are not only dominated by the strong water absorption, but also by distinct absorption bands originating from numerous first-order vibration/rotation modes of the biomolecules. Absorption spectroscopy in this wavelength range, has thus become a standardised instrument for biochemical analysis of tissue samples.¹⁶³ For instance, glucose shows numerous spectral fingerprints between

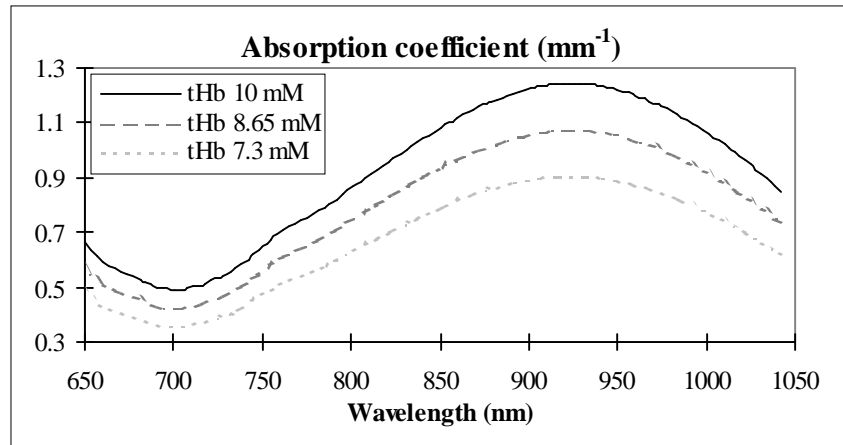


Figure 7.4 Absorption spectra of blood with different concentrations of oxy-haemoglobin (data obtained from Wray et al.¹⁵⁹).

2.5-11 μm .¹⁶⁴ However, since conventional optical fibres do not transmit light efficiently in this spectral range and tissue exhibits extremely low light penetration depths (1-20 μm),³⁵ mid-IR spectroscopy is not therefore a realistic option for *in vivo* measurements in the clinics.

The presence of chromophores are crucial for tissue to absorb light, as is the relative concentration of each absorber. The general spectral shape of the overall absorption coefficient of tissue is essentially determined by the strong absorption characteristics of water, in both the UV and IR regions as shown in Figure 7.3. This is not unexpected, since the water content of tissue can be as high as 57% by weight.¹⁶⁶ Whole blood, normally containing 7.5-9.8 mM haemoglobin, has a significantly higher absorption coefficient in the visible wavelength region than water. It is also the main absorber of visible light in tissue in general, but not as dominating as one could believe from Figure 7.2, which shows a peak value of the absorption coefficient of several hundreds of inverse millimetres. One must keep in mind that the blood concentration in tissue is only in the range of 1-5% of the total volume.

Changes in the absorber concentration and the absorption coefficient are linearly related. An increase in the absorber concentration can therefore be monitored by an increase in the characteristic absorption bands. This is illustrated in Figure 7.4, where the absorption behaviour of three concentrations of oxyhaemoglobin, close to the normal range of whole blood, are presented. Despite small relative changes in the absorber concentration, they are often clearly apparent in optical transmission measurement due to the exponential relationship between the collimated transmission and the absorption coefficient (Beer-Lambert's law Eq. 4.24). This provides a sensitive tool not only for qualitative but also

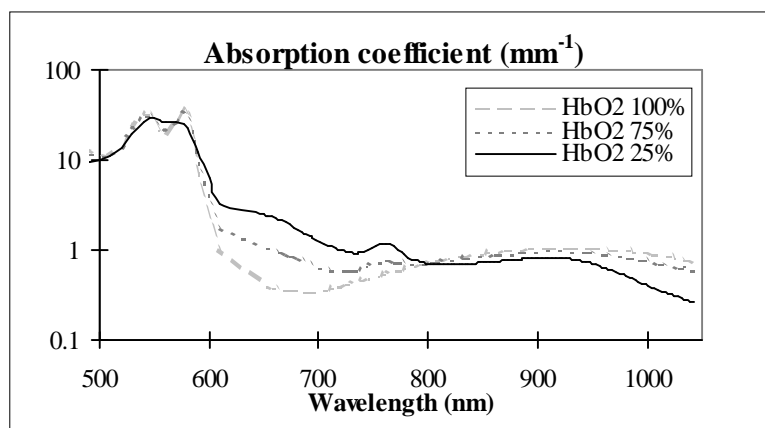


Figure 7.5 Absorption spectra of haemoglobin with different degrees of oxygenation (data obtained from Verkruyse¹⁵⁸ and Wray et al.¹⁵⁹).

quantitative analysis of distinctive absorbers in tissue, which can be used for characterisation. For instance, the weak vibration absorption bands of cholesterol, collagen and elastin in the NIR spectral range can be used for characterisation of cardiovascular tissue based on transmission or reflection measurements, as shown in Paper VII.

7.1.2 Configurational factors influencing the absorption coefficient

From the previous section we can conclude that the absorption coefficient of tissue is highly dependent on the wavelength, yielding a spectral shape governed by the tissue constituents and their concentrations. However, there are additional factors influencing the absorption coefficient.

Small configurational changes in the absorbing molecules have a strong impact on the absorption coefficient. This can be induced by for instance changes in temperature and in the tissue osmotic balance, the latter being governed by various solutes. Another example of conformational changes is when an oxygen molecule is bound to the haemoglobin molecule to form oxyhaemoglobin. It affects the entire three-dimensional structure of the haemoglobin molecule, inducing decreased absorption probability at particular photon energies (*i.e.* wavelengths) and increased at others. These changes are clearly shown in Figure 7.2 and Figure 7.5 for different concentrations of oxy- and deoxyhaemoglobin. The maximum in the absorption peak of deoxyhaemoglobin is shifted to shorter wavelengths (to 418 nm) on being oxygenated and two peaks (at 542 and 577 nm) are formed from the single absorption peak at approximately 560 nm (see Figure 7.2 and Figure 7.5). Furthermore, the peak centred at approximately 758 nm, originating from deoxyhaemoglobin, is reduced at higher concentrations of oxyhaemoglobin, as can be seen in Figure 7.5.

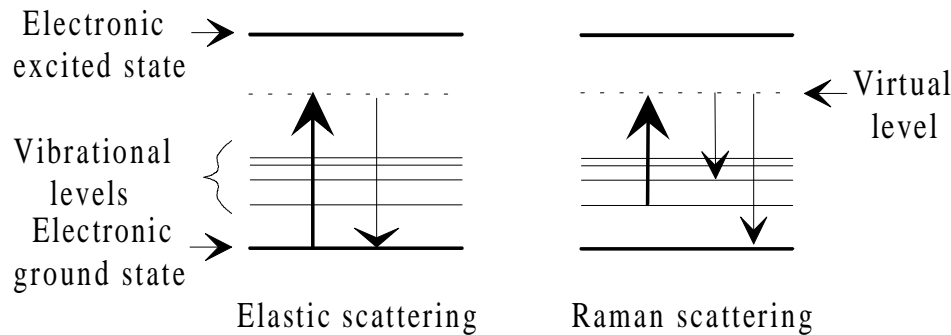


Figure 7.6 The two important pathways of light scattering (elastic and Raman) are depicted here schematically as energy level diagrams.

Finally, the geometrical distribution of the absorbers in tissue influences the effective absorption coefficient. A homogeneous distribution of the absorber results in a higher *effective* absorption coefficient compared to when the absorbing molecules are enclosed within discrete volume elements, due to shielding. When enclosed, only the outermost absorbing molecules of each element are apparent to the light, whereas the innermost absorbers are shielded by the surroundings. This means that only a fraction of the absorbing molecules are active, yielding a lower effective light absorption. Verkrusye *et al.*⁸⁷ have for instance shown that this phenomenon is significant in relation to the distribution of haemoglobin as absorber in different vessel geometries. A homogeneous distribution of a certain concentration of haemoglobin yields higher effective light absorption than when the same quantity is enclosed within vessels.

7.2 Microscopic features and light scattering

The photon characteristics of light can also be applied to light scattering. The important elastic and Raman scattering phenomena are represented by energy level diagrams in Figure 7.6. The scattering event is then treated on molecular level. This can be depicted as an excitation process followed by a prompt de-excitation to either the initial state of the molecule (elastic scattering) or to a higher/lower laying level causing a net change in the potential energy of the molecule (Raman scattering). When the electromagnetic wave model of light is used, light scattering is instead treated as a phenomenon originating from spatial variations in the moderately wavelength dependent refractive index. This is perceived at various size levels, ranging from boundaries of organs, layers with different types of cells or structural components, to sub-cellular constituents, such as the cell membrane, organelles, cytoplasm, and the extracellular fluid, as illustrated in Figure 7.7.

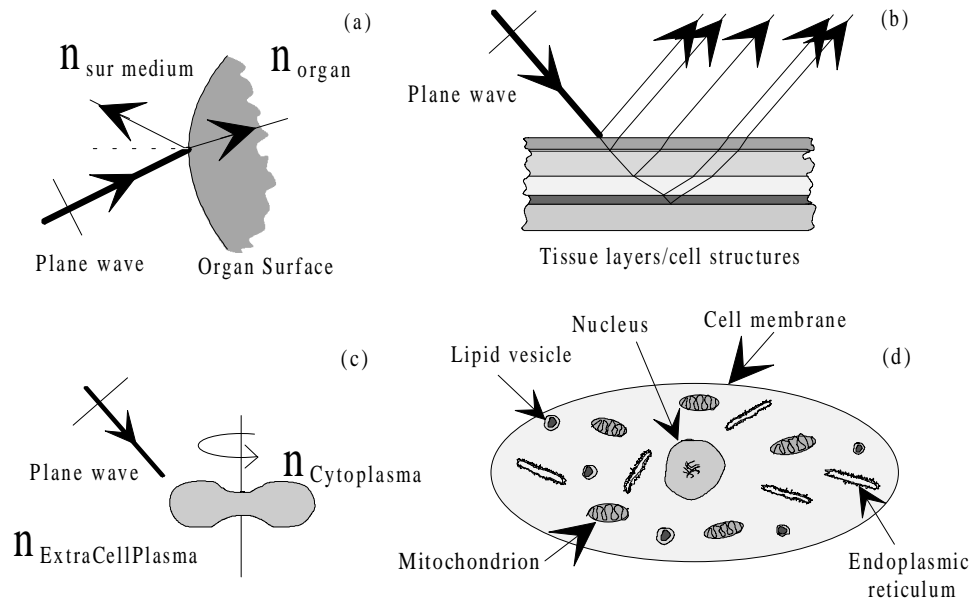


Figure 7.7 Different contributors to the light scattering in tissue, from (a) Fresnel reflection in macroscopic organ boundaries and (b) tissue layers/cell structures to microscopic (c) cellular and (d) sub-cellular components, are illustrated.

Important parameters are for instance the average shape and size of the scattering objects relative to the wavelength. Radiative transport theory is too unprecise a tool to theoretically investigate and interpret light scattering from microscopic tissue components. Instead, fundamental electromagnetic theory is almost exclusively used to provide detailed information on the influence of microstructural parameters of the scattering object on the resultant scattering characteristics.

7.2.1 Light scattering structures in tissue

Fresnel reflection at a surface of an organ, as illustrated in Figure 7.7a, can be thought of as a macroscopic scattering which is dependent on the direction of the incoming light relative to the normal of the tissue surface, as well as on the refractive indices of both the surrounding medium and the organ tissue. The refractive indices of a number of tissues have been measured and found to range from 1.38 to 1.41 at 632.8 nm. A slight dispersion (*i.e.* dependence of the wavelength) is indicated by the decrease in the refractive index over the wavelength range 390-710 nm of the order of 2-4%.¹⁶⁷

Refractive indices of this order of magnitude result, at small to intermediate incidence angles, in a Fresnel reflection in the order of a few of percent for an air-tissue interface and less than one percent for a water-tissue interface. It is thus a scattering phenomenon of apparently low significance. However, with several adjacent tissue/cell layers, or repeated structures with slightly different refractive indices within the organ as depicted in Figure 7.7b, the total effect can be considerable.

Variations in refractive index over a smaller scale than that of organs and tissue layers, can also be shown to influence the light propagation within tissue. The small differences in effective refractive indices of the extracellular fluid and entire cells, when the cells are seen as homogeneous particles, have a larger collective impact on the light scattering than that indicated by the magnitudes of the relative refractive indices. This scattering behaviour is illustrated in Figure 7.7c. The ratios of the cellular and extracellular refractive indices are close to unity, for example 1.045 for a red blood cell in blood plasma. There is however significant scattering due to the large number of cells. Important features influencing this ratio are low-molecular solutes, such as electrolytes, alcohols and also glucose, fructose and other sugars. Kohl *et al.*^{10,12} have shown that the presence of glucose in an aqueous suspension of polystyrene spheres, increases the *total* refractive index of the suspension with increasing concentration of glucose, resulting in a decrease in the *relative* refractive index. This results in a decrease in the scattering coefficient and an increase in the g-factor, which was confirmed by Mie theory computations^{10,12,168}. Chance *et al.*¹⁶⁹ have shown a corresponding decrease in the effective scattering coefficient for different kinds of sugars (including glucose), electrolytes and alcohols in lipid vesicle- (Intralipid) and cell-suspensions, as well as in liver tissue.

The cell mainly contains an aqueous solution of electrolytes and proteins, the cytoplasm, with an effective refractive index of approximately 1.38,⁹⁶ while the cell membrane and cell organelles are composed of phospholipid layers and proteins with refractive indices in the range of 1.43-1.51.^{96,114} However, since the fraction of these higher refractive index components is rather small, *i.e.* in the order of 5%,⁹⁶ the effective cellular refractive index can be estimated to approximately 1.40.⁹⁶ When studying the spatial variations in the refractive index over a microscopic scale such as the inside of a cell using a phase microscope, it is found that the cell membrane and the nucleus are the components which are the dominant contributions to the cellular effective refractive index;⁹⁶ these are far more important than for example the mitochondria. However, this does not mean that the membrane and the nucleus are the main scatterers in tissue. Apart from the refractive index, parameters such as structure, size and concentration of the scattering object must also be taken into account. For instance, the cell membrane has a thickness of only 5-10 nm and thus has a relatively insignificant effect on the total light scattering from the cell,^{110,111} despite its high refractive index. Instead, a high correlation between the reduced scattering coefficient and the mitochondrial content has been found.¹²⁰ Tissues of high mitochondrial content exhibit high μ_s' -coefficients. Light scattering from tissues with high concentrations of

Table 7.1 Cell components and their corresponding properties of importance for the evaluation of light scattering, as well as their individual contribution to the total cellular light scattering.

| Cell component | Refractive index | Size | Concentration | Membrane structure | Scattering efficiency | References |
|----------------|------------------|-------|---------------|--------------------|-----------------------|------------|
| Membrane | high | thin | low | low | low | 96,110,111 |
| Nucleus | high | large | low | low | low | 96,120 |
| Mito-chondrion | low | small | high | high | high | 96,113,120 |

| | | | | | | |
|-------------------------------|------|-------|----------------------|-----------|---------------------|--------------------|
| Lipid vesicle | high | small | high in fatty tissue | low | high (when present) | ^{120,121} |
| Endo-plasmic reticulum | low | small | depends on cell type | very high | ? | ⁹⁶ |

mitochondria, such as liver tissue, can to a large extent (but far from completely) be attributed to this organelle, despite its low refractive index. This can be mainly attributed to the large volume fraction (22%) in the hepatocyte,^{113,120} but possibly also to its internal structure with a high (20-40%) membrane content which facilitates light scattering.⁹⁶ A layered structure is, as previously discussed, a more efficient scatterer than a corresponding homogeneous object. When the internal structure of a scattering object is less homogeneous, it causes increased large-angle scattering and decreased small-angle scattering.^{108,170} This argument can, beside the low particle concentration, also partly explain the low effective scattering of the nucleus. Despite its high refractive index, a low correlation between the reduced scattering coefficient and the tissue DNA content is found.¹²⁰ The low volume fraction of membrane structures in the nucleus (0.2-0.7%)⁹⁶ is probably an explanation for this. Thus, it would be interesting to investigate the contribution to the cellular light scattering by the organelle endoplasmic reticulum, as the volume fraction is as high as 50-60%.⁹⁶ Moreover, lipid droplets inside the cells of adipose tissue (fatty tissue) have been shown to be a major contributor to the cellular scattering, due to their high refractive index and high volume fraction (88%) in the cell.¹²⁰ The strong scattering characteristics of lipid particles is further confirmed by the high correlation found between the lipid content of liver tissue and the reduced scattering coefficient,¹²¹ when the influence of the mitochondrial content has been compensated for. However, these measurements were performed *in vitro*. This is important to note, since the lipid droplets solidify, affecting the scattering properties, when the tissue temperature is reduced from normal to for instance room temperature. Results from time-resolved measurements performed by Berg⁵¹ on fatty porcine tissue indicate an increase in the reduced scattering coefficient when the tissue temperature was lowered from 37°C to 15°C. A summary of the contributions of the different cell components to the cellular light scattering discussed above is presented in Table 7.1. In addition, Rayleigh scattering from macromolecules, such as haemoglobin and albumin, suspended in the extracellular fluid and/or the cytoplasm contribute to the scattering behaviour.¹¹⁷

7.2.2 Configurational factors influencing the scattering properties

Configurational alterations in cell clusters, cells, organelles and macromolecules have a significant impact on the scattering properties of tissue. It can be induced by various changes in normal physiological parameters, such as temperature, local concentration of electrolytes, oxygenation saturation, etc., as can be observed as a consequence of for instance disorders in the tissue, treatment response and tissue deterioration *post mortem*. This is discussed further in Chapters 8 and 9. In order to improve the understanding of the effect of these configurational alterations on the scattering properties, theoretical studies should be helpful.

Detailed theoretical information on the light scattering from specific cells and their organelles can be obtained by utilising the various methods based on electromagnetic theory, as described in Chapter 4.3. For instance, the red blood cell (RBC) is often modelled as a homogeneous sphere employing Mie theory computations.⁹ Despite the discrepancy between actual and modelled cell shapes, the theoretical results show good agreement with experimental results from diluted blood samples, probably owing to the random orientation of the cells in the non-flowing samples, used for the measurements. The assumption of a homogeneous cell is also satisfactory, since the red blood cell is composed of a cell membrane and a cytoplasm containing haemoglobin molecules but basically no organelles. The cell membrane has, as discussed above, a minor influence on the light scattering. It is thus reasonable to incorporate its contributions via the effective refractive index of the entire cell, which again is confirmed by the good correspondence between Mie theoretical and experimental results.⁹

Mie computations can also be employed in order to investigate the influence of the *size* of the scattering object, as well as of particle volume changes on the light scattering.^{108,109} The general results from such computations show that small scatterers, compared to the wavelength, yield essentially isotropic scattering, whereas particles of greater size, the scattering is of a more pronounced anisotropic character. This has also been confirmed by experimental results from measurements on red blood cells.¹⁷¹ Moreover, the scattering cross section increases with particle volume. Increased cell size, which occurs due to for instance osmosis, thus increases the forward scattering and also the scattering probability. From these computations it is clear that the anisotropy factor, g , is strongly dependent on the average size of the main scatterer in the tissue and can in fact be used to derive a so called Mie equivalent average radius from measured g -factors, as was shown in Paper II utilising a spherical-particle model. For instance, the measured g -factor of blood is close to unity in the visible wavelength range (approximately 0.99) and corresponds to a large scattering object with a size comparable to the red blood cell. Thus, the main scatterer in blood is the entire red blood cell. Performing the same estimates from measured g -factors of liver tissue, reveals a scattering particle with a Mie equivalent average radius comparable to a mitochondrion (see Paper II). This corresponds closely with the high mitochondrial content in liver tissue and its dominating influence on the scattering properties,^{113,120} as discussed previously. Mie computations utilising a cylindrical-particle model can also be applied, in order to investigate the influence of the size of an elongated scattering object such as collagen fibres, a structural intercellular substance in skin, on the light scattering.⁷⁹ Correspondingly, thin (compared to the wavelength) fibres yield scattering with isotropic character, whereas an enlargement, as observed for example with the gestational maturity of collagen fibres in neonatal skin, increases the anisotropy and the scattering cross section. This has also been confirmed for cylindrical organelles in retinal nerve fibres.¹¹⁴


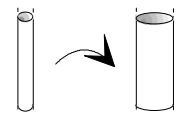




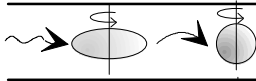
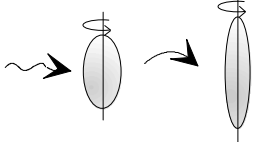
Although the contributions to the total cellular scattering from the nucleus are relatively small, changes in its size and refractive index influences the angular distribution of the scattered light. Rayleigh-Gans-Debye (RGD) computations of a layered sphere model, with a particle size in the order of a lymphocyte, reveals that an increased nucleus diameter, at constant total cell size, increases the forward scattering. This is confirmed by results obtained from Finite-Difference Time-Domain (FDTD) computations.¹⁷⁰ However, a decrease in refractive index of either the nucleus, or the surrounding cytoplasm causes a decrease in the forward scattering.¹⁷² This provides the means to extract information on

nuclear size and shape by measurements of the scattering distribution,¹⁷³ which is of importance in conjunction with for example cancer detection.

Changes in *shape* of the scattering object also influences the angular distribution of the scattering. This was evaluated in Paper V by performing T-matrix computations utilising a spheroidal model with a particle volume equal to that of a red blood cell. In general, particles with pronounced aspherical shape, exhibit asymmetric scattering, resulting in for example an elliptical angular scattering distribution, as confirmed experimentally by Burger *et al.*¹⁷³ The transformation of a disc shaped into a spherical cell, as well as the elongation of prolate shaped cells were shown in Paper V to, on average, decrease the anisotropy at constant cell volume. The former small but distinct decrease in the g-factor found when the disc shaped red blood cells become spherical heating, see Paper IV. A summary of the morphological changes discussed here are presented in Table 7.2.

This survey indicates that the light scattering from individual cells is highly dependent on the cell morphology and that electromagnetic theory provides useful computational instruments to investigate this dependence in detail. Elaborate

Table 7.2 Common changes in cell morphology and their impact on the anisotropy and scattering efficiency of the cellular light scattering

| Shape transformation | Anisotropy factor | Scattering cross section | Computation method |
|---|-------------------|--|--|
|  | increase | increase | Mie ^{9,108,109} |
|  | increase | increase | Mie, ⁷⁹ RGD ¹¹⁴ |
|  | decrease | dependent on the relationship between the internal structure and the total particle shape/size | Modified anomalous diffraction, ¹⁰⁸ FDTD ¹⁷⁰ |
|  | increase | not evaluated | Modified RGD, ¹⁷² FDTD ¹⁷⁰ |
|  | decrease | not evaluated | Modified RGD ¹⁷² |
|  | decrease | not evaluated | Modified RGD ¹⁷² |
|  | decrease | decrease | T-matrix (Paper V) |
|  | decrease | decrease | T-matrix (Paper V) |

studies on the angular distribution of the scattering,^{26,31} as described in Paper V, often reveal significant discrepancies compared to the Henyey-Greenstein (H-G) phase function, normally used to describe the angular distribution of a single scattering event in transport theory. The H-G function exhibits larger side and back scattering at high g-factors, than given by scattering computations based on electromagnetic theory for the same value of the g-factor. Whether this disagreement is due to erroneous assumptions made in the electromagnetic theory model used, or to the empirical character of the H-G function, remains uncertain. It could be that the "single scattering" event described by the H-G function corresponds to the integral scattering from more than one cell, or to the scattering from one cell, including collective effects from the closely surrounding cells. The average distance between two "single scattering" events for tissue is typically in

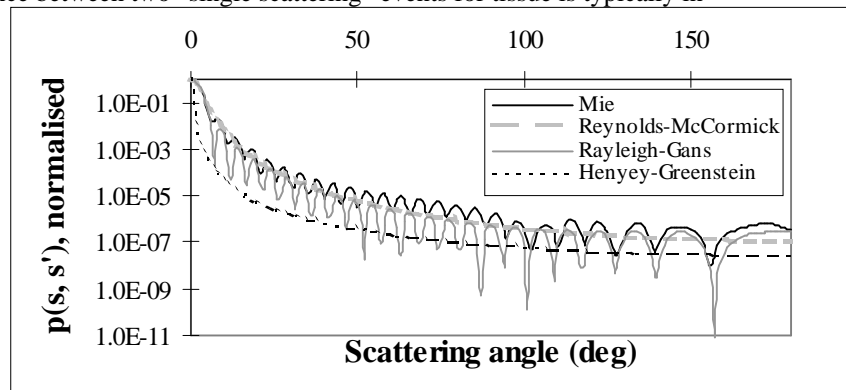


Figure 7.8 Four different phase functions, normalised at 0° , are displayed versus the scattering angle. The Mie and Rayleigh-Gans phase functions were obtained from computations utilising the subroutines written by Bohren and Huffman⁹⁴ and an analytical expression¹⁷⁴ for a volume equivalent sphere of a red blood cell (RBC) at 632.8 nm. The Henyey-Greenstein phase function was computed for the g-factor 0.9939, corresponding to the angular distribution derived from the Mie computations. Finally, a simple fit of the Reynolds-McCormick phase function to the Mie phase function resulted in a g-factor of 0.94 and an α of 1.3.

the order of 25-60 μm , which indicates an integral scattering from several cells, organelles and structural components. The Henyey-Greenstein function has experimentally been shown to describe the light scattering in dermis well (to 90%)¹⁸ and it has subsequently been used for almost all types of tissues. However, its appropriateness to describe the highly anisotropic light scattering characterised by extremely high g-factors, as for example in blood, has been discussed. Other phase functions have instead been applied, such as Rayleigh-Gans and Reynolds-McCormick phase functions (the latter dependent on two parameters, g and α), which have been found to be more compatible with experimental results.^{26,28,30,31} A comparison between four different phase functions, all computed for light scattering by a sphere with the same volume as a red blood cell, is shown in Figure 7.8. It reveals a significant discrepancy between the Henyey-Greenstein and Mie phase functions. The Rayleigh-Gans and Reynolds-McCormick phase functions correspond better with the Mie phase function and might thus be a more appropriate choice for computations of light scattering by blood. This is important to bear in mind, since the choice of phase function has

been proven to have a large impact on for example Monte Carlo simulated results, especially close to the source.^{25,28}

The theoretically derived asymmetric scattering from cells with a highly aspherical shape, can often be neglected when modelling light scattering in tissue, since this effect is often averaged in practice by the random orientation of the cells. However, the assumption of isotropic azimuthal light scattering (with constant scattering probability over the azimuthal angle $\psi = 2\pi\xi$, where ξ is randomised number, see Eq. 4.41) in tissue might not be appropriate for structurally aligned cells in tissue such as muscle tissue.²² For instance, measurements performed on flowing blood, which induces cell alignment due to the shear stress, have clearly shown asymmetric back scattering.¹⁷⁵

8. Laser-based treatment modalities - tissue optical aspects

The primary cause of a treatment modality employing laser light, is the transformation of light energy into heat or chemical energy, via light absorbing endo- or exogenous chromophores. An essential variable governing a successful outcome of the treatment is therefore the distribution of these efficient absorbers. They correspond to an active part of the optical absorption coefficient. In addition, the distribution of the radiation is an equally essential factor, governed not only by the absorption of the molecules active in the treatment, but also by other chromophores, as well as by the scattering of the tissue. The treatment should of course finally destroy the diseased tissue. The treatment affects the tissue and consequently modifies its optical properties, which in turn alters the distribution of the light. It is thus clear that treatment modalities utilising laser light are characterised by a complex dynamic behaviour. Changes in the optical parameters have been estimated in connection with clinical laser treatment modalities, such as photodynamic therapy (PDT) and thermotherapy with both long and short time constants, as presented in Paper I to Paper IV.

8.1 Photodynamic therapy

8.1.1 *The distribution of the photoactive drug*

Photodynamic therapy (PDT) is a treatment modality primarily applied to cancers. It is based on the photochemical interaction effect and can be thought of as a light activated chemotherapy. A photosensitive compound (for instance Photofrin) or pro-drug (for instance δ -amino laevulinic acid - ALA) is administered to the patient, either systemically or topically. Their photoactive agents, protoporphyrin IX (PpIX) for ALA and porphyrin derivatives for Photofrin, are to some extent selectively accumulated into malignant tissue, thus preparing the ground for selective tumour treatment. The selectivity for topically applied ALA is primarily because it readily passes through only an abnormal epithelium,¹⁷⁶ and for systemic administrated ALA and Photofrin presumably owing to characteristic properties of tumour tissue, such as low pH due to high anaerobic glycolysis, the presence of specific antigens and receptors¹⁷⁷⁻¹⁷⁹ and also increased vascularisation.¹⁸⁰

The type of administration, affects the distribution of the PDT-active absorber. Topical application, for example on the skin, or intraperitoneal administration results in a superficial and local distribution¹⁸¹ and thus a correspondingly local treatment. There is then less risk of phototoxic reactions in other organs and minimal danger of perforation of the treated tissue in *e.g.* the oesophagus, bladder or uterus. In contrast, fully systemic administration (oral or intravenous) results in a wider distribution of the photosensitiser,¹⁸¹ which enables treatment of cell layers deeper within the tissue, but also induces a more general photosensitisation in other organs.

Intracellularly, the mitochondrion seems to be a common location for both these sensitisers. For instance, ALA is transformed into PpIX in the natural haem synthesis pathway

proceeding in the mitochondria, and this occurs with greater efficiency in many tumour cells.^{176,182} Moreover, the lipophilic porphyrin derivatives are preferably stored in the phospholipid bilayers of different membrane structures, primarily those in the mitochondria.^{178,183} No observations of microscopic, cellular changes originating from the photosensitiser itself have been reported, although van Hillegersberg *et al.*⁷⁶ have reported an increase in the scattering coefficient and a decrease in the g-factor following intravenous administration of Photofrin before irradiation. Changes in tissue structure or physiology were postulated, although no microscopical changes could be distinguished in histological samples. The possible influence of fluorescence from the photosensitive agents, inducing anomalous results, was also considered. The former explanation seems rather unlikely, considering that the increase obtained in the reduced scattering coefficient was approximately 30-100%, which usually corresponds to distinct alterations in the tissue morphology, as found for instance in Paper II.

8.1.2 The light distribution

No chemical reactions occur before the irradiation starts, *i.e.* the photons can be considered as reagents, where the reaction pathway is determined by the photon energy. Since there are several possible pathways, the choice of photon energy (*i.e.* the wavelength of the light) is also influenced by the optical properties of tissue. The requirements of high absorption of the photosensitiser and low absorption of endogenous chromophores must be balanced. The porphyrin-based sensitisers exhibit several stronger absorption bands in the region between 400-650 nm, these decreasing in strength at longer wavelengths. At first sight, better treatment results should be obtained if light with a wavelength around 400 nm was employed, probing the most efficient absorption band of the sensitiser. However, light at approximately 630-635 nm is normally used, employing a weaker absorption band, since the penetration depth is significantly greater at longer wavelengths in the visible wavelength region, as discussed in Chapter 7. Less efficient light absorption by the sensitiser in a larger tissue volume produces a better outcome, since the treatment light has a better chance to reach peripheral neoplastic cells, thus decreasing the risk of partial treatment and recurrence, than strong light absorption in a superficial tissue layer.

8.1.3 The photochemical reaction

When the photoactive molecules of the photosensitiser absorb red light at 630-635 nm, the photon energy is just enough to promote the molecules into the first excited singlet state, but insufficient for excitation to any higher levels. Following this first excitation path, the molecules are transferred from the excited singlet state, via intersystem crossing - a process involving a change in sign of electron spin - to the lowest triplet state, but still corresponding to a higher energy than the original ground level. The relaxation to the singlet ground state from this triplet state is an unlikely process, resulting in unusually long (in the order of 100 μ s compared to 10 ns for a singlet excited state¹⁸⁴) lifetimes for the excited molecules. This means that there is time enough to interact with surrounding molecules, predominantly with oxygen, forming highly reactive singlet oxygen.¹⁷⁷ Thus, the excitation of photoactive molecules ultimately causes an oxidation. The outcome of the treatment is consequently not only influenced by the distributions of photosensitiser and light but also relies on the presence of oxygen.

8.1.4 The treatment response

Target molecules for the oxidation are proteins, nucleic acids and phospholipids. For instance, inhibition of important enzymes (*e.g.* mitochondrial cytochrome c oxidase) by oxidation of amino acids in their active centres and conformational changes of membrane proteins have been suggested as important mechanisms for cell death by PDT.¹⁷⁷ Consequently, mitochondrial damage has consistently been observed.¹⁷⁸ Tumour cells as well as vascular endothelial cells demonstrate this damage to a greater extent and are thus more susceptible to PDT than other cell types, but not necessarily correlated with the content of sensitiser.¹⁷⁹ This means there are essentially two types of damage which can be observed following PDT. These are direct destruction of the tumour cells as well as vascular damages. The latter causes secondary injuries in terms of decreases in the quantity of nutritional substrates and oxygen reaching the tumour tissue.^{179,185} It appears as if the destruction of tumour tissue following PDT, employing systemic administration of Photofrin or ALA can be mainly attributed to damage to the microcirculation, *e.g.* oedema of vascular endothelial cells and blood stasis in the vascular lumen.¹⁸⁶⁻¹⁸⁹ This causes an immediate decrease in blood flow^{189,190} and red blood cells are then accumulated in the dilated blood vessels. In the optical properties, this is mainly reflected as an increase in the absorption coefficient, as demonstrated in Paper I. When vascular damage is reached, the treated tissue layer serves as an absorbing filter for the underlying tissue, thus reducing the treatment depth. This can be shown by the insertion of optical fibres into the tissue to different depths; these serve as dosimeters during the treatment, and monitor the decrease in light intensity with treatment time. This was described in Paper I, confirming the results obtained by others.¹⁹¹ The change in the effective absorption coefficient was found to range from 30 to 100% in a 1 mm thick superficial tissue layer.

In contrast to the above discussion, it was found that the resulting blood flow increases following PDT after topical application of ALA.¹⁹² This indicates a totally different underlying mechanism, vascular damage does not occur. An increased blood flow can be monitored employing laser-Doppler imaging, as discussed in Paper XI, not only immediately following the treatment but until normal tissue has fully replaced the malignant lesion, which can take approximately eight weeks. This indicates an inflammatory reaction, as a result of direct response to the treatment by the tumour cells. The difference in response mechanism between the two administration modalities is probably because the vascular endothelial cells are more directly exposed to the sensitiser by systemic administration, as compared to topical application, where the drug does not essentially enter the blood stream. The resulting inflammatory response in conjunction with topical administration, increases the quantity of blood cells in the tumour area both during and after the treatment. This probably also produces an increased total tissue absorption coefficient during the treatment, owing to the increasing concentration of the endogenous absorber, haemoglobin. Results obtained from dosimetry measurements during PDT, utilising topically applied ALA, confirms this hypothesis, since it was found there is a consistent steady decrease in fluence rate when 11 patients were treated.¹²⁷ However, the topical administration is often applied to superficial lesions in for instance the skin and the increased blood flow essentially takes place beneath the epidermis and the lesion. Hence, the “blood filter” does not probably significantly affect the treatment efficiency for such superficial lesions. However, it might have an impact on the treatment of nodular lesions, partly explaining the less successful outcome of ALA-PDT, compared to that found for the superficial lesions. Still, an average

penetration depth of 2.8 mm, corresponding to a distance where the fluence rate was reduced by e^{-1} based on the diffusion approximation, was measured *in vivo* during ALA-PDT.¹²⁷ A similar penetration depth, was confirmed by Monte Carlo simulations performed by Svaasand *et al.*¹⁹³ Thus, the primary problem for topical application appears to be the limited ALA penetration and diffusivity. Microscopic fluorescence studies have shown that the detection of porphyrin fluorescence in conjunction with topically applying only ALA is limited after 3 hours to a depth of 0.75 mm.¹⁸¹ Dimethylsulfoxide (DMSO) was shown to enhance the ALA penetration by a factor of three, resulting in a ALA penetration in the same order as that of the light.

It is thus clear that the outcome of the treatment is a complex function of several mutually interacting parameters. Thus, a dynamic dosimetry model is needed, from which the cytotoxic dose can be calculated, in order to estimate the optimal treatment parameters. Svaasand *et al.*¹⁹⁴ have developed such a model, including time dependent computations of the ALA distribution in the skin, and calculations on the formation of PpIX and the generation of singlet oxygen from the light distribution. Mechanisms such as drug clearance and photo bleaching of the photo active molecules were taken into account. This model would, for instance, be an excellent platform for detailed analysis of the possible impact of changing optical properties on the outcome of the treatment. This could be achieved by incorporating a dynamic relationship between the cytotoxic dose, as a measure of the tissue damage, and the optical properties.

8.2 Thermotherapy

Photosensitive agents are not necessary for all laser-based treatments. The light energy can also be absorbed by endogenous chromophores and then transformed into thermal energy. When the tissue temperature exceeds 100°C, vaporisation of the water occurs. Bubble formation follows, which causes an increase in transmittance and reflectance and thus a dynamic increase in the light scattering, as was shown for blood in Paper III. This vaporisation is employed in laser surgery, where the scalpel is replaced by a laser beam. Tissue can also be destroyed at temperatures below the water vaporisation threshold. Protein denaturation (coagulation) is induced at temperatures above 45°C, and deactivation of the cellular enzymatic processes can already be observed at 40°C. These are the underlying mechanisms of thermotherapy and laser-induced hyperthermia. The optical effects of hyperthermia are insignificant, in contrast to those caused by thermotherapy. We will therefore focus on the tissue optics in conjunction with thermotherapy in this chapter.

8.2.1 The light energy deposition

Thermotherapy is primarily used for cancer therapy and elimination of vascular malformations such as port-wine stains. The temperature distribution, which here is the origin of the treatment effect, is not only governed by the thermal properties of tissue, *i.e.* the thermal conductivity [$\text{W m}^{-1} \text{K}^{-1}$] and specific heat [$\text{J kg}^{-1} \text{K}^{-1}$], but also by the source and sink configuration. A typical sink in tissue, is the blood flow from the heated volume, which is dependent on the perfusion rate [s^{-1}]. The source term is simply the incident light energy deposition. A variable influencing the energy deposition is the distribution of the *treatment light*. With basic knowledge of the wavelength dependence of the optical properties, as was discussed in Chapter 7, the optimum light distribution can be designed by correct selection of the wavelength in order to illuminate appropriate the volume. If a

wavelength in the tissue optical window is selected, for instance 1064 nm produced by a continuous wave (c. w.) Nd:YAG laser, this enables high optical penetration depth and thus a temperature distribution with a peak 1-2 mm beneath the irradiated tissue surface, followed by a slow decrease with depth.¹⁹⁵ In contrast, the temperature distribution following continuous irradiation with a wavelength in the blue/green range (producing one tenth the penetration) generates a higher peak value, although this is located at the tissue surface. There is also a much more rapid attenuation with tissue depth.¹⁹⁵ Superficial lesions are thus efficiently treated by the latter system. However, instead of a high maximum temperature, as obtained with blue/green light, a greater treatment depth and a more even temperature distribution is normally desired in a clinical setting. This is why NIR radiation can be used with advantage. The reason for this is to achieve complete eradication of peripheral malignant cells.

The energy deposition is also governed by the *thermally active part of the optical absorption coefficient*, which can now be regarded as a light-heat transformation efficiency coefficient. When using NIR light, which is normally clinically preferred, the entire average absorption coefficient of the irradiated tissue volume is essentially thermally active. This is because only an insignificant portion of the absorbed light energy is lost via other pathways in the NIR-range, compared to that being transferred to thermal energy. At shorter wavelengths some of the light energy is lost due to for instance fluorescence, phosphorescence or chemical energy, which results in a lower thermally active part of the average absorption coefficient. Moreover, the thermal μ_a is at some wavelengths completely dominated by the absorption of one tissue constituent. This is true for tissue containing chromophores with distinct spectral absorption bands, for instance blood with its highly light absorbing haemoglobin. Thus, the transfer from light to thermal energy solely takes place in the predominantly absorbing tissue, enabling selective thermotherapy of this and only the immediately surrounding tissue. This approach is employed in the treatment of for instance vascular malformations.¹⁹⁶ This means that the vascularity can efficiently be destroyed, without thermal injuries being induced in the healthy less absorbing surrounding tissue, resulting in minimal scar formation. At first sight optimal photoselective treatment can be attained using wavelengths associated with maximal absorption coefficients of the target tissue. For vascular malformations this would be at 577 nm, the position of the highest absorption coefficient of blood. However, the configuration of the absorbers in the tissue has been shown to significantly influence the light distribution. For the treatment of vascular malformations, it has been shown experimentally that better treatment results are achieved using a wavelength of 585 nm, corresponding to a significantly lower absorption coefficient of the blood.¹⁹⁷ The explanation of this has been found via Monte Carlo modelling, which reveals that 585 nm yields a more homogeneous light and heat energy distribution, resulting in thermal damage to the entire vessel and not just the top surface, as with 577 nm.^{86,198} A lower absorption coefficient means that not only the blood absorbs less light, but also the surrounding vessels. Hence, a more pronounced diffuse light flux is formed, which is of advantage in the treatment efficiency of both the underside and of deeper lying vessels. This effect is not solely determined by the absorption coefficient of the blood, but rather by a product of the absorption coefficient and the vessel radius, which quantifies the *effective* light absorption, as well as the distance between the vessels. Verkruijsse *et al.*⁸⁷ have discussed the importance of considering the effective light absorption, rather than a configurationally uncompensated absorption coefficient when evaluating the light distribution. The reason for this is because the blood cells in the central

part of the blood vessel is optically less active, owing to the shadowing by the surrounding cells, as discussed in Chapter 7.

The *temporal outline* of the energy deposition influences the thermal distribution significantly. Continuous, or pulsed irradiation with exposure times longer than the thermal relaxation time, *i.e.* in the order of milliseconds¹⁹⁵ for blood, means a small fraction of the stored heat energy is continuously lost during the irradiation via thermal diffusion. This results in a widely distributed, less selective, thermal effect and a lower peak temperature. The thermal distribution will then mainly be determined by the thermal properties of the tissue, rather than by the optical properties.¹⁹⁵ In contrast, a local heating, more or less corresponding to the irradiated tissue volume, is obtained with a light exposure time in the order of, or less than, the thermal relaxation time. Thermal diffusion does not start until most of the light energy has been transferred into stored heat energy, resulting in a high local temperature. It follows from this that the thermal distribution is now mainly determined by the light distribution and thus the optical properties. High enough temperatures to cause thermal damage to a range of treatment volumes can be obtained by changing the length of the laser pulse. Thus, the pulse length determines the diameter of a blood vessel that can be successfully damaged.¹⁹⁹

8.2.2 The treatment response

The heat induces different types of damage, depending on the temperature as well as on the duration of the heat exposure. However, the general trend is lower temperatures require longer heat exposure and a higher temperature a shorter heat exposure, in order to induce a specific degree of thermal damage, mathematically expressed by a damage integral (for a review, see Jacques²). Low temperature in combination with long heat exposure time causes subtle damage, such as inactivation of vital enzymes followed by swelling of mitochondria and the endoplasmatic reticulum.^{200,201} Higher temperatures induce the typical thermal coagulation, *i.e.* immediate denaturation of proteins, irreversible modifications of other biomolecules such as the phospholipids in the membranes. In all, this causes morphological alterations of the organelles, membranes and extracellular components, and also small granules with the resulting degenerative material.²⁰⁰

Disregarding which of these is actually used (long or short heat exposure), distinct cellular damage can be achieved, which is necessary for the treatment of *e.g.* tumour tissue and port wine stains. For successful results, some kind of selectivity between diseased and normal tissue is desirable, such as for the blood vessel malformations in port-wine stains. This selectivity originates from the natural difference in absorption coefficients of blood and the surrounding dermal tissue at the wavelength of the treatment light. Selective thermal treatment of malignancies can also be achieved, since some cancer cells are more susceptible to elevated temperatures than normal cells. Vascular endothelial cells also exhibit this higher susceptibility, resulting in vascular damage and decreased blood supply, causing secondary injuries to the tumour tissue.²⁰² The selectivity is here obtained due to the abnormal tumour vasculature.

It is thus clear that morphological and vascular alterations occur during the treatment, these have been shown to affect the optical properties and consequently the light distribution. The disruption of the organelles, arranged in smaller aggregates, and also the formation of small granules of coagulated proteins following thermal coagulation has been shown to increase

the reduced scattering coefficient (by a factor ranging from 2 to 7 times, depending on the wavelength and tissue) when various tissue samples, such as aorta, myocardium, liver and muscle tissue, are either slowly heated *in vitro*,^{73,77,112,119,156,203,204} or instantaneously photo-coagulated during laser irradiation for 20-40 s.⁶⁰ The increase in reduced scattering coefficient was attributed to a decrease in the g-factor, as a result of the formation of smaller scattering aggregates.^{77,112,118,119,156} This is in good agreement with the lower g-factors for smaller particles by Mie theory computations, and also with the lower g-factor for “cloudy” compared to “clear” particles found from computations based on modified anomalous diffraction, as summarised in morphological changes on the scattering properties in Table 7.2. In order to investigate the influence of heat on not only the tissue matrix, but also on the main absorber in tissue, whole blood was slowly heated while monitoring its optical properties, as described in Paper IV. Small, but distinct, changes in the scattering properties were observed when the disc shaped red blood cells became spherical. The decrease in the g-factor is in accordance with the T-matrix computations when the light scattering by an oblate spheroid was compared to that by a sphere (see Paper V; see also Table 7.2). However, the increase in the absorption coefficient at higher temperatures was the most dominating modification observed. From their investigations on absorbance measurements of heated and irradiated blood, Tan *et al.*²⁰⁵ suggested these changes could be related to the formation of degradation products of haemoglobin, as well as to haemolysis.

In order to study the influence of thermotherapy on the scattering and absorption properties simultaneously and also take into account the configurational changes in the distribution of absorbers, due to the vascular damage, integrating sphere measurements were performed on samples from liver tissue exposed to thermotherapy *in vivo*, as described in Paper II. A doubling of not only the reduced scattering coefficient but also the absorption coefficient was found, the latter probably as a result of the vascular damage, or possibly due to heat-induced injuries to the blood cells, as previously discussed. Furthermore, by analysing the spectral shape of both the reduced scattering coefficient and the g-factor, employing Mie theory computations, the mean size of the average scatterer was estimated. This analysis found there was a 21-32% decrease in average scattering radius of treated as compared to untreated tissue, which again confirms the formation of smaller aggregates, as observed by microscopy.

Most studies of heat-induced changes in the optical properties have so far been performed on slowly heated tissue. This does not necessarily completely describe the changes arising when employing pulsed, intense laser irradiation. Lin *et al.*²⁰⁶ have shown that the changes observed during pulsed heating of skin and aorta contain both irreversible and reversible components. The irreversible part was attributed to the same mechanisms observed during slow heating, *i.e.* coagulation and dehydration. The existence of reversible phenomena was suggested to be associated with temperature dependent morphological changes in the tissue during the treatment, thermal lensing (non-uniform heating causes a gradient in the refractive index), thermal expansion of the tissue resulting in increased tissue thickness, and water transport. The dynamic behaviour of the reflectance and transmittance of a blood sample during a short, intense laser pulse, typically used for treatment of port wine stains, was investigated in Paper III. Two thresholds of exposures were observed for the reflectance at 2.9 and 6.3 J/cm², possibly due to an increase in the effective scattering due to coagulation (first increase) and vaporisation and bubble formation (second increase). The transmittance displayed an initial continuous decrease until the first threshold of the reflectance was reached. A smooth, continuous increase was then followed, until a sudden

step-like increase occurred at the vaporisation exposure of 6.3 J/cm^2 . The changes in the transmittance before the vaporisation were shown to correspond closely with a temperature dependent absorption coefficient, which increases with temperature until 100°C .

All this implies the dynamic behaviour of the source term during the treatment, which influences the thermal distribution when pulsed heating with short pulse lengths is used, because of the significant changes in the optical properties. It has also been theoretically confirmed by Rastegar and Motamedi,²⁰⁷ employing a dynamic heat distribution model. A linear increase in the reduced scattering and absorption coefficients with increasing temperature results in a clearly more rapid temperature rise, particularly close to the surface, than if the optical properties were constant during the treatment. However, Splinter *et al.*²⁰⁸ have experimentally shown that the influence of the dynamic optical properties on the thermal distribution cannot even be neglected during continuous-wave irradiation, when optical properties are supposed to have less influence on the heat distribution.

9. Optical diagnostic techniques - tissue optical aspects

Optical diagnostics offers a wide range of applications in non-intrusive monitoring of fundamental information related to the physical, chemical and biological processes in tissue for medical purposes. All physical disorders can be associated with biochemical, physiological and morphological alterations in tissue. These changes can affect the interaction processes between light and tissue from molecular to cell layer level. The corresponding modifications of the optical signals form spectral fingerprints, which allows tissue characterisation in relation to malformations, malignancies, inflammatory reactions, hypoxia/hyperoxia, etc. to be made.

The detected light has undergone a number of interactions, including emission from light absorbing molecules, inelastic and/or elastic scattering events, *i.e.* processes either inducing a shift in the wavelength (fluorescence and inelastic scattering) of the incident light, or not (elastic scattering). Depending on the underlying interaction mechanism, four main categories of diagnostic techniques can be identified. *Laser-induced fluorescence* (LIF) is based on resonant light absorption followed by re-emission of a photon with only a fraction of the absorbed energy, the fluorescence photon. The shift in wavelength is referred to as the Stokes shift. *Raman spectroscopy* and *laser-Doppler flowmetry* are based on inelastic and quasi-elastic scattering, respectively, resulting in a wavelength shift. The spectrally narrow Raman shift is obtained via an interaction process between the photon and molecule, primarily involving excitation to a virtual, non-resonant level (though real levels can also be involved) followed by a rapid de-excitation, yielding a slight shift in the vibrational energy of the molecule. The laser-Doppler shift originates from a quasi-elastic scattering process between a photon and a molecule in motion, *e.g.* in flowing blood cells. This dynamic scattering causes a transfer of the kinetic energy of the molecule to the photon, dependent on the velocity of the molecule. Finally, *elastic scattering spectroscopy* comprises in its widest definition all types of reflectance and transmittance techniques employing elastically scattered light. The underlying photon-molecule interaction is extremely rapid (in the order of fs), and therefore too short for mutual energy transfer, only a change in the direction and possibly polarisation of the photon would be possible. The energy transfer, molecule to photon, associated with the appropriate interaction mechanisms of a particular diagnostic technique can be recognised in some of the energy level diagrams shown in Figure 7.1 and Figure 7.6. It is thus clear that these diagnostic methods are founded on the basic mechanisms of tissue optics, as defined by the absorption and scattering parameters. An essential part of tissue diagnostics is therefore its implications in relation to tissue optical properties. Three of the above mentioned diagnostic categories will be discussed in this chapter. For information on the use of Raman spectroscopy as a diagnostic tool, reviews by Mahadevan-Jansen and Richards-Kortum²⁰⁹ should be referred to.

In all optical diagnostic techniques, the spectral distribution is dependent on the illumination and collection geometries. This is as a result of the wavelength dependence of the optical properties and thus of the wavelength dependence of the angular distribution of the scattered light. An ideal detection geometry would be to collect the total distribution of the scattered light. However, this is only possible utilising an integrating sphere, which is

impractical in a clinical setting. A flexible illumination/detection geometry based on optical fibres is instead frequently employed. One should then be aware of the fact that the fraction of the total reflectance collected by the detection fibre is dependent on the optical properties of the tissue and is thus wavelength dependent. This means that when evaluating a spectrum by calculating the ratio of two intensities at different wavelengths, the values utilised do not fully account for variations in the illumination and detection geometries. These depends on such small variations as for instance the distance between the illumination and detection fibres²¹⁰, detector fibre and tissue surface, as well as general differences in the illumination/detection system used. The latter being exemplified by the two different probing geometries illustrated in Figure 9.1. The illumination and detection using one single optical fibre in close contact with the tissue surface favours collection of photons of low optical penetration depth, and thus of shorter wavelengths. In contrast, separate surface illumination followed by collection with an optical fibre in close contact with the tissue surface enables the collection of photons with longer scattering history, since the collection fibre shades the tissue volume immediately beneath. From this it follows that the detection efficiency is greater for those photons from greater optical penetration depths, having in general longer wavelengths. However, the impact of the optical properties on the illumination and collection efficiency can be taken into account utilising a proper calibration routine.^{211,212} Furthermore, Mourant *et al.*²¹⁰ have demonstrated that a sophisticated choice of fibre separation (illumination versus detection fibres) enables light detection essentially independent of the scattering properties.

9.1 Laser-induced fluorescence

Laser-induced fluorescence (LIF) spectroscopy provides information on the tissue content of characteristic fluorescing endogenous or exogenous chromophores. Knowledge of the types of fluorophores and their individual distribution as well as concentration, can be used successfully for tissue characterisation. It can be thought of as a sensitive technique capable of collecting information from molecular probing instruments, sensing small changes in the tissue biochemical environment. Examples of such endogenous probing molecules, *i.e.* endogenous

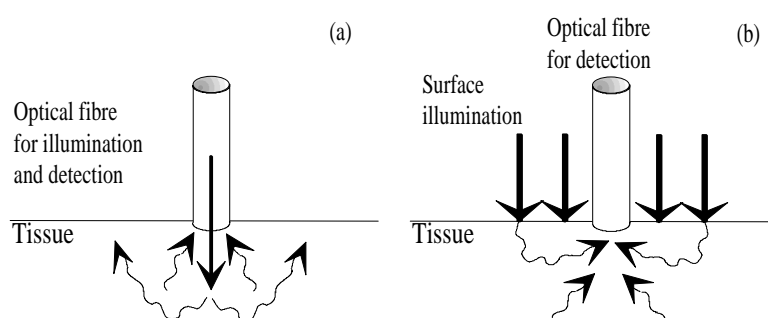


Figure 9.1 Schematic illustration of the impact of different illumination and detection geometries on the recorded signal. Illumination and detection via an optical fibre, as shown in (a), favours the collection of photons with low optical penetration depth. Surface illumination, as illustrated in (b), instead favours the collection of photons with a long scattering history.

fluorophores, are the aromatic amino acid tryptophan, present mainly in the proteins in the mitochondria, NADH (nicotin amide adenine dinucleotide) an important co-enzyme also active in the mitochondria, collagen and elastin in structural tissue. Other weaker fluorophores are carotene, flavin adenine dinucleotide (FAD) and keratin.

9.1.1 Propagation of excitation and emission light

Let us first consider the influence of the tissue optical properties on the excitation process. The fraction of the total absorption coefficient corresponding to the generation of laser-induced fluorescence (LIF), $\mu_{a,f}(\lambda_{ex})$ where λ_{ex} is the excitation wavelength, is in general not particularly significant compared to the total μ_a . However, there are spectral regions in which the fluorescence absorption coefficient can be substantial. Laser-induced fluorescence is mainly induced by excitation light with fairly short wavelengths, *i.e.* in the ultraviolet or blue spectral region, yielding fluorescence visible to the naked eye. However, since UV/blue light has a rather small penetration depth, this results in correspondingly minimal probing depth. In consequence detected fluorescence from the superficial tissue layers is relatively greater than that from lower lying tissues. For instance, the penetration depth of human aortic tissue at 360 nm was estimated to approximately 150 μm ,²¹³ a region in which tissue in general is to a large extent composed of an epithelial layer. This was also exemplified in Paper VII, where fatty and fibrous heart tissue could not be individually distinguished employing LIF, probably because the fatty heart tissue is covered by a thin fibrous pericardium. Furthermore, it implies that the fluorescence signal is particularly sensitive to changes in the epithelial layer, which can be profitable when searching for the superficial malignancies frequently accompanied by changes in epithelial thickness and composition,²¹⁴ as was shown for adenocarcinoma in Barrett's oesophagus in Paper VIII. Tissue with columnar epithelium tended to have lower auto-fluorescence than that with squamous epithelium. Furthermore, it is important to acknowledge that different tissues can have differing probing depths because of their characteristic optical properties. Tissues of high blood content absorb relatively more light, and therefore less is available for the excitation process which induces fluorescence. This results in an overall decrease in the magnitude of the entire fluorescence spectrum.

Once the excitation light has reached the fluorophore and a successful excitation occurs, fluorescence light can be emitted. The probing depth is thus not only dependent on the optical properties of the excitation light but also on those of the emission light. Monte Carlo simulations have shown that 30-40% of the fluorescence photons is remitted in the forward direction, *i.e.* away from the tissue surface.⁵³ This means that distal layers influence the fluorescence signal, yielding a larger effective probing depth than predicted by the penetration depth of the excitation light. The fluorophores exhibit peak intensities in fluorescence at various wavelengths depending on the molecular energy level structure. For instance, if an excitation wavelength of 337 nm is used, then tryptophan and collagen display their fluorescence peaks at approximately 390 nm, elastin at 410 nm, NADH at 470 nm and carotene at 520 nm. All peaks are broad with a FWHM in the order of 100 nm, since the excited fluorophore can return to any of the vibrational levels within the ground state, during the emission of fluorescence photons with a broad range of energies, as illustrated in Figure 9.1. Auto-fluorescence spectra from tissues, containing a mixture of fluorophores, are essentially an integral of the individual fluorescence spectrum of these fluorophores. The spectral characteristics, required to distinguish different tissues and also those with malignant irregularities, are those given by the variations in fluorophore

composition and concentration, as well as the chemical environment. For example, the various tissue layers in the skin display different auto-fluorescence emission characteristics, in relation to intensity and spectral shape, indicating a non-homogeneous distribution of different fluorophores in normal skin (excitation wavelength: 442 nm).²¹⁵ Atherosclerotic arteries exhibit a red shift and broadening in peak fluorescence, compared to normal aortic tissue at an excitation wavelength of 308 nm, which was considered to be related to an accumulation of oxidised lipoproteins.²¹⁶ Moreover, fibrous, scarred myocardium show increased fluorescence emission at wavelengths in the range 440-475 nm, using 308 nm excitation, compared to normal myocardium.²¹⁷ Paper VII confirms this ability to discriminate between normal myocardium and fibrous, or fatty heart tissue, using LIF with an excitation wavelength of 337 nm. As a final example, Paper VIII shows that the auto-fluorescence peak at approximately 500 nm, using 405 nm excitation, is significantly lower for adenocarcinoma in Barrett's oesophagus, compared to normal oesophageal mucosa. This could be attributed to a different structure and possibly thickness of the epithelium, as previously discussed, but alterations in auto-fluorescence also originates in changes in fluorophore composition/concentration, as well as chemical environment, as shown by the examples presented. The latter can for instance be seen in tumour tissue, which in general has a slightly lower pH than normal tissue. This could affect the NADH/NAD⁺ balance and thus the fluorescence component originating from NADH.²¹⁸

9.1.2 Fluorescence from exogenous fluorophores

In order to enhance the demarcation between normal and malignant tissue, a tumour selective drug is frequently administered consisting of the same photosensitisers as those used for PDT, but either at a lower dose²¹⁹ or in connection with the treatment session.²²⁰ With an excitation of 405 nm, probing at the maximum absorption coefficient, porphyrin-based photosensitisers fluoresce with a characteristic double peak at 630 and 690 nm for Photofrin and 635 and 705 nm for ALA-induced PpIX. Thus, the spectral shape of the auto-fluorescence, originating from endogenous fluorophores, is combined with these distinct peaks. The general idea is to base the demarcation criterion not only on the changes in auto-fluorescence, frequently observed as an overall decrease in tumour tissue, but also on an increase in fluorescence emission originating from the porphyrins accumulated in the malignancy. For instance, topically applied ALA, in conjunction with PDT, of basal cell carcinomas in the skin was found after six hours to fluorescence at 635 nm 2.4 times more intensely in the lesion compared to the surrounding normal skin, see Paper IX. However, we must remind ourselves of the low probing depth of LIF using ultraviolet/blue excitation light. Hence, this technique does not give any information on the drug accumulation at greater depths in the lesion. It is thus interesting to notice the trend, though apparently insignificant, that lesions requiring retreatment possessed on average a higher fluorescence intensity associated to the PpIX than lesions requiring only one treatment. This might indicate a shallow drug penetration and thus a higher degree of superficial accumulation of PpIX. However, one should be careful drawing such conclusions from measurements performed on lesions with different optical properties, as previously discussed. Incorporation of the decrease in auto-fluorescence yields a demarcation factor of the malignant as compared to the healthy tissue of between 7.4 and 9.5. The kinetics of the drug accumulation can be followed utilising LIF, the maximal demarcation at the probe depth was found to be 2-4 hours after applying the ALA onto the skin, see Paper X. However, the drug does not always exhibit the desired tumour selectivity as indicated in these studies. The fluorescence signal, corresponding to the porphyrins following low-dose intravenous

injection of Photofrin, was found on average to be only 1.2 times higher in oesophageal adenocarcinoma, as compared to that in normal oesophageal mucosa, see Paper VIII. The demarcation between malignant and healthy tissue can thus be mainly attributed to a sufficient difference in auto-fluorescence.

9.1.3 Evaluation methods

Fluorescence spectra are traditionally evaluated by calculating ratios, for instance between the intensities of the auto-fluorescence and photosensitiser peaks, in order to substantiate the characteristic spectral differences between various tissue types without interference of for instance intensity variations of the excitation light. Paper VII shows that better discrimination can be obtained for cardiovascular tissue by including the entire spectral information in the analysis utilising powerful analysis techniques such as Principal Component Analysis (PCA).²²¹ PCA extracts the main spectral features from a set of measured spectra in terms of the principal component spectra. Each spectrum measured can then be characterised by its composition ("amount") of the principal components. It, however, allows at the most qualitative analysis of tissue fluorophores but not quantitative estimates, owing to the influence of the tissue optical properties and boundary effects, unless combined with a rigorous calibration routine. Durkin and Richards-Kortum⁶¹ have shown that full spectral analysis, in their case performed by the method of partial least squares, can in combination with a set of controls with known fluorophore concentrations and optical properties of the surrounding medium, yield quantitative information of the fluorophore concentration. This could be of particular importance in order to determine the concentration of photosensitiser for PDT, an important dosage parameter for optimal treatment.

When analysing fluorescence spectra, it is important to bear in mind that the fluorescence light has been filtered through the tissue before being detected. This means that the tissue optical properties have left their fingerprint on the spectral shape of the fluorescence. The most pronounced spectral features originate from the main absorber in tissue, in the visible range - the blood - with manifest absorption bands in its oxygenated state at 418, 542 and 577 nm, as can be seen in Figure 7.2 and Figure 7.5. These can often show up as dips in the fluorescence spectra, which must not be misinterpreted as features originating from the fluorescence signals. Another phenomenon, associated with the absorption coefficient, is the self-absorption. This originates from the overlapping of the emission and absorption spectra of the fluorophores, yielding a more efficient absorption of the fluorescence light at shorter wavelengths and thus a red-shift of the measured compared to the intrinsic fluorescence spectrum. The wavelength dependent scattering properties affect the spectral shape of the fluorescence as well, since they determine the average photon path length and thus the degree of absorption. The fluorescence light with longer wavelengths is less efficiently scattered than that at shorter wavelengths according to the general behaviour of the reduced scattering coefficient, as discussed in Chapter 7.2 and shown in Paper II. This means that fluorescence light at longer wavelengths experiences a slightly shorter path than fluorescence light with shorter wavelengths and is consequently less effectively absorbed. Hence, fluorescence light at shorter wavelengths are more efficiently absorbed, again causing a red-shift. This has experimentally been verified by Ahmed *et al.*²²²

Several methods have been presented which are capable of distinguishing the intrinsic fluorescence light from the total detectable. In addition to the previously described method based on a control set of reference fluorescence spectra derived by Durkin and Richards-Kortum,⁶¹ an analytical relationship between the intrinsic and measured fluorescence has been developed utilising information from a diffuse reflectance spectrum. However, only relative information on tissue-fluorophore composition can be deduced from this.²²³ Absolute values can however be obtained by employing a technique developed by Gardner *et al.*,²²⁴ based on the knowledge of not only the diffuse reflectance but also the effective light penetration depth (*i.e.* a simple average measure of the optical properties). Furthermore, there is a method based on a transfer function, derived from Kubelka-Munk theory, which can also be used to derive absolute concentrations of the fluorophores. Experimentally, a dual-wavelength excitation and detection method has been shown to successfully determine hematoporphyrin derivative concentrations in a tissue phantom using a dimensionless ratio, which is independent of the optical properties.²²⁵ This concept has been shown to be useful when evaluating fluorescence spectra obtained from pigmented lesions in the skin following topical application of ALA.²²⁶ This is because the variations in fluorescence detected are independent of the tissue optical properties - here pigmentation variations - and thus can be entirely related to the drug. It has also been confirmed experimentally that the diffuse reflectance spectrum can be used as a first order approximation to compensate for the interference of the fluorescence spectrum due to absorption and scattering,²¹⁵ as predicted theoretically.²²³

9.2 Elastic scattering spectroscopy

Elastic scattering spectroscopy directly probes all tissue chromophores and scatterers, providing information on the composition and biochemistry of the tissue matrix. Thus, the impact of the tissue optical properties on the registered signal, which in LIF-spectroscopy often is considered to degenerate the desired information from the fluorophore, corresponds here to the primary carrier of information. The fraction of the incident light, which passes elastically through the tissue, can be used to characterise tissue morphology from the scattering history of the monitored photons. From the photons "lost" to other inelastic interaction processes, information regarding tissue chromophores can be gained.

The spectroscopic diagnostic techniques using elastically scattered light are essentially those described in Chapter 6.2, since elastic scattering spectroscopy is basically equivalent to the determination of tissue optical properties, although not necessarily quantitatively. All types of reflectance and transmittance measurements are employed, either determining the total amount present, or monitoring the resolved signal with respect to space or time. By appropriately choosing the wavelength of the probing light in relation to the general wavelength dependence of the optical properties, not only can the probe depth be varied, but the microscopic tissue variables can also be selectively characterised, as discussed in Chapter 7. *Visible* light is highly scattered and consequently mainly contains information on tissue structure and cell morphology, such as on shape and size of extracellular structural tissue components, cells and their organelles. This spectral range is thus applied in flow cytometry, where the light scattering from individual cells is analysed, providing information on cell volume, shape, refractive index, etc..^{173,227} It has been shown from analysis of the characteristics of the diffuse back-scattered linearly polarised light in the visible range, that information on the concentration and size of particles in a scattering tissue phantom can be obtained.¹⁵ The average size of the scatterer in a tissue phantom¹⁴ or

tissue can also be derived from the slope of the g -factor, or reduced scattering coefficient, plotted as a function of the wavelength in the visible region, as shown in Paper II. The scattering properties have a particularly strong influence on the reflectance, which indicates that tissue characterisation, with respect to size of the tissue component, can be performed using elastic scattering spectroscopy based on the spectral shape of diffusely reflected visible light. This has experimentally been shown by Mourant *et al.*,²²⁸ who were able to distinguish malignant from normal tissue in the bladder wall, with a diagnostic algorithm based on the slope of reflected light collected by an optical fibre. The change in slope was considered to be related to an increase in the nucleus/cytoplasm ratio for malignant cells, which is expected to affect the scattering properties of tissue. Since other studies of the optical properties of malignant, or treated versus healthy and untreated tissues, display differences in both scattering coefficients and also their spectral shape in the visible range,^{60,77,119,154,156,203,204} a wide applicability of this optical biopsy technique can be anticipated. The visible spectral region contains a few characteristic broad absorption bands, due to the electronic transitions in haeme-containing biomolecules. These spectral features can also be used for tissue characterisation utilising the difference in tissue content and distribution of biomolecules such as haemoglobin, myoglobin and cytochromes. For instance, assessment of the thickness of vessels, comprising vascular malformations such as port wine stains, as well as their depth, can be obtained from visual reflectance spectra.²²⁹ These are important parameters necessary to design the optimal treatment conditions and also evaluate the treatment response.^{230,231}

The *near infrared* wavelength region 700-1300 nm, identified as the "tissue optical window" comprising minimal absorption and scattering coefficients in tissue, is employed for a wide range of applications associated with a requirement of deep probing. Measurements of the oxygenation content in blood can be obtained using reflected light at two appropriately selected wavelengths, to maximise differences in absorption spectra for oxy- and deoxyhaemoglobin. These occur at for instance 665 and 955 nm⁴¹ and at 660 and 813 nm,²³² which can be used to determine the *relative* oxygenation. Transmission measurements have also been performed, in order to monitor cerebral and myocardial oxygen sufficiency.^{233,234} *Absolute* values of the absorption coefficient and thus the concentrations of haemoglobin (Hb) and oxyhaemoglobin (HbO₂) are not so easy to determine using the reflectance/transmittance measurements, since the effective pathlength of the recorded light within the tissue is unknown due to multiple scattering. In general measurements are thus primarily used to obtain relative values. Matcher and Cooper²³⁵ have demonstrated an alternative approach in order to determine absolute concentrations of Hb/HbO₂. The trick is to estimate the effective pathlength of the probe light by correlating the absorption bands of water with its known concentration in tissue and use this to derive the absorption coefficient and consequently the concentrations of Hb/HbO₂. Furthermore, time-resolved transmission measurements in the short-wave NIR-range can be conducted in order to detect inclusions, such as tumours, deeply located within the tissue, such as breast tissue^{70,236,237} in the development of optical mammography.

The absorption coefficients of near infrared light at longer wavelengths (1-2.5 μ m) are in general slightly higher due to the water absorption. However, distinct but weak absorption bands, originating from combinations and overtones of O-H, C-H and N-H stretching bands can also be found. They have for a long time been regarded as of no value for tissue identification,²³⁸ due to their weak character and a certain overlap between some of the bands. With improved analytical techniques based on the whole spectral data, this

wavelength range has now been acknowledged as having significant potential for tissue characterisation. For instance, the characteristic spectral features have been shown to provide both quantitative and qualitative information on lipid and protein content in tissue samples.^{239,240} Moreover, Paper VII has shown that NIR light in the range 1-2.5 μm can be utilised to characterise cardiovascular tissue in terms of normal myocardium, aorta, fatty and fibrous heart tissue, provided a powerful analytical method of principal components²²¹ (PCA) is available. The wavelength segment between 2.0 and 2.3 μm appears to be particularly feasible, partly because it contains interesting spectral features, but also due to a local minimum in water absorption, as discussed in Chapter 7.1. These characteristics result in a greater probe depth, as well as an improved signal-to-noise ratio.

Finally, *mid-infrared* light exhibits distinct vibration absorption bands, which can be used readily for quantitative analysis of biochemical composition of tissue samples, for instance in conjunction with analysis of colorectal cancer tissue,²⁴¹ atherosclerotic arteries²⁴² and myocardial tissue following infarction.²⁴³ However, as previously mentioned, due to strong water absorption and consequent insignificant probe depth, this spectral region is less feasible in a clinical setting.

9.3 Laser-Doppler flowmetry

The two previously discussed diagnostic techniques assess disorders apparent in the tissue matrix, *i.e.* malignancies, scar formation, atherosclerotic plaque, hypoxia/hyperoxia, etc., corresponding to structural changes in biomolecules. However, laser-Doppler flowmetry is used to probe alterations in the peripheral blood flow, corresponding to a secondary response to physiological changes under normal as well as pathological conditions. Various stimuli such as inflammatory reactions, temperature changes, electrical skin stimuli, etc.^{192,244,245} affect the microcirculation, as do common diseases such as diabetes and arteriosclerosis. Since the microcirculation exhibits local spatial variations, an imaging technique is required to evaluate a more representative average portion of the perfusion in the affected tissue than is possible using the limited spacial information provided by the fibre optical probe. Such a technique is Laser Doppler Imaging (LDI).²⁴⁶

The general principle of laser-Doppler imaging is to scan a laser beam over the tissue surface. The wavelength of the probing light is usually around 633 nm, at which the blood absorption is relatively low, in order to minimise the number of photons "lost" in the interaction events with the blood cells. This results in a sampling depth estimated to approximately 200-240 μm in skin, depending on the blood content.^{28,246,247} However, by shifting the wavelength of the probing light to the NIR spectral range, a probing depth in the order of 1-10 mm can be achieved,^{28,56} depending on the source/detection geometry. Thus, the actual sampling depth is dependent on the tissue optical properties. It is therefore questionable whether the blood perfusion results obtained from lesions of different thicknesses or optical properties can be interrelated. This is exemplified for basal cell carcinomas in Paper XI, showing that nodular lesions display lower perfusion than those which are superficial. The thicker and more dense tissue matrix in a nodular lesion probably prevents the light from reaching the same microvascular depth as that probed for a superficial lesion.

When light interacts with a moving blood cell via quasi-elastic scattering, a fraction of the kinetic energy is transferred to the scattered photons resulting in a Doppler-shift. This shift is extremely small, in the order of 10^{-11} times the frequency of the incident beam.²⁴⁸ It is, however, macroscopically discernible as a fluctuating speckle pattern, originating from the combination of the light scattered by the static tissue matrix with the Doppler-broadened light from the moving blood. The speckle pattern is imaged on a detector as a fluctuating signal with intensity modulation at the Doppler frequency:

$$\text{Eq. 9.1} \quad \Delta f = \frac{1}{2\pi} (\mathbf{k}_s - \mathbf{k}_i) \cdot \mathbf{v},$$

where \mathbf{k}_i and \mathbf{k}_s are the wave vectors of the incident and scattered light, and \mathbf{v} is the velocity vector of the moving blood cell. Since the blood cells flows in various directions and the incidence/scattering angles of the photons vary, the modulation frequency (*i.e.* the Doppler shift) has a certain distribution. From this frequency distribution the velocity distribution of the moving blood cells can be deduced.²⁴⁶ Moreover, the magnitude of the fluctuations corresponds to the concentration of blood cells. The perfusion is then simply a product of the average velocity, obtained from the velocity distribution, and the concentration of blood cells in the illuminated sampling volume.

Kienle *et al.*³⁰ have shown that a laser Doppler spectrum depends on the optical scattering properties of the flowing medium. From a clinical point of view, this is of less importance, since relatively small differences in the scattering properties of blood is expected *in vivo*. However, the optical properties of the surrounding tissue matrix are not invariant. They affect not only the sampling depth and volume, as previously mentioned, but also directly the distribution of Doppler shifts in the case where the light is highly directed. The reason for this is that the shift is dependent on the direction of the incident light. Tissue is in general a rather strongly scattering medium in the visible wavelength range. This means that isotropic probing light is generated at reasonably short distances from the surface. Thus, the direct influence of the optical properties on the Doppler shift is probably negligible for source/detection geometries favouring the collection of photons with longer scattering histories in the tissue matrix. This was verified for a large (in the order of centimetres) source versus detection fibre separation⁵⁶ (g -factors in the range 0.5-0.9 at $\mu_s' = 1.0 \text{ mm}^{-1}$ and $\mu_a = 0.001 \text{ mm}^{-1}$) by Monte Carlo simulations. However, an influence of the g -factor on the Doppler spectrum has been observed at a smaller fibre separation (in the order of millimetres), in conjunction with Monte Carlo computations for optical properties close to those of the skin ($g = 0.875$, $\mu_s = 11\text{-}25 \text{ mm}^{-1}$ and $\mu_a = 0.01\text{-}0.015 \text{ mm}^{-1}$).²⁸ An extended study is recommended, in order to conclude within what range of the optical properties and for which source/detection geometries this effect has to be considered.

Laser Doppler measurements utilising an imaging approach involves a scanning procedure over the tissue surface being imaged, typically the area in the order of $5 \times 5 \text{ cm}$. The blood perfusion is deduced from step measurements during the scanning, and stored as a pixel value in a laser-Doppler image. This results in a spatial resolution in the order of millimetres, partly due to the strong scattering by tissue. A high-resolution laser-Doppler perfusion imager has been designed, yielding a spatial resolution corresponding to the diameter of the probe beam used, *i.e.* in the order of 0.1 mm ²⁴⁹. Substantially higher spatial resolution ($2\text{-}10 \mu\text{m}$) can be obtained by combining Doppler velocimetry with the optical coherence tomography (OTC) approach.²⁵⁰ The latter method is founded on the technique of

low-coherence reflectometry, as briefly described in Chapter 6.2.4. OTC provides tomographic images of the tissue with a high resolution. When combined with the laser Doppler technique, high resolution laser Doppler images can be obtained. This optical Doppler tomography technique has been demonstrated *in vivo* on blood flow in small vessels embedded in highly scattering tissue (skin) some 200 μm below the surface. OTC would for instance be a powerful tool for further studies on microvascular injuries, in conjunction with PDT following topically applied ALA. This could be carried out to confirm the results obtained with conventional low resolution LDI described in Paper XI and to provide a better insight into what occurs at the microscopic level. LDI has been utilised to estimate the tissue perfusion in conjunction with cryo therapy, as well as with ALA-PDT on basal cell carcinomas in the skin, as discussed in Paper XI. This study showed that LDI is a promising technique for assessment of the healing, since the perfusion in the residual/recurrent tumours do not recover to normal perfusion values, as do lesions requiring only one treatment session.

10. Summary of papers

Paper I to Paper IV report on changes in optical properties in the visible spectral range, arising in conjunction with laser-based treatments, using various integrating sphere set-ups. These exemplify the close relationship between optical properties and physiological, as well as morphological alterations in tissue. A single integrating sphere set-up, employing a Xe-lamp as the light source in combination with a monochromator, was utilised in *Paper I*. In this study the absorption coefficient of rat liver and muscle tissue was found to increase by 30-70% and 50-100%, respectively, after PDT performed *in vivo*. This could probably be due to damage to the microvasculature as a result of the treatment. In *Paper II*, the single integrating sphere set-up was rebuilt with a spectrometer combined with a CCD-camera as the detector, thus enabling the acquisition of total spectra of optical properties. Changes in the optical properties of rat liver tissue, treated by thermotherapy employing a continuous wave Nd:YAG laser, were determined. An increase of 200% in not only the absorption, but also the effective scattering coefficient was found, indicating vascular as well as tissue matrix (coagulation) injuries. The entire spectral information on the reduced scattering coefficient, as well as on the g-factor was used to estimate a Mie equivalent average radius, corresponding to the average size of the scattering centres in the tissue. This was shown to be 20-30% lower in the tissue treated by thermotherapy compared to the untreated tissue. Finally, a double integrating sphere set-up was utilised in order to follow dynamic changes in the optical properties of blood. In *Paper IV*, the blood was slowly heated, causing a continuous increase in the absorption coefficient with temperature. An increase in temperature from 25 to 50°C induced an 80% increase in μ_a at 633 nm, which was suggested to be related to formation of degradation products, following haemoglobin denaturation, and/or haemolysis. Furthermore, a small but abrupt decrease in the g-factor, coinciding with a corresponding increase in the scattering coefficient, was observed when the disc shaped blood cells became spherical at a heating temperature of 45-46°C. The temperature dependent increase in the absorption coefficient was confirmed using pulsed heating in *Paper III*. An increase in the absorption coefficient of 250% was estimated, when the blood was heated from 20 to 100°C using a 0.5 ms laser pulse at 586 nm. The reflectance and transmittance signals measured during the pulse, revealed distinct changes dependent on the accumulated radiant exposure rather than the exposure time. A distinct increase in the reflectance was displayed after an accumulated exposure of 2.9 J/cm², which was accompanied by the development of coagulates in the blood. Moreover, a “popping” sound, indicating on vaporisation of the heated blood, was heard when both the reflectance and transmittance were found to significantly increase after an accumulated exposure of 6.3 J/cm².

In **Paper V**, T-matrix computations, with extended precision variables, were employed in order to estimate the influence of shape transformations of red blood cells, modelled as volume equivalent spheroids, on the angular distribution of the scattered light. Sphering as well as elongation of a spheroid, when maintaining the particle volume, cause a decrease in the g-factor. For the sphering, this decrease in the g-factor is in agreement with the experimental results presented in Paper IV. Moreover, near field computations reveal that optical measurements have to be performed on highly diluted blood to validate the

assumption of independent scattering. However, this also means that results from such measurements cannot be simply extrapolated to whole blood.

The potential of a fairly unexplored spectral region, from the viewpoint of clinical diagnostics, is for the cardiovascular tissue investigated in **Paper VII**. This study indicates a better specificity can be obtained with near infrared diffuse reflection spectroscopy, in the spectral range 0.8-2.3 μm , as compared to laser-induced fluorescence. The wavelength region 2.0-2.3 μm was shown to comprise of particularly useful information for tissue characterisation. This is partly due to a local minimum in the water absorption, allowing distinct absorption dips to be evaluated. The capacity and usefulness of Principal component analysis were demonstrated for both NIR- and LIF-spectroscopy. Spectral analysis utilising the entire spectral information appears to be a powerful analysis technique, as compared to analysis at single wavelengths.

Paper VI considers the influence of the optical properties of tissue on LIF-measurements. Three computational methods were developed, all based on the time-resolved Monte Carlo approach for light transport in tissue. One program, considered as the standard, treats each fluorescence phenomenon simply as a change in the optical properties. The other two programs separate the fluorescence in its two processes. The transport of the excitation light is simulated separately, from that of the emitted light, and the total was obtained via convolution. The results from all three programs were in good agreement, except for a normalisation factor, but the two condensed simulation programs produced the results significantly faster than the standard approach.

The clinical results obtained within the scope of this work are reported in **Paper VIII to Paper XI**. *Paper VIII* is entirely devoted to diagnostics using laser-induced fluorescence and intravenously injected low-dose Photofrin. The good discrimination obtained for severe dysplasia and adenocarcinoma in Barrett's oesophagus, could mainly be related to alterations in the auto-fluorescence rather than a selective uptake of the photosensitising drug. *Paper IX to Paper XI* report results from an ongoing clinical study, which is evaluating the treatment of basal cell carcinomas in the skin. It comprises a comparison between topically applied ALA combined with PDT on one hand and cryo therapy on the other. The papers discuss the potential of and results obtained from the optical diagnostics techniques, LIF and LDI, rather than any clinical evaluation of the outcome of the treatment, since the last of the one-year follow-up visits will not take place until the beginning of 1998. The LIF studies reveal that a 2.4 times higher PpIX fluorescence is on the average obtained in the lesion compared to the normal surrounding skin after six hours and that optimal demarcation at the probe depth is obtained 2-4 hours after the application of the ALA creme. No correlation between the fluorescence measurements performed immediately before the treatment and the treatment response was found. LDI seems to be a powerful tool to monitor and assess the outcome of the treatment during follow-up visits, since the elevated blood flow decreases to normal values after complete healing, in contrast to the residual/recurrent lesions. The submission of these papers is planned to occur when the clinical evaluation is completed.

The contributions by the author consisted of the experimental work, evaluation of data, programming, simulations and computations in all papers. Papers I, II, IV, V, VII, VIII and XI have been written and prepared by the author, while the participation in the preparation for and writing of Papers III, VI, IX and X was as one of the co-authors.

11. Acknowledgements

First of all, I would like to express my gratitude to Dr. Stefan Andersson-Engels. It has been of great value having a supervisor who has a broad knowledge of physics in general, but also a deep insight into each and every aspect of biomedical optics. I have also found it a great honour and pleasure in being a PhD-student in "the Svanberg-group", which has been established on the true enthusiasm and high working ideals of Prof. Sune Svanberg and Dr. Katarina Svanberg.

This work would have been impossible without the stimulating collaboration with all the people in the medical and other groups at the Division of Atomic Physics, as well as co-workers at Lund University Hospital, the Department of Electromagnetic Theory and also the Division of Solid State Physics. Special thanks to Prof. Martin van Gemert, his staff and students at the Laser Centre, Academic Medical Centre in Amsterdam for adopting me into their group, as if I belonged nowhere else. I consider the hard work, fruitful discussions and the friendly atmosphere I shared with Dr. Gerald Lucassen and Wim Verkrusysse, as some of the highlights of my time as a PhD student.

The special support from and friendship with some of the few young women within the field have meant a great deal to me. Anne, Lill-Tove, Lotta, Ingrid R and Ingrid W - thank you for being around. Not to mention all the support from my dear friends in Sandviken and Hedda's - thank you for listening and giving good advice.

The comfort in having a "allra-käraste" sister, a supportive mother who turns my darkest hours into daylight, and a father, who has proven that aims are there to be fulfilled and that hard work makes few things impossible, my family has meant more to me than I can ever express with words.

Beloved Jan, this work is truly yours as much as mine. For all that patience and encouragement - I dedicate this work to you with the hope for more time to our happiness and love.

This work was financially supported by the Swedish Research Council for Engineering Sciences, which is gratefully acknowledged.

12. References

1. E. Viherkoski, "Lasers in medicine," *Annales Chirurgiae et Gynecologiae* **79**, 176-181 (1990).
2. S. L. Jacques, "Laser-tissue interactions, photochemical, photothermal, and photomechanical," *Lasers in General Surgery* **72**, 531-558 (1992).
3. S. Svanberg, "Tissue diagnostics using lasers," in *Lasers in Medicine*, G. Pettit and R.W. Waynant, eds. (Wiley, New York, to appear).
4. A. Ishimaru, *Wave propagation and scattering in random media* (Academic press, New York, 1978).
5. K. M. Case and P. F. Zweifel, *Linear transport theory* (Addison-Wesley Publishing Co. 1967).
6. L. O. Svaasand and R. Ellingsen, "Optical properties of the human brain," *Photochem. Photobiol.* **38**, 293-299 (1983).
7. L. O. Svaasand and R. Ellingsen, "Optical penetration in human intracranial tumors," *Photochem. Photobiol.* **41**, 73-76 (1985).
8. S. T. Flock, B. C. Wilson, and M. S. Patterson, "Monte Carlo modeling of light propagation in highly scattering tissue - II: Comparison with measurements in phantoms," *IEEE Trans. Biomed. Eng.* **36**, 1169-1173 (1989).
9. J. M. Steinke and A. P. Shepherd, "Comparison of Mie theory and the light scattering of red blood cells," *Appl. Opt.* **27**, 4027-4033 (1988).
10. M. Kohl, M. Cope, M. Essenpreis, and D. Böcker, "Influence of glucose concentration on light scattering in tissue-simulating phantoms," *Opt. Lett.* **19**, 2170-2172 (1994).
11. M. Firbank, M. Oda, and D. T. Delpy, "An improved design for a stable and reproducible phantom material for use in near-infrared spectroscopy and imaging," *Phys. Med. Biol.* **40**, 955-961 (1995).
12. M. Kohl, M. Essenpreis, and M. Cope, "The influence of glucose concentration upon the transport of light in tissue-simulating phantoms," *Phys. Med. Biol.* **40**, 1267-1287 (1995).
13. U. Sukowski, F. Schubert, D. Grosenick, and H. Rinneberg, "Preparation of solid phantoms with defined scattering and absorption properties for optical tomography," *Phys. Med. Biol.* **41**, 1823-1844 (1996).
14. J. R. Mourant, T. Fuselier, J. Boyer, T. M. Johnson, and I. J. Bigio, "Predictions and measurements of scattering and absorption over broad wavelength ranges in tissue phantoms," *Appl. Opt.* **36**, 949-957 (1997).
15. A. H. Hielscher, J. R. Mourant, and I. J. Bigio, "Influence of particle size and concentration on the diffuse backscattering of polarized light from tissue phantoms and biological cell suspensions," *Appl. Opt.* **36**, 125-135 (1997).
16. H. J. van Staveren, C. J. M. Moes, J. van Marle, S. A. Prahl, and M. J. C. van Gemert, "Light scattering in Intralipid-10 % in the wavelength range of 400-1100 nm," *Appl. Opt.* **30**, 4507-4514 (1991).
17. W. F. Cheong, S. A. Prahl, and A. J. Welch, "A review of the optical properties of biological tissues," *IEEE J. Quant. Electr.* **26**, 2166-2185 (1990).
18. S. L. Jacques, C. A. Alter, and S. A. Prahl, "Angular dependence of HeNe laser light scattering by human dermis," *Lasers Life Sci.* **1**, 309-333 (1987).
19. G. Yoon, A. J. Welch, M. Motamedi, and M. J. C. van Gemert, "Development and application of three-dimensional light distribution model for laser irradiated tissue," *IEEE J. Quant. Electr.* **QE-23**, 1721-1733 (1987).
20. M. R. Arnfield, J. Tulip, and M. S. McPhee, "Optical propagation in tissue with anisotropic scattering," *IEEE Trans. Biomed. Eng.* **35**, 372-381 (1988).
21. L. G. Henyey and J. L. Greenstein, "Diffuse radiation in the galaxy," *Astrophysics Journal* **93**, 70-83 (1941).
22. W. M. Star, J. P. A. Marijnissen, and M. J. C. van Gemert, "Light dosimetry in optical phantoms and in tissue: 1 Multiple flux and transport theory," *Phys. Med. Biol.* **33**, 437-454 (1988).
23. J. H. Joseph, W. J. Wiscombe, and J. A. Weinman, "The delta-Eddington approximation for radiative flux transfer," *J. Atmos. Sci.* **33**, 2452-2459 (1976).
24. H. C. van de Hulst and R. Graaff, "Aspects of similarity in tissue optics with strong forward scattering," *Phys. Med. Biol.* **41**, 2519-2531 (1996).
25. J. R. Mourant, J. Boyer, A. H. Hielscher, and I. J. Bigio, "Influence of scattering phase function on light transport measurements in turbid media performed with small source-detector separations," *Opt. Lett.* **21**, 546-548 (1996).
26. R. Graaff, J. G. Aarnoudse, F. F. M. de Mul, and H. W. Jentink, "Light propagation parameters for anisotropically scattering media based on a rigorous solution of the transport equation," *Appl. Opt.* **28**, 2273-2279 (1989).
27. R. Graaff, A. C. M. Dassel, M. H. Koelink, F. F. M. de Mul, J. G. Aarnoudse, and W. G. Zijlstra, "Optical properties of human dermis *in vitro* and *in vivo*," *Appl. Opt.* **32**, 435-447 (1993).

28. M. H. Koelink, F. F. M. de Mul, J. Greve, R. Graaff, A. C. M. Dassel, and J. G. Aarnoudse, "Laser Doppler blood flowmetry using two wavelengths: Monte Carlo simulations and measurements," *Appl. Opt.* **33**, 3549-3558 (1994).
29. L. O. Reynolds and N. J. McCormick, "Approximate two-parameter phase function for light scattering," *J. Opt. Soc. Am.* **70**, 1206-1212 (1980).
30. A. Kienle, M. S. Patterson, L. Ott, and R. Steiner, "Determination of the scattering coefficient and the anisotropy factor from laser Doppler spectra of liquids including blood," *Appl. Opt.* **35**, 3404-3412 (1996).
31. A. N. Yaroslavsky, I. V. Yaroslavsky, T. Goldbach, and H.-J. Schwarzmaier, "The optical properties of blood in the near infrared spectral range," in *Optical diagnostics of living cells and biofluids*, D. L. Farkas, R. C. Leif, A. V. Priezzhev, T. Asakura, and B. J. Tromberg, eds., *Proc. Soc. Photo-Opt. Instrum. Eng.* **2678**, 314-324 (SPIE, Bellingham, 1996).
32. M. S. Patterson, B. C. Wilson, and D. R. Wyman, "The propagation of optical radiation in tissue. I. Models of radiation transport and their application," *Lasers Med. Sci.* **6**, 155-168 (1991).
33. A. J. Welch, G. Yoon, and M. J. C. van Gemert, "Practical models for light distribution in laser-irradiated tissue," *Lasers Surg. Med.* **6**, 488-493 (1987).
34. G. Yoon, S. A. Prahl, and A. J. Welch, "Accuracies of the diffusion approximation and its similarity relations for laser irradiated biological media," *Appl. Opt.* **28**, 2250-2255 (1989).
35. A. J. Welch and M. J. C. van Gemert, *Optical-thermal response of laser-irradiated tissue* (Plenum Press, New York, 1995).
36. P. Kubelka and F. Munk, "Ein Beitrag zur Optik der Farbanstriche," *Z. Tech. Phys.* **12**, 593-601 (1931).
37. P. Kubelka, "New contributions to the optics of intensely light-scattering materials. Part I," *J. Opt. Soc. Am.* **38**, 448-457 (1948).
38. M. J. C. van Gemert and W. M. Star, "Relations between the Kubelka-Munk and the transport equation models for anisotropic scattering," *Lasers Life Sci.* **1**, 287-298 (1987).
39. S. A. Prahl, M. J. C. van Gemert, and A. J. Welch, "Determining the optical properties of turbid media by using the adding-doubling method," *Appl. Opt.* **32**, 559-568 (1993).
40. K. M. Case, "Elementary solutions of the transport equation and their applications," *Annals of Physics* **9**, 1-23 (1960).
41. L. Reynolds, C. Johnson, and A. Ishimaru, "Diffuse reflectance from a finite blood medium: applications to the modeling of fiber optic catheters," *Appl. Opt.* **15**, 2059-2067 (1976).
42. A. Ishimaru, "Diffusion of light in turbid material," *Appl. Opt.* **28**, 2210-2215 (1989).
43. E. D. Cashwell and C. J. Everett, *A practical manual on the Monte Carlo method for random walk problems* (Pergamon Press, London, Great Britain, 1959).
44. G. N. Plass and G. W. Kattawar, "Influence of single scattering albedo on reflected and transmitted light from clouds," *Appl. Opt.* **7**, 361-367 (1968).
45. B. C. Wilson and G. Adam, "A Monte Carlo model for the absorption and flux distributions of light in tissue," *Med. Phys.* **10**, 824-830 (1983).
46. M. Keijzer, S. L. Jacques, S. A. Prahl, and A. J. Welch, "Light distribution in artery tissue: Monte Carlo simulations for finite-diameter laser beams," *Lasers Surg. Med.* **9**, 148-154 (1989).
47. L. Wang and S. L. Jacques, "Monte Carlo modeling of light transport in multi-layered tissues in standard C," (Laser Biology Research Laboratory, M. D. Anderson Cancer Center, University of Texas, Houston, Tex. 1992).
48. D. T. Delpy, M. Cope, P. van der Zee, S. Arridge, S. Wray, and J. Wyatt, "Estimation of optical pathlength through tissue from direct time of flight measurement," *Phys. Med. Biol.* **33**, 1433-1442 (1988).
49. S. L. Jacques, "Time resolved propagation of ultrashort laser pulses within turbid tissue," *Appl. Opt.* **28**, 2223-2229 (1989).
50. J. C. Hebden and R. A. Kruger, "Transillumination imaging performance: Spatial resolution simulation studies," *Med. Phys.* **17**, 41-47 (1990).
51. R. Berg, "Laser-based cancer diagnostics and therapy - Tissue optics considerations," Dissertation thesis (Lund Institute of Technology, Lund, 1995).
52. A. J. Welch and R. Richards-Kortum, "Monte Carlo simulation of the propagation of fluorescent light," in *Laser-induced interstitial thermotherapy*, G. Müller and A. Roggan, eds., The International Society for Optical Engineering (SPIE, Bellingham, Washington USA, 1995) pp. 174-189.
53. A. J. Welch, C. M. Gardner, R. Richards-Kortum, E. Chan, G. Criswell, J. Pfefer, and S. Warren, "Propagation of fluorescence light," *Lasers Surg. Med.* **21**, 166-178 (1997).
54. H. W. Jentink, F. F. M. de Mul, R. G. A. M. Hermesen, R. Graaff, and J. Greve, "Monte Carlo simulations of laser Doppler blood flow measurements in tissue," *Appl. Opt.* **29**, 2371-2381 (1990).
55. H. W. Jentink, F. F. M. de Mul, R. Graaff, H. E. Suichies, J. G. Aarnoudse, and J. Greve, "Laser Doppler flowmetry: measurements in a layered perfusion model and Monte Carlo simulations of measurements," *Appl. Opt.* **30**, 2592-2597 (1991).
56. G. Soelkner, G. Mitic, and R. Lohwasser, "Monte Carlo simulations and laser Doppler flow measurements with high penetration depth in biological tissuelike head phantoms," *Appl. Opt.* **36**, 5647-5654 (1997).

57. L. T. Perelman, J. Wu, I. Itzkan, and M. S. Feld, "Photon migration in turbid media using path integrals," *Phys. Rev. Lett.* **72**, 1341-1344 (1994).
58. L. T. Perelman, J. Wu, Y. Wang, I. Itzkan, R. R. Dasari, and M. S. Feld, "Time-dependent photon migration using path integrals," *Phys. Rev. E: Statistical Physics* **51**, 6134-6141 (1995).
59. R. Splinter, W. F. Cheong, M. J. C. van Gemert, and A. J. Welch, "In vitro optical properties of human and canine brain and urinary bladder tissues at 633 nm," *Lasers Surg. Med.* **9**, 37-41 (1989).
60. R. Splinter, R. H. Svenson, L. Littman, J. R. Tuntelder, C. H. Chuang, G. P. Tatsis, and M. Thompson, "Optical properties of normal, diseased, and laser photocoagulated myocardium at the Nd:YAG wavelength," *Lasers Surg. Med.* **11**, 117-124 (1991).
61. A. J. Durkin and R. Richards-Kortum, "Comparison of methods to determine chromophore concentrations from fluorescence spectra of turbid samples," *Lasers Surg. Med.* **19**, 75-89 (1996).
62. A. Roggan, H. Albrecht, K. Dörschel, O. Minet, and G. J. Müller, "Experimental set-up and Monte-Carlo model for the determination of optical tissue properties in the wavelength range 330-1100 nm," *Proc. Soc. Photo-Opt. Instrum. Eng.* **2323**, 21-46 (SPIE, Bellingham, 1995).
63. K. M. Yoo, F. Liu, and R. R. Alfano, "When does the diffusion approximation fail to describe photon transport in random media?" *Phys. Rev. Lett.* **64**, 2647-2650 (1990).
64. M. S. Patterson, B. Chance, and B. C. Wilson, "Time resolved reflectance and transmittance for the non-invasive measurement of optical properties," *Appl. Opt.* **28**, 2331-2336 (1989).
65. S. J. Madsen, B. C. Wilson, M. S. Patterson, Y. D. Park, S. L. Jacques, and Y. Hefetz, "Experimental tests of a simple diffusion model for the estimation of scattering and absorption coefficients of turbid media from time-resolved diffuse reflectance measure," *Appl. Opt.* **31**, 3509-3517 (1992).
66. T. J. Farrell, M. S. Patterson, and B. Wilson, "A diffusion theory model of spatially resolved, steady-state diffuse reflectance for noninvasive determination of tissue optical properties *in vivo*," *Med. Phys.* **19**, 879-888 (1992).
67. R. Cubeddu, M. Musolino, A. Pifferi, P. Taroni, and G. Valentini, "Time resolved reflectance: a systematic study for the application to the optical characterization of tissue," *IEEE J. Quant. Electr.* **30**, 2421-2430 (1994).
68. S. Andersson-Engels, R. Berg, and S. Svanberg, "Effects of optical constants on time-gated transillumination of tissue and tissue-like media," *J. Photochem. Photobiol. B: Biol.* **16**, 155-167 (1992).
69. J. C. Hebden, R. A. Kruger, and K. S. Wong, "Time resolved imaging through a highly scattering medium," *Appl. Opt.* **30**, 788-794 (1991).
70. R. Alfano, P.-P. Ho, and K.-M. Yoo, "Photons for prompt tumour detection," *Phys. World* **5**, 37-40 (1992).
71. K. Suzuki, Y. Yamashita, K. Ohta, and B. Chance, "Quantitative measurement of optical parameters in the breast using time-resolved spectroscopy. Phantom and preliminary *in vivo* results," *Invest. Radiol.* **29**, 410-414 (1994).
72. J. M. Steinke and A. P. Shepherd, "Diffusion model of the optical absorbance of whole blood," *J. Opt. Soc. Am. A* **5**, 813-822 (1988).
73. I. F. Cilesiz and A. J. Welch, "Light dosimetry: effects of dehydration and thermal damage on the optical properties of human aorta," *Appl. Opt.* **32**, 477-487 (1993).
74. P. Parsa, S. L. Jacques, and N. S. Nishioka, "Optical properties of rat liver between 350 and 2200 nm," *Appl. Opt.* **28**, 2325-2330 (1989).
75. J. W. Pickering, "Optical property changes as a result of protein denature in albumen and yolk," *J. Photochem. Photobiol. B: Biol.* **16**, 101-111 (1992).
76. R. van Hillegersberg, J. W. Pickering, M. Aalders, and J. F. Beek, "Optical properties of rat liver and tumor at 633 nm and 1064 nm: Photofrin enhances scattering," *Lasers Surg. Med.* **13**, 31-39 (1993).
77. J. W. Pickering, S. Bosman, P. Posthumus, P. Blokland, J. F. Beek, and M. J. C. van Gemert, "Changes in the optical properties (at 632.8 nm) of slowly heated myocardium," *Appl. Opt.* **32**, 367-371 (1993).
78. J. Qu, C. MacAuley, S. Lam, and B. Palcic, "Optical properties of normal and carcinomatous bronchial tissue," *Appl. Opt.* **33**, 7397-7405 (1994).
79. I. S. Saidi, S. L. Jacques, and F. K. Tittel, "Mie and Rayleigh modeling of visible-light scattering in neonatal skin," *Appl. Opt.* **34**, 7410-7418 (1995).
80. E. Chan, T. Menovsky, and A. J. Welch, "Effects of cryogenic grinding on soft-tissue optical properties," *Appl. Opt.* **35**, 4526-4532 (1996).
81. D. D. Royston, R. S. Poston, and S. A. Prahl, "Optical properties of scattering and absorbing materials used in the development of optical phantoms at 1064 nm," *J. Biomedical Optics* **1**, 110-116 (1997).
82. A. Pifferi, R. Berg, P. Taroni, and S. Andersson-Engels, "Fitting of time-resolved reflectance curves with a Monte Carlo model," in *Advances in optical imaging and photon migration*, R. R. Alfano and J. G. Fujimoto, eds., Optical Society of America **2**, 311-314 (Optical Society of America, Washington, D.C. 1996).
83. A. Pifferi, P. Taroni, G. Valentini, and S. Andersson-Engels, "Real time method for fitting time-resolved reflectance and transmittance measurements using a Monte Carlo model," submitted to *Appl. Opt.* (1997).

84. I. D. Miller and A. R. Veitch, "Optical modelling of light distributions in skin tissue following laser irradiation," *Lasers Surg. Med.* **13**, 565-571 (1993).
85. A. Kienle, L. Lilge, I. A. Vitkin, M. S. Patterson, B. C. Wilson, R. Hibst, and R. Steiner, "Why do veins appear blue? A new look at an old question," *Appl. Opt.* **35**, 1151-1160 (1996).
86. G. W. Lucassen, W. Verkruijsse, M. Keijzer, and M. J. C. van Gemert, "Light distributions in a port wine stain model containing multiple cylindrical and curved blood vessels," *Lasers Surg. Med.* **18**, 345-357 (1996).
87. W. Verkruijsse, G. W. Lucassen, J. F. de Boer, D. J. Smithies, J. S. Nelson, and M. J. C. van Gemert, "Modelling light distributions of homogeneous versus discrete absorbers in light irradiated turbid media," *Phys. Med. Biol.* **42**, 51-65 (1997).
88. R. A. J. Groenhuis, H. A. Ferwerda, and J. J. ten Bosch, "Scattering and absorption of turbid materials determined from reflection measurements. 1: Theory," *Appl. Opt.* **22**, 2456-2462 (1983).
89. S. T. Flock, B. C. Wilson, M. S. Patterson, and D. R. Wyman, "Monte Carlo modeling of light propagation in highly scattering tissues-I: model predictions and comparison with diffusion theory," *IEEE Trans. Biomed. Eng.* **36**, 1162-1168 (1989).
90. R. Graaff, M. H. Koelink, F. F. M. de Mul, W. G. Zijlstra, A. C. M. Dassel, and J. G. Aarnoudse, "Condensed Monte Carlo simulations for the description of light transport," *Appl. Opt.* **32**, 426-434 (1993).
91. S. T. Flock, B. C. Wilson, and M. S. Patterson, "Hybrid Monte Carlo - diffusion theory modelling of light distributions in tissue," in *Laser Interaction with Tissue*, M. W. Berns, ed., Proc. Soc. Photo-Opt. Instrum. Eng. **908**, 20-28 (SPIE, Bellingham, 1988).
92. L. Wang and S. L. Jacques, "Hybrid model of Monte Carlo simulation and diffusion theory for light reflectance by turbid media," *J. Opt. Soc. Am. A* **10**, 1746-1752 (1993).
93. A. Kienle and M. S. Patterson, "Determination of the optical properties of turbid media from a single Monte Carlo simulation," *Phys. Med. Biol.* **41**, 2221-2227 (1996).
94. C. F. Bohren and D. R. Huffman, *Absorption and scattering of light by small particles* (John Wiley & Sons, Inc. New York, 1983).
95. A. Ishimaru, *Electromagnetic wave propagation, radiation, and scattering* (Prentice-Hall, Inc. New Jersey, 1991).
96. J. Beuthan, O. Minet, J. Helfmann, M. Herrig, and G. Müller, "The spatial variation of the refractive index in biological cells," *Phys. Med. Biol.* **41**, 369-382 (1996).
97. P. W. Barber and C. Yeh, "Scattering of electromagnetic waves by arbitrarily shaped dielectric bodies," *Appl. Opt.* **14**, 2864-2872 (1975).
98. H. C. van de Hulst, *Light scattering by small particles* (Wiley, New York, 1957).
99. J. R. Zijp and J. J. ten Bosch, "Pascal program to perform Mie calculations," *Opt. Eng.* **32**, 1691-1695 (1993).
100. S. Asano and G. Yamamoto, "Light scattering by a spheroidal particle," *Appl. Opt.* **14**, 29-49 (1975).
101. S. Asano, "Light scattering properties of spheroidal particles," *Appl. Opt.* **18**, 712-723 (1979).
102. P. C. Waterman, "Symmetry, unitarity and geometry in electromagnetic scattering," *Physical Review D* **3**, 825-839 (1971).
103. S. C. Hill, A. C. Hill, and P. W. Barber, "Light scattering by size/shape distributions of soil particles and spheroids," *Appl. Opt.* **23**, 1025-1031 (1984).
104. M. I. Mishchenko, "Light scattering by size-shape distributions of randomly oriented axially symmetric particles of a size comparable to a wavelength," *Appl. Opt.* **32**, 4652-4666 (1993).
105. A. Quirantes Sierra and A. V. Delgado Mora, "Size-shape determination of nonspherical particles in suspension by means of full and depolarized static light scattering," *Appl. Opt.* **34**, 6256-6262 (1995).
106. R. M. P. Doornbos, M. Schaeffer, A. G. Hoekstra, P. M. A. Sloot, B. G. de Grooth, and J. Greve, "Elastic light-scattering measurements of single biological cells in an optical trap," *Appl. Opt.* **35**, 729-734 (1996).
107. M. G. Nichols, E. L. Hull, and T. H. Foster, "Design and testing of a white-light, steady-state diffuse reflectance spectrometer for determination of optical properties of highly scattering systems," *Appl. Opt.* **36**, 93-104 (1997).
108. P. Latimer, D. M. Moore, and F. Dudley Bryant, "Changes in total light scattering and absorption caused by changes in particle conformation," *J. Theoret. Biol.* **21**, 348-367 (1968).
109. P. Latimer and B. E. Pyle, "Light scattering at various angles. Theoretical predictions of the effects of particle volume changes," *Biophys. J.* **12**, 764-773 (1972).
110. J. C. Lin and A. W. Guy, "A note on the optical scattering characteristics of whole blood," *IEEE Trans. Biomed. Eng.* **21**, 43-45 (1974).
111. R. A. Meyer, "Light scattering from red blood cell ghosts: sensitivity of angular dependent structure to membrane thickness and refractive index," *Appl. Opt.* **16**, 2036-2038 (1977).
112. S. Thomsen, S. L. Jacques, and S. T. Flock, "Microscopic correlates of macroscopic optical property changes during thermal coagulation of myocardium," in *Laser-Tissue Interaction*, S. L. Jacques, ed., Proc. Soc. Photo-Opt. Instrum. Eng. **1202**, 2-11 (SPIE, Bellingham, 1990).

113. B. Beauvoit, T. Kitai, and B. Chance, "Contribution of the mitochondrial compartment to the optical properties of the rat liver: a theoretical and practical approach," *Biophys. J.* **67**, 2501-2510 (1994).
114. Q. Zhou and R. W. Knighton, "Light scattering and form birefringence of parallel cylindrical arrays that represent cellular organelles of the retinal nerve fiber layer," *Appl. Opt.* **36**, 2273-2285 (1997).
115. M. I. Mishchenko, D. W. Mackowski, and L. D. Travis, "Scattering of light by bispheres with touching and separated components," *Appl. Opt.* **34**, 4589-4599 (1995).
116. M. I. Mishchenko and L. D. Travis, "T-matrix computations of light scattering by large spheroidal particles," *Opt. Comm.* **109**, 16-21 (1994).
117. M. L. Daley, R. C. Watzke, and M. C. Riddle, "A model for the apparent decrease in optical transmittance of the diabetic eye," *IEEE Trans. Biomed. Eng.* **39**, 88-94 (1992).
118. S. Bosman, "Heat-induced structural alterations in myocardium in relation to changing optical properties," *Appl. Opt.* **32**, 461-463 (1993).
119. S. Jaywant, B. C. Wilson, L. Lilge, T. Flotte, J. Woolsey, and C. McCulloch, "Temperature dependent changes in the optical absorption and scattering spectra of tissues: correlation with ultrastructure," in *Laser-tissue interaction IV*, S. L. Jacques and A. Katzir, eds., *Proc. Soc. Photo-Opt. Instrum. Eng.* **1882**, 218-229 (SPIE, Bellingham, 1993).
120. B. Beauvoit, S. M. Evans, T. W. Jenkins, E. E. Miller, and B. Chance, "Correlation between the light scattering and the mitochondrial content of normal tissues and transplantable rodent tumors," *Anal. Biochem.* **226**, 167-174 (1995).
121. T. Kitai, B. Beauvoit, and B. Chance, "Optical determination of fatty change of the graft liver with near-infrared time-resolved spectroscopy," *Transplantation* **62**, 642-647 (1996).
122. R. L. Fante, "Relationship between radiative-transport theory and Maxwell's equations in dielectric media," *J. Opt. Soc. Am.* **71**, 460-468 (1981).
123. P. W. Barber and S. C. Hill, *Light scattering by particles: computational methods*. (World Scientific Publishing Co. Pte. Ltd. Singapore, 1990).
124. W. H. Press, S. A. Teukolsky, W. T. Vetterling, and B. P. Flannery, *Numerical recipes in C* (Cambridge University Press, Cambridge, 1992).
125. R. Graaff, J. G. Aarnoudse, J. R. Zijp, P. M. A. Sloot, F. F. M. de Mul, J. Greve, and M. H. Koelink, "Reduced light-scattering properties for mixtures of spherical particles: a simple approximation derived from Mie calculations," *Appl. Opt.* **31**, 1370-1376 (1992).
126. E. Evans and Y.-C. Fung, "Improved measurements of the erythrocyte geometry," *Microvasc. Res.* **4**, 335-347 (1972).
127. E. J. Hudson, M. R. Stringer, F. Cairnduff, D. V. Ash, and M. A. Smith, "The optical properties of skin tumours measured during superficial photodynamic therapy," *Lasers Med. Sci.* (1994).
128. S. T. Flock, B. C. Wilson, and M. S. Patterson, "Total attenuation coefficients and scattering phase functions of tissues and phantom materials at 633 nm," *Med. Phys.* **14**, 835-841 (1987).
129. R. Marchesini, A. Bertoni, S. Andreola, E. Melloni, and A. E. Sichirollo, "Extinction and absorption coefficients and scattering phase functions of human tissues *in vitro*," *Appl. Opt.* **28**, 2318-2324 (1989).
130. N. B. Nelson and B. B. Prézelin, "Calibration of an integrating sphere for determining the absorption coefficient of scattering suspensions," *Appl. Opt.* **32**, 6710-6717 (1993).
131. S.-P. Lin, L. Wang, S. L. Jacques, and F. K. Tittel, "Measurements of tissue optical properties by the use of oblique-incidence optical fiber reflectometry," *Appl. Opt.* **36**, 136-143 (1997).
132. R. A. J. Groenhuis, J. J. ten Bosch, and H. A. Ferwerda, "Scattering and absorption of turbid materials determined from reflection measurements. 2: Measuring method and calibration," *Appl. Opt.* **22**, 2463-2467 (1983).
133. A. Kienle, L. Lilge, M. S. Patterson, R. Hibst, R. Steiner, and B. C. Wilson, "Spatially resolved absolute diffuse reflectance measurements for noninvasive determination of the optical scattering and absorption coefficients of biological tissue," *Appl. Opt.* **35**, 2304-2314 (1996).
134. T. J. Farrell, B. C. Wilson, and M. S. Patterson, "The use of a neural network to determine tissue optical properties from spatially resolved diffuse reflectance measurements," *Phys. Med. Biol.* **37**, 2281 (1992).
135. K. M. Yoo and R. R. Alfano, "Determination of the scattering and absorption lengths from the temporal profile of a backscattered pulse," *Opt. Lett.* **15**, 276-278 (1990).
136. M. S. Patterson, J. D. Moulton, B. C. Wilson, K. W. Berndt, and J. R. Lakowicz, "Frequency-domain reflectance for the determination of the scattering and absorption properties of tissue," *Appl. Opt.* **30**, 4474-4476 (1991).
137. S. L. Jacques, "Principles of phase-resolved optical instruments," in *Future Trends in Biomedical Applications of Lasers*, L. O. Svaasand, ed., *SPIE* **1525**, 143-153 (SPIE, Berlin, Germany, 1991).
138. B. J. Tromberg, L. O. Svaasand, T.-T. Tsay, and R. C. Haskell, "Properties of photon density waves in multiple-scattering media," *Appl. Opt.* **32**, 607-616 (1993).
139. L. O. Svaasand, B. J. Tromberg, R. C. Haskell, T.-T. Tsay, and M. W. Berns, "Tissue characterization and imaging using photon density waves," *Opt. Eng.* **32**, 258-266 (1993).

140. S. J. Madsen, P. Wyss, L. O. Svaasand, R. C. Haskell, Y. Tadir, and B. J. Tromberg, "Determination of the optical properties of the human uterus using frequency-domain photon migration and steady-state techniques," *Phys. Med. Biol.* **39**, 1191-1202 (1994).
141. C. Lindquist, A. Pifferi, R. Berg, S. Andersson-Engels, and S. Svanberg, "Reconstruction of diffuse photon-density wave interference in turbid media from time-resolved transmittance measurements," *Appl. Phys. Lett.* **69**, 1674-1676 (1996).
142. S. A. Prahl, I. A. Vitkin, U. Bruggemann, B. C. Wilson, and R. R. Anderson, "Determination of optical properties of turbid media using pulsed photothermal radiometry," *Phys. Med. Biol.* **37**, 1203-1217 (1992).
143. G. Yoon, D. N. G. Roy, and R. C. Straight, "Coherent backscattering in biological media: measurement and estimation of optical properties," *Appl. Opt.* **32**, 580-585 (1993).
144. M. H. Eddowes, T. N. Mills, and D. T. Delpy, "Monte Carlo simulations of coherent backscatter for identification of the optical coefficients of biological tissues in vivo," *Appl. Opt.* **34**, 2261-2267 (1995).
145. J. M. Schmitt, A. Knüttel, and R. F. Bonner, "Measurement of optical properties of biological tissues by low-coherence reflectometry," *Appl. Opt.* **32**, 6032-6042 (1993).
146. J. A. Jacquez and H. F. Kuppenheim, "Theory of the integrating sphere," *J. Opt. Soc. Am.* **45**, 460-470 (1955).
147. D. G. Goebel, "Generalized integrating-sphere theory," *Appl. Opt.* **6**, 125-128 (1967).
148. M. Firbank, M. Hiraoka, M. Essenpreis, and D. T. Delpy, "Measurement of the optical properties of the skull in the wavelength range 650-950 nm," *Phys. Med. Biol.* **38**, 503-510 (1993).
149. J. W. Pickering, C. J. M. Moes, H. J. C. M. Sterenborg, S. A. Prahl, and M. J. C. van Gemert, "Two integrating sphere with an intervening scattering sample," *J. Opt. Soc. Am.* **9**, 621-631 (1992).
150. J. W. Pickering, S. A. Prahl, N. van Wieringen, J. F. Beek, H. J. C. M. Sterenborg, and M. J. C. van Gemert, "Double-integrating-sphere system for measuring the optical properties of tissue," *Appl. Opt.* **32**, 399-410 (1993).
151. K. Grandin and A. Roos, "Evaluation of correction factors for transmittance measurements in single-beam integrating sphere," *Appl. Opt.* **33**, 6098-6104 (1994).
152. J. H. Torres, A. J. Welch, I. Cilesiz, and M. Motamedi, "Tissue optical property measurements: Overestimation of absorption coefficient with spectrophotometric techniques," *Lasers Surg. Med.* **14**, 249-257 (1994).
153. D. J. Maitland, J. T. Walsh, Jr., and J. B. Prytowsky, "Optical properties of human gallbladder tissue and bile," *Appl. Opt.* **32**, 586-591 (1993).
154. V. G. Peters, D. R. Wyman, M. S. Patterson, and G. L. Frank, "Optical properties of normal and diseased human breast tissues in the visible and near infrared," *Phys. Med. Biol.* **35**, 1317-1334 (1990).
155. L. Wang and S. L. Jacques, "Error estimation of measuring total interaction coefficients of turbid media using collimated light transmission," *Phys. Med. Biol.* **39**, 2349-2354 (1994).
156. J. W. Pickering, P. Posthumus, and M. J. C. van Gemert, "Continuous measurement of the heat-induced changes in the optical properties (at 1,064 nm) of rat liver," *Lasers Surg. Med.* **15**, 200-205 (1994).
157. L. C. Junqueira, J. Carneiro, and J. A. Long, *Basic histology* (LANGE Medical Publications, Los Altos, California, 1986).
158. W. Verkruijsse, Personal communication (1995).
159. S. Wray, M. Cope, D. T. Delpy, J. S. Wyatt, and E. O. R. Reynolds, "Characterization of the near infrared absorption spectra of cytochrome *aa₃* and haemoglobin for the non-invasive monitoring of cerebral oxygenation," *Biochim. Biophys. Acta* **933**, 184-192 (1988).
160. J. A. Curcio and C. C. Petty, "The near infrared absorption spectrum of liquid water," *J. Opt. Soc. Am.* **41**, 302-304 (1951).
161. Y. Liu, R.-K. Cho, K. Sakurai, T. Miura, and Y. Ozaki, "Studies on spectra/structure correlations in near-infrared spectra of proteins and polypeptides. Part I: A marker band for hydrogen bonds," *Appl. Spectr.* **48**, 1249-1254 (1994).
162. J. W. Hall and A. Pollard, "Near-infrared spectroscopic determination of serum total proteins, albumin, globulins, and urea," *Clin. Biochem.* **26**, 483-490 (1993).
163. H. H. Mantsch and M. Jackson, "Molecular spectroscopy in biodiagnostics (from Hippocrates to Herschel and beyond)," *Journal of Molecular Structure* **347**, 187-206 (1995).
164. Y. Mendelson, A. C. Clermont, R. A. Peura, and B.-C. Lin, "Blood glucose measurement by multiple attenuated total reflection and infrared absorption spectroscopy," *IEEE Trans. Biomed. Eng.* **37**, 458-465 (1990).
165. G. M. Hale and M. R. Querry, "Optical constants of water in the 200-nm to 200-mm wavelength region," *Appl. Opt.* **12**, 555-563 (1973).
166. A. C. Guyton, *Textbook of medical physiology* (W.B. Saunders, Philadelphia, P.A. 1986).
167. F. P. Bolin, L. E. Preuss, R. C. Taylor, and R. J. Ference, "Refractive index of some mammalian tissue using a fiber optic cladding method," *Appl. Opt.* **28**, 2297-2303 (1989).

168. J. Qu and B. C. Wilson, "Monte Carlo modeling studies of the effect of physiological factors and other analytes on the determination of glucose concentration *in vivo* by near infrared optical absorption and scattering measurements," *J. Biomedical Optics* **2**, 319-325 (1997).
169. B. Chance, H. Liu, T. Kitai, and Y. Zhang, "Effects of solutes on optical properties of biological materials: models, cells, and tissues," *Anal. Biochem.* **227**, 351-362 (1995).
170. A. Dunn, C. Smithpeter, A. J. Welch, and R. Richards-Kortum, "Finite-difference time-domain simulation of light scattering from single cells," *J. Biomedical Optics* **2**, 262-266 (1997).
171. M. Tomita, M. Gotoh, M. Yamamoto, N. Tanahashi, and M. Kobari, "Effects of hemolysis, hematocrit, RBC swelling, and flow rate on light scattering by blood in a 0.26 cm ID transparent tube," *Biorheology* **20**, 485-494 (1984).
172. P. M. A. Sloot, A. G. Hoekstra, and C. G. Figdor, "Osmotic response of lymphocytes measured by means of forward light scattering: theoretical considerations," *Cytometry* **9**, 636-641 (1988).
173. D. E. Burger, J. H. Jett, and P. F. Mullaney, "Extraction of morphological features from biological models and cells by Fourier analysis of static light scatter measurements," *Cytometry* **2**, 327-336 (1982).
174. R. Graaff, J. G. Aarnoudse, F. F. M. de Mul, and H. W. Jentink, "Similarity relations for anisotropic scattering in absorbing media," *Opt. Eng.* **32**, 244-252 (1993).
175. A. H. Gandjbakhche, P. Mills, and P. Snabre, "Light-scattering technique for the study of orientation and deformation of red blood cells in a concentrated suspension," *Appl. Opt.* **33**, 1070-1078 (1994).
176. J. C. Kennedy, R. H. Pottier, and D. C. Pross, "Photodynamic therapy with endogenous protoporphyrin IX: Basic principles and present clinical experience," *J. Photochem. Photobiol. B: Biol.* **6**, 143-148 (1990).
177. T.M.A.R. Dubbelman, C. Prinsze, L.C. Penning, and J. van Steveninck, "Photodynamic therapy: membrane and enzyme photobiology," in *Photodynamic Therapy: Basic Principles and Clinical Applications*, B.W. Henderson and T.J. Dougherty, eds. (Marcel Dekker, Inc. New York, USA, 1992) pp. 37-47.
178. R. Hilf, "Cellular targets of photodynamic therapy as a guide to mechanisms," in *Photodynamic Therapy: Basic Principles and Clinical Applications*, B.W. Henderson and T.J. Dougherty, eds. (Marcel Dekker, New York, USA, 1992) pp. 47-54.
179. D.A. Bellnier and B.W. Henderson, "Determinants for photodynamic tissue destruction," in *Photodynamic Therapy: Basic Principles and Clinical Applications*, B.W. Henderson and T.J. Dougherty, eds. (Marcel Dekker, Inc. New York, USA, 1992) pp. 117-127.
180. H. I. Peterson, "Modification of tumour blood flow - a review," *Int. J. Radiat. Biol.* **60**, 201-210 (1991).
181. Q. Peng, T. Warloe, J. Moan, H. Heyerdahl, H. B. Steen, J. M. Nesland, and K.-E. Giercksky, "Distribution of 5-aminolevulinic acid-induced porphyrins in noduloulcerative basal cell carcinoma," *Photochem. Photobiol.* **62**, 906-913 (1995).
182. Q. Peng, T. Warloe, K. Berg, J. Moan, M. Kongshaug, K.-E. Giercksky, and J. M. Nesland, "5-aminolevulinic acid-based photodynamic therapy: clinical research and future challenges," *Cancer* **79**, 2282-2308 (1997).
183. J. Moan, K. Berg, H.B. Steen, T. Warloe, and K. Madslie, "Fluorescence and photodynamic effects of phthalocyanines and porphyrins in cells," in *Photodynamic Therapy: Basic Principles and Clinical Applications*, T.J. Dougherty and B.W. Henderson, eds. (Marcel Dekker, Inc. New York, USA, 1992) pp. 19-35.
184. S. Andersson-Engels, "Laser-induced fluorescence for medical diagnostics," Ph.D. thesis **LRAP-108** (Lund Institute of Technology, Lund, 1989).
185. C. Zhou, B. Xu, J. Xie, Y. Yang, Z. Ding, W. Yang, H. Shen, Y. Chen, and X. Ha, "An ultrastructural study of human bladder cancer treated by photodynamic therapy," *Lasers Med. Sci.* **3**, 87-92 (1988).
186. W. M. Star, H. P. A. Marijnissen, A. E. van den Berg-Blok, J. A. C. Versteeg, K. A. P. Franken, and H. S. Reinhold, "Destruction of rat mammary tumor and normal tissue microcirculation by hematoporphyrin derivative photoradiation observed *in vivo* in sandwich observation chambers," *Cancer Res.* **46**, 2532-2540 (1986).
187. M. W. R. Reed, F. N. Miller, T. J. Wieman, M. T. Tseng, and C. G. Pietsch, "The effect of photodynamic therapy on the microcirculation," *J. Surg. Res.* **45**, 452-459 (1988).
188. D. L. Liu, I. Wang, S. Andersson-Engels, C. H. Håkansson, U. Stenram, and K. Svanberg, "Intra-operative laser-induced photodynamic therapy in the treatment of experimental hepatic tumours," *Eur. J. Gastroenterol. Hepatol.* **7**, 1073-1080 (1995).
189. K. Svanberg, D. L. Liu, I. Wang, S. Andersson-Engels, U. Stenram, and S. Svanberg, "Photodynamic therapy using intravenous d-aminolaevulinic acid-induced protoporphyrin IX sensitisation in experimental hepatic tumours in rats," *Br. J. Cancer* **74**, 1526-1533 (1996).
190. D. L. Liu, K. Svanberg, I. Wang, S. Andersson-Engels, and S. Svanberg, "Laser Doppler perfusion imaging: New technique for determination of perfusion and reperfusion of splanchnic organs and tumor tissue," *Lasers Surg. Med.* **20**, 473-479 (1997).
191. J. P. A. Marijnissen and W. M. Star, "Quantitative light dosimetry *in vitro* and *in vivo*," *Lasers Med. Sci.* **2**, 235-242 (1987).

192. I. Wang, S. Andersson-Engels, G. E. Nilsson, K. Wårdell, and K. Svanberg, "Superficial bloodflow following photodynamic therapy of malignant skin tumours measured by laser Doppler imaging," *Br. J. Dermatol.* **136**, 184-189 (1997).
193. L. O. Svaasand, B. J. Tromberg, P. Wyss, M.-T. Wyss-Desserich, Y. Tadir, and M. W. Berns, "Light and drug distribution with topically administered photosensitizers," *Lasers Med. Sci.* **11**, 261-265 (1996).
194. L. O. Svaasand, P. Wyss, M. T. Wyss, Y. Tadir, B. J. Tromberg, and M. W. Berns, "Dosimetry model for photodynamic therapy with topically administered photosensitizers," *Lasers Surg. Med.* **18**, 139-149 (1996).
195. L. O. Svaasand, T. Boerslid, and M. Oeveraasen, "Thermal and optical properties of living tissue: application to laser-induced hyperthermia," *Lasers Surg. Med.* **5**, 589-602 (1985).
196. R. R. Anderson and J. A. Parrish, "Selective photothermolysis: precise microsurgery by selective absorption of pulsed radiation," *Science* **220**, 524-527 (1983).
197. O. T. Tan, P. Morrison, and A. K. Kurban, "585 nm for the treatment of port-wine stains," *Plast. Reconstr. Surg.* **86**, 1112-1117 (1990).
198. W. Verkruysse, J. W. Pickering, J. F. Beek, M. Keijzer, and M. J. C. van Gemert, "Modelling the effect of wavelength on the pulsed dye laser treatment of port wine stains," *Appl. Opt.* **32**, 393-398 (1993).
199. J. F. de Boer, G. W. Lucassen, W. Verkruysse, and M. J. C. van Gemert, "Thermolysis of port-wine-stain blood vessels: diameter of damaged blood vessel depends on the laser pulse length," *Lasers Med. Sci.* **11**, 177-180 (1996).
200. S. Thomsen, "Pathologic analysis of photothermal and photomechanical effects of laser-tissue interactions," *Photochem. Photobiol.* **53**, 825-835 (1991).
201. S. Hotta, H. Kashimura, S. Hirai, A. Nakahara, H. Fukutomi, T. Osuga, and U. Uchiyama, "Immediate changes in subcellular structures of transplanted tumors following photodynamic and laser hyperthermic therapy," *Lasers Surg. Med.* **16**, 262-271 (1995).
202. L. Liu, S. Andersson-Engels, C. Stureson, K. Svanberg, C. H. Håkansson, and S. Svanberg, "Tumour vessel damage resulting from laser-induced hyperthermia alone and in combination with photodynamic therapy," *Cancer Lett.* **111**, 1-9 (1996).
203. G. J. Derbyshire, D. K. Bogen, and M. Unger, "Thermally induced optical property changes in myocardium at 1.06 mm," *Lasers Surg. Med.* **10**, 28-34 (1990).
204. R. Agah, A. H. Gandjbakhche, M. Motamedi, R. Nossal, and R. F. Bonner, "Dynamics of temperature dependent optical properties of tissue: dependence on thermally induced alteration," *IEEE Trans. Biomed. Eng.* **43**, 839-846 (1996).
205. O. T. Tan, P. Morrison, S. Murray, and E. F. MacNichol, "Red blood cell responses to pulsed laser irradiation," in *Laser surgery: advanced characterisation, therapeutics and systems*, K. Atsumi, N. R. Goldblatt, and S. N. Joffe, eds., Proc. Soc. Photo-Opt. Instrum. Eng. **1066**, 154-164 (SPIE, Bellingham, 1989).
206. W.-C. Lin, M. Motamedi, and A. J. Welch, "Dynamics of tissue optics during laser heating of turbid media," *Appl. Opt.* **35**, 3413-3420 (1996).
207. S. Rastegar and M. Motamedi, "A theoretical analysis of dynamic variation of temperature dependent optical properties in the response of laser irradiated tissue," in *Laser-tissue interaction*, S. L. Jacques, ed., Proc. Soc. Photo-Opt. Instrum. Eng. **1202**, 253-259 (SPIE, Bellingham, 1990).
208. R. Splinter, S. Y. Semenov, G. A. Nanney, L. Littman, J. R. Tuntelder, R. H. Svenson, C. H. Chuang, and G. P. Tatis, "Myocardial temperature distribution under cw Nd:YAG laser irradiation *in vitro* and *in vivo* situations: theory and experiment," *Appl. Opt.* **34**, 391-399 (1995).
209. A. Mahadevan-Jensen and R. Richards-Kortum, "Raman spectroscopy for the detection of cancers and precancers," *J. Biomedical Optics* **1**, 31-70 (1996).
210. J. R. Mourant, I. J. Bigio, D. A. Jack, T. M. Johnson, and H. D. Miller, "Measuring absorption coefficients in small volumes of highly scattering media: source-detector separations for which path lengths do not depend on scattering properties," *Appl. Opt.* **36**, 5655-5661 (1997).
211. L. T. Norvang, E. J. Fiskerstrand, K. König, B. Bakken, Ö. Standahl, T. E. Milner, M. W. Berns, J. S. Nelson, and L. O. Svaasand, "Comparison between reflectance spectra obtained with an integrating sphere and a fiber-optic collection system," in *Laser-tissue interaction and tissue optics*, G. P. Delacretaz, R. W. Steiner, L. O. Svaasand, H. J. Albrecht, and T. H. Meier, eds., Proc. Soc. Photo-Opt. Instrum. Eng. **2624**, 155-2624 (SPIE, Bellingham, 1996).
212. S.L. Jacques, "Reflectance spectroscopy with optical fiber devices, and transcutaneous bilirubinometers," in *Biomedical optical instrumentation and laser-assisted biotechnology*, A.M. Verga Scheggi, S. Martellucci, A.N. Chester, and R. Pratesi, eds., NATO **325** (Kluwer Academic Publishers, Dordrecht, 1996) pp. 83-94.
213. A. F. Gmitro, F. W. Cutruzzola, M. L. Stetz, and L. Deckelbaum, "Measurement depth of laser-induced tissue fluorescence with application to laser angioplasty," *Appl. Opt.* **27**, 1844-1849 (1988).
214. V. R. Kolli, A. R. Shaha, H. E. Savage, P. G. Sacks, M. A. Casale, and S. P. Schantz, "Native cellular fluorescence can identify changes in epithelial thickness *in vivo* in the upper aerodigestive tract," *American Journal of Surgery* **170**, 495-498 (1995).

215. H. Zeng, C. MacAuley, D. I. McLean, and B. Palcic, "Spectroscopic and microscopic characteristics of human skin autofluorescence emission," *Photochem. Photobiol.* **61**, 639-645 (1995).
216. A. A. Oraevsky, S. L. Jacques, G. H. Pettit, R. A. Sauerbrey, F. K. Tittel, J. H. Nguy, and P. D. Henry, "XeCl laser-induced fluorescence of atherosclerotic arteries. Spectral similarities between lipid-rich lesions and peroxidized lipoproteins," *Circulation Research* **72**, 84-90 (1993).
217. M. Perk, G. J. Flynn, C. Smith, B. Bathgate, J. Tulip, W. Yue, and A. Lucas, "Laser-induced fluorescence emission: I. The spectroscopic identification of fibrotic endocardium and myocardium," *Lasers Surg. Med.* **11**, 523-534 (1991).
218. W. Lohmann and F. Hugo, "The effect of NADH on different human and mouse cell lines," *Naturwissenschaften* **76**, 72-74 (1989).
219. L. Baert, R. Berg, B. van Damme, M. A. D'Hallewin, J. Johansson, K. Svanberg, and S. Svanberg, "Clinical fluorescence diagnosis of human bladder carcinoma following low-dose Photofrin injection," *Urol.* **41**, 322-330 (1993).
220. K. Svanberg, T. Andersson, D. Killander, I. Wang, U. Stenram, S. Andersson-Engels, R. Berg, J. Johansson, and S. Svanberg, "Photodynamic therapy of non-melanoma malignant tumours of the skin using topical d-amino levulinic acid sensitization and laser irradiation," *Br. J. Dermatol.* **130**, 743-751 (1994).
221. D. F. Morrison, *Multivariate statistical methods* (McGraw-Hill Book Company, New York, 1976).
222. S. A. Ahmed, Z. Zang, K. M. Yoo, M. A. Ali, and R. R. Alfano, "Effect of multiple light scattering and self-absorption on the fluorescence and excitation spectra of dyes in random media," *Appl. Opt.* **33**, 2746-2750 (1994).
223. J. Wu, M. S. Feld, and R. P. Rava, "Analytical model for extracting intrinsic fluorescence in turbid media," *Appl. Opt.* **32**, 3585-3595 (1993).
224. C. M. Gardner, S. L. Jacques, and A. J. Welch, "Fluorescence spectroscopy of tissue: recovery of intrinsic fluorescence from measured fluorescence," *Appl. Opt.* **35**, 1780-1792 (1996).
225. M. Sinaasappel and H. J. C. M. Sterenborg, "Quantification of the hematoporphyrin derivative by fluorescence measurement using dual-wavelength excitation and dual-wavelength detection," *Appl. Opt.* **32**, 541-548 (1993).
226. H. J. C. M. Sterenborg, A. E. Saarnak, R. Frank, and M. Motamedi, "Evaluation of spectral correction techniques for fluorescence measurements on pigmented lesions in vivo," *J. Photochem. Photobiol. B: Biol.* **35**, 159-165 (1996).
227. N. Mohandas, Y. R. Kim, D. H. Tycko, J. Orlik, J. Wyatt, and W. Groner, "Accurate and independent measurement of volume and hemoglobin concentration of individual red cells by laser light scattering," *Blood* **68**, 506-513 (1986).
228. J. R. Mourant, I. J. Bigio, J. Boyer, R. L. Conn, T. Johnson, and T. Shimada, "Spectroscopic diagnosis of bladder cancer with elastic light scattering," *Lasers Surg. Med.* **17**, 350-357 (1995).
229. L. O. Svaasand, L. T. Norvang, E. J. Fiskerstrand, E. K. S. Stopps, M. W. Berns, and J. S. Nelson, "Tissue parameters determining the visual appearance of normal skin and port-wine stains," *Lasers Med. Sci.* **10**, 55-65 (1995).
230. E. J. Fiskerstrand, L. O. Svaasand, G. Kopstad, M. Dalaker, L. T. Norvang, and G. Volden, "Laser treatment of port wine stains: therapeutic outcome in relation to morphological parameters," *Br. J. Dermatol.* **134**, 1039-1043 (1996).
231. L. O. Svaasand, E. J. Fiskerstrand, G. Kopstad, L. T. Norvang, E. K. Svaasand, J. S. Nelson, and M. W. Berns, "Therapeutic response during pulsed laser treatment of port-wine stains: dependence on vessel diameter and depth in dermis," *Lasers Med. Sci.* **10**, 235-243 (1995).
232. J. M. Steinke and A. P. Shepherd, "Reflectance measurements of hematocrit and oxyhemoglobin saturation," *Am. J. Physiol.* **253**, H147-H153 (1987).
233. F. F. Jöbsis, "Noninvasive, infrared monitoring of cerebral and myocardial oxygen sufficiency and circulatory parameters," *Science* **198**, 1264-1267 (1977).
234. M. Cope and D. T. Delpy, "System for long-term measurement of cerebral blood and tissue oxygenation on newborn infants by near infra-red transillumination," *Med. Biol. Eng. Comput.* **26**, 289-294 (1988).
235. S. J. Matcher and C. E. Cooper, "Absolute quantification of deoxyhaemoglobin concentration in tissue near infrared spectroscopy," *Phys. Med. Biol.* **39**, 1295-1312 (1994).
236. R. Berg, O. Jarlman, and S. Svanberg, "Medical transillumination imaging using short-pulse diode lasers," *Appl. Opt.* **32**, 574-579 (1993).
237. H. Heusmann, J. Kölzer, J. Otto, R. Puls, T. Friedrich, S. Heywang-Köbrunner, and W. Zinth, "Spectral transillumination of female breasts and breast tissue-like material," in *Photon Transport in Highly Scattering Tissue*, S. Avrillier, B. Chance, G. J. Müller, A. V. Priezzhev, and V. V. Tuchin, eds., Proc. Soc. Photo-Opt. Instrum. Eng. **2326**, 370-382 (SPIE, Bellingham, 1995).
238. J. A. Jacquez, J. Huss, W. McKeenhan, J. M. Dimitroff, and H. F. Kuppenheim, "Spectral reflectance of human skin in the region 0.7-2.6 m," *J. Appl. Physiol.* **8**, 297-299 (1955).

-
239. L. A. Cassis and R. A. Lodder, "Near-IR imaging of atheromas in living arterial tissue," *Anal. Chem.* **65**, 1247-1256 (1993).
240. J. M. Carney, W. Landrum, L. Mayes, Y. Zou, and R. A. Lodder, "Near-infrared spectrophotometric monitoring of stroke-related changes in the protein and lipid composition of whole gerbil," *Anal. Chem.* **65**, 1305-1313 (1993).
241. B. Rigas, S. Morgello, I. S. Goldman, and P. T. T. Wong, "Human colorectal cancers display abnormal Fourier-transform infrared spectra," *Proc. Natl. Acad. Sci. USA* **87**, 8140-8144 (1990).
242. R. Manoharan, J. J. Baraga, R. P. Rava, R. R. Dasari, M. Fitzmaurice, and M. S. Feld, "Biochemical analysis and mapping of atherosclerotic human artery using FT-IR microspectroscopy," *Atherosclerosis* **103**, 181-193 (1993).
243. K.-Z. Liu, M. Jackson, M. G. Sowa, H. Ju, I. M. C. Dixon, and H. H. Mantsch, "Modification of the extracellular matrix following myocardial infarction monitored by FTIR spectroscopy," *Biochim. Biophys. Acta* **1315**, 73-77 (1996).
244. A. Troilius, B. Ljunggren, S. Bornemyr, B. Nilsson, and K. Wårdell, "Evaluation of port wine stain perfusion by laser Doppler imaging and thermography before and after argon laser treatment," *Acta Derm. Venereol.* **72**, 6-10 (1992).
245. K. Wårdell, H. K. Naver, G. E. Nilsson, and B. G. Wallin, "The cutaneous vascular axon reflex in humans characterized by laser Doppler perfusion imaging," *J. Physiol.* **460**, 185-199 (1993).
246. K. Wårdell, A. Jakobsson, and G. E. Nilsson, "Laser Doppler perfusion imaging by dynamic light scattering," *IEEE Trans. Biomed. Eng.* **40**, 309-316 (1993).
247. A. Jakobsson and G. E. Nilsson, "Prediction of sampling depth and photon pathlength in laser Doppler flowmetry," *Med. Biol. Eng. Comput.* **31**, 301-307 (1993).
248. P. Å. Öberg, "Laser-Doppler flowmetry," *Crit. Rev. Biomed. Eng.* **18**, 125-163 (1990).
249. M. Linden, A. Sirsjo, L. Lindbom, G. Nilsson, and A. Gidlof, "Laser-Doppler perfusion imaging of microvascular blood flow in rabbit tenuissimus muscle," *Am. J. Physiol.* **269**, H1496-500 (1995).
250. Z. Chen, T. E. Milner, S. Srinivas, X. Wang, A. Malekafzali, M. J. C. van Gemert, and J. S. Nelson, "Noninvasive imaging of *in vivo* blood flow velocity using optical Doppler tomography," *Opt. Lett.* **22**, 1119-1121 (1997).

13. Papers
